

A Search for High-Energy Gamma-rays from
AGN ON+231 with the STACEE-32 Detector

Claude G. Théoret

Department of Physics, McGill University

Montreal, Quebec, Canada

August, 2001

A Thesis submitted to the
Faculty of Graduate Studies and Research
in partial fulfillment of the requirements for the degree
Doctor of Philosophy

©Claude G. Théoret, 2001



**National Library
of Canada**

**Acquisitions and
Bibliographic Services**

395 Wellington Street
Ottawa ON K1A 0N4
Canada

**Bibliothèque nationale
du Canada**

**Acquisitions et
services bibliographiques**

395, rue Wellington
Ottawa ON K1A 0N4
Canada

Your file Votre référence

Our file Notre référence

The author has granted a non-exclusive licence allowing the National Library of Canada to reproduce, loan, distribute or sell copies of this thesis in microform, paper or electronic formats.

The author retains ownership of the copyright in this thesis. Neither the thesis nor substantial extracts from it may be printed or otherwise reproduced without the author's permission.

L'auteur a accordé une licence non exclusive permettant à la Bibliothèque nationale du Canada de reproduire, prêter, distribuer ou vendre des copies de cette thèse sous la forme de microfiche/film, de reproduction sur papier ou sur format électronique.

L'auteur conserve la propriété du droit d'auteur qui protège cette thèse. Ni la thèse ni des extraits substantiels de celle-ci ne doivent être imprimés ou autrement reproduits sans son autorisation.

0-612-78786-9

Pour Lucien, Michelle et Lucien

Abstract

The Solar Tower Atmospheric Čerenkov Effect Experiment (STACEE) is a ground-based atmospheric Čerenkov telescope constructed to conduct γ -ray astronomy. The STACEE telescope employs the mirrors of the National Solar Thermal Test Facility (NSTTF) to observe γ -rays at a lower energy threshold than the current generation of imaging atmospheric Čerenkov telescopes. A prototype of the telescope was constructed in 1998 which used 32 heliostat mirrors of the NSTTF with a total collection area of $\sim 1200 m^2$. This prototype called STACEE-32, was used to search for high energy γ -ray emissions from the active galactic nucleus (AGN) ON+231 (also known as W Coma and 1219+285). The STACEE-32 response as a function of energy was calculated for this source and we report a spectral energy threshold of $E_{th} = 130 \pm 50 GeV$. The analysis of data collected in the spring of 1999 resulted in a non-detection of the AGN at this energy. We derived a 95% confidence level upper limit on the integrated γ -ray flux for this source of $\Phi_{int}(E > 130 \pm 50 GeV) \leq 2.4 \times 10^{-10} cm^{-2} sec^{-1}$. This upper limit further constrains the high energy flux extrapolations of this AGN.

Résumé

Le détecteur STACEE (Solar Tower Atmospheric Čerenkov Effect Experiment) est un télescope à effet Čerenkov terrestre construit dans le but d'effectuer des études en astrophysique des rayons- γ . Le télescope STACEE utilise les miroirs du NSTTF (National Solar Thermal Test Facility) pour observer des rayons- γ à un seuil d'énergie inférieur aux seuils de la présente génération de télescope Čerenkov imageurs. Un prototype du télescope utilisant 32 miroirs solaires du NSTTF fut construit en 1998. Ce prototype, qui a porté le nom de STACEE-32, a été utilisé au printemps 1999 pour effectuer une recherche des émissions de rayons- γ provenant du noyau actif galactique ON+231 (aussi surnommé W Coma ou 1219+285). L'acceptance de STACEE-32 en fonction de l'énergie a été calculée et le seuil d'énergie pour cette source est de $E_{th} = 130 \pm 50 GeV$. L'analyse des données indique aucun signal de rayons- γ provenant de ON+231. Nous avons calculé une limite supérieure (à un niveau de confiance de 95%) du flux intégré de rayons- γ provenant de ON+231 de $\Phi_{int}(E > 130 \pm 50 GeV) \leq 2.4 \times 10^{-10} cm^{-2} sec^{-1}$. Cette limite supérieure limite l'extrapolation aux hautes énergies du flux de rayons- γ de ON+231.

Acknowledgements

The construction of a new instrument of the scale of STACEE, can only be the result of the cooperation of a large group of people. The list of people for whom I owe gratitude is long and I apologise to anyone I have forgotten.

I would like to thank Ken Ragan, my official supervisor, for his guidance and patience; but mostly for teaching me to think like a scientist. Ken's dedication to teaching made him a very available supervisor, and in the almost weekly meetings we had over the years, I learned how to work more effectively, focus my efforts and turn hunches into facts.

I would like to thank David Hanna, my unofficial supervisor, for all of his technical advice and for convincing me to join the STACEE group in 1997. Leaving something as established as CDF for a new experiment using an unproven concept was a risky and more difficult path for a Ph.D.; but, one that I don't regret, since the satisfaction derived from this pioneering work and the doors that were open to me as a consequence, were well worth it. Thanks Dave.

The McGill shop played a large and key role in the construction of STACEE-32. Eddie Del Campo, Michel Houde, Cathy Farrow and Steve Kecani, all involved with the design and manufacture of the STACEE-32 prototype, all worked extra hours so that we could construct the experiment on time. During that time I worked in close collaboration with Steve Kecani and saw first hand how his ingenuity and skill shaped design into reality.

The data analysis and simulation involved with STACEE-32 was as large an undertaking, in man hours, as the actual construction of the telescope. I would like to thank our computer system administrators Paul Mercure and Juan Gallego for the invisible and often thankless tasks of keeping our computers running, our software up to date and answering hundreds of my questions.

I would like to thank the rest of my STACEE collaborators who helped build and operate STACEE-32: Rene Ong, Corbin Covault, Mark Chantell, Zoa Conner, Dave Williams, Lowell Boone, Reshmi Mukherjee, Dippen Bhattacharya, Mark Dragovan, Richard Scalzo, Tumay Tumer, Pascal Fortin and, in particular, Scott Oser. Scott Oser was the first graduate student in the STACEE collaboration and answered many of my queries as I was writing this thesis.

The STACEE telescope benefited massively from the existing infrastructure of the NSTTF. The staff at the NSTTF were instrumental in helping us adapt an industrial scale solar power research facility, into an instrument capable of fine tuned astronomical measurements. I would like to thank J.J. Kelton, Darell Johnson, Kye Chisman, Roy Tucker, Mike Usher, Mike Edgar, Cheryl Ghanbari, Bill Kolb and Loula Killian not only for their technical prowess (and occasionally borrowed tools), their prompt repair of heliostats, their handling of the administration (specifically in obtaining our security passes);but, also for making me feel so welcomed and at home in New Mexico.

In the summer of 1998 I fell very ill and suffered from liver problems that still affect me to this day. In my early visits to the McGill Health Centre that summer I had the good fortune to have an appointment with Dr. Barbara Black. Thanks to her kindness, expertise and careful monitoring I was able to minimise the time lost to the disease and make a long but steady recovery.

During my PhD I received the financial support of the McGill Major Chalk-Rowles fellowship and our group received funding from NSERC and FCAR. I would like to thank the trustees of the Chalk-Rowles fund Mr. Norman Hewton and Mrs. Carol Tanner.

Over the course of my PhD I developed a love for Montréal, that is no doubt due to the friends I have made here. I would like to thank Lisa God-

win, Kurt Chaboyer, Marie Thone, Sophie Morissette, Diane Leyland, Chantal Robichaud, Tiago DeJesus, Andrea Holtslander, Marko Milek, Lin Wai Hung, Jocelyn Bourdages, Sébastien Blais-Ouillette, Tracy Smee, Todd Van Dyke, Patrick McDonough and Rachel Spencer for their help, their support, their music, their advice and, especially Marie, for taking care of me when I was sick.

I thank my girlfriend, Tamsin Rothery, for putting up with me while I wrote this thesis.

Finally I would like to thank my parents for their support and love. I owe whatever success I have (or will have) as a physicist to my work ethic, taught to me by my father over many years on the farm and in the bush, and to my curiosity, fostered and encouraged by my mother for as long as I can remember.

Personal Contributions to STACEE-32

I first joined the STACEE Collaboration in September of 1997. My first task was the creation of the high voltage control system used in the STACEE cameras. This system was implemented in my first shift in January of 1998. Upon my return to McGill I installed the STOFF (STACEE Offline data unpacking software package) at McGill and wrote analysis software used to analyse the data from the SGI based DAQ used for the 16 channel prototype. Concurrently, I participated in the initial R&D and production of the light concentrators (DTIRCs).

I later participated in the assembly shift used to upgrade the experiment from 16 to 32 channels. Upon my return to McGill I then used the STOFF package to write my own version of the 32 channel analysis software. In the summer of 1998 I designed a graphical user interface for the HV control software. In the fall of 1998 I implemented a current monitoring and HV trip/alarm system into the general DAQ. In the winter of 1998/99 I took several data shifts at Sandia and I installed the MOCCA shower simulation software package at McGill and used it to start MC shower studies. In the spring of 1999 I performed the initial analysis of the ON+231 data set used in this thesis. I developed the L1 rate model in the summer 1999 and, in performing the initial work presented in chapter five, discovered a problem with the accepted effective area curve.

In the spring of 2000 I participated in the heliostat mirror re-alignment and in the expansion of the experiment to the 48 channel instrument. In the summer and fall of 2000 I participated in several calibration shifts for STACEE-48, performed MC studies and developed the trigger model used in this thesis. I started the actual thesis writing in January of 2001 and performed much of the final MC studies presented in this thesis in the spring of 2001.

Glossary and Definition of terms

The term γ -ray is used to denote photons with energies above several hundred thousand electron volts (eV). All photons of energy greater than X-rays are called γ -rays. Thus γ -rays occupy an extremely broad range of the electromagnetic spectrum. The unbounded nature of γ -ray energies leads to the creation of subdivisions in the field of γ -ray astronomy, with subdivisions dictated by the detection mechanisms used to study the specific energy range.

Energy Range	Nomenclature	Detection Technique
10-30 MeV	medium energy	satellite-based Compton telescope
30 MeV - 30 GeV	high energy (HE)	satellite-based tracking detector
30 GeV - 30 TeV	very high energy (VHE)	ground-based atmospheric Čerenkov telescope ground based air shower particle detector
30 TeV - 30 PeV	ultra high energy (UHE)	ground based air shower particle detector

Table 1: γ -ray astronomy nomenclature

parsec A parsec (pc) is a unit of distance derived from the parallax angle to a star (parsec is a short form of parallax-second). 1 parsec is the distance from which the radius of the Earth's orbit, 1 astronomical unit (AU), subtends an angle of 1". A parsec is equal to 3.2 light years.

magnitude scale The magnitude scale is a logarithmic brightness scale. Five magnitudes represent a factor of 100 in brightness. Thus, one magnitude

difference between two objects is equivalent to factor $100^{1/5} \approx 2.512$ in brightness. The brightness of an object is inversely related to the square of the distance to that source. Thus, the **absolute magnitude** is needed to define the light output of a star. The absolute magnitude of a star, M , is the apparent magnitude of the star if it was 10 pc away.

radiation length The radiation length is a unit of measure used extensively in high energy and nuclear physics. The radiation length is the distance over which an electron's energy is reduced by a factor of $1/e$ due to radiation loss only in a given material.

redshift For cosmological distances (such as extragalactic sources), one can use Hubble's Law and the redshift of the object to estimate the distance to the source. For redshifts $z \leq 2$ the distance d to a source for a redshift z is:

$$d \simeq \frac{c}{H_0} \frac{(z+1)^2 - 1}{(z+1)^2 + 1} \quad (1)$$

Schwarzschild radius The Schwarzschild radius is a parameter used in the descriptions of collapsed stars and black holes. It is defined as $R_s = 2GM/c^2$, where M is the mass of the collapsed star or black hole, and physically corresponds to the radius within which no information can be retrieved from an observer outside that radius.

Gamma Ray Bursts Gamma Ray Bursts (GRBs) are enigmatic flashes of γ -rays that occur about once a day. They have been observed from the optical energy range (eV) up to several GeV. The bursts last on the order of a few seconds and seem to be distributed evenly over the sky.

STACEE	Solar Tower Atmospheric Effect Experiment
NSTTF	National Solar Thermal Test Facility
CGRO	Compton Gamma Ray Observatory
EGRET	Energetic Gamma Ray Telescope
ACT	Atomspheric Čerenkov Telescope
IACT	Imaging Atomspheric Čerenkov Telescope
AGN	Active Galactic Nucleus
SNR	Super Nova Remnant
SSC	Synchrotron Self Compton
IC	Inverse Compton
IR	Infra-Red
SED	Spectral Energy Distribution
NSB	Night Sky Background
MCS	Master Control System
PMT	Photomultiplier Tube
DTIRC	Dielectric Total Internal Reflection Concentrators
TDC	Time to Digital Converter
ADC	Analogue to Digital Converter
TOF	Time of Flight
L1	Level 1 trigger
L2	Level 2 trigger
DAQ	Data Acquisition
HV	High Voltage
MC	Monte Carlo
QE	Quantum Efficiency
CL	Confidence Level

Table 2: Several of the acronyms in the thesis are explained.

Contents

Abstract	ii
Résumé	iii
Acknowledgements	iv
Personal Contributions	vii
Glossary and Definition of Terms	viii
1 Introduction	1
1.1 VHE γ -ray Astronomy: Review of a Young Field	1
1.1.1 Satellite-Based Experiments	2
1.2 Ground-based VHE γ -ray astronomy	6
1.2.1 Electromagnetic Showers	7
1.2.2 Atmospheric Showers	9
1.2.3 Čerenkov Light from EAS	11
1.2.4 Differentiating Between Proton- and γ -induced Showers . .	15

1.2.5	Imaging Atmospheric Čerenkov Telescopes	18
1.2.6	The Unobserved Gap and the Need for New Instruments	22
1.3	Astrophysics of the γ -ray sky	24
1.3.1	Physics Processes in γ -ray Astronomy	26
1.3.2	Active Galactic Nuclei	31
1.4	AGN ON+231	39
1.4.1	Optical Observations	40
1.4.2	Radio Observations	42
1.4.3	X-ray Observations	45
1.4.4	γ -ray Observations	47
2	The STACEE-32 Detector	50
2.1	ACT Energy Threshold	50
2.1.1	Reducing the Energy Threshold	52
2.2	STACEE Concept	53
2.2.1	NSTTF	54
2.2.2	Heliostats	57
2.2.3	The Secondary Optical System	60
2.2.4	The PMT Cameras	63
2.2.5	Electronics	71

<i>CONTENTS</i>	xiii
3 Simulations of STACEE-32	84
3.1 Atmospheric Shower Simulation	85
3.1.1 Monte Carlo Technique	85
3.1.2 Atmospheric Modelling	86
3.1.3 MOCCA Shower Simulation Package	89
3.2 Telescope Simulation	90
3.2.1 Heliostat Modelling	90
3.2.2 Secondary Mirror Modelling	94
3.2.3 DTIRC and Cookie Modelling	94
3.2.4 Modelling of the Photocathode	96
3.2.5 Trigger Model	97
3.3 Simulation Results	104
3.3.1 Cosmic Ray Rate	104
3.3.2 Effective Area Curve	106
3.3.3 Calculating the Energy Threshold	110
4 Data Analysis	113
4.1 Data Collection	113
4.1.1 A Typical Night at the STACEE Telescope	115
4.2 Analysis Technique	116

4.2.1	Run Cuts	118
4.2.2	L1 Rate Cuts	118
4.2.3	Cuts Due to Technical Problems	122
4.2.4	Event Cuts: Offline Reconstruction of Events	123
4.2.5	Deadtime	126
4.2.6	Timing Corrections and Heliostat Arrival Times	127
4.2.7	Wavefront Reconstruction	129
4.2.8	Fitting Showerfronts to a Sphere	133
4.2.9	χ^2_{sphere} Cut	136
5	Results and Conclusion	142
5.1	Results	142
5.1.1	Calculating an Upper Limit	144
5.1.2	Calculating the Integral Flux Limit	145
5.1.3	Systematic Uncertainty	148
5.2	Discussion and Conclusion	153
	Bibliography	159

List of Figures

1.1	CGRO diagram	3
1.2	Schematic of EGRET	5
1.3	3rd EGRET catalog	6
1.4	Electromagnetic Shower Model	8
1.5	Atmospheric γ -ray shower penetration.	10
1.6	Čerenkov Wavefronts.	12
1.7	Formation of Čerenkov rings and circles.	13
1.8	Radial Čerenkov density distribution.	14
1.9	Čerenkov Light Yield.	16
1.10	Čerenkov Photon Distribution on the Ground.	17
1.11	Shower Timing Profiles.	18
1.12	Schematic of the Whipple IACT	20
1.13	Schematic of the CAT camera	21
1.14	γ -ray vs. Hadronic Showers in IACT Camera	22

1.15	TeV γ -ray Source Catalog	23
1.16	Extrapolated EGRET spectra	24
1.17	Shock Front Acceleration Model	27
1.18	SSC Model and Data for the Crab	30
1.19	Intergalactic IR Field Opacity	32
1.20	Effect of pair creation on AGN spectra	33
1.21	Highly conceptualised AGN diagram	36
1.22	Viewing Angle Effects on AGN Emission	37
1.23	Hadronic and Leptonic Beam Models	38
1.24	ON+231 Historical Light Curve	40
1.25	ON+231 Outburst Light Curve	41
1.26	ON+231 3.8 Year Outburst Period	42
1.27	ON+231 Radio Light Curve	43
1.28	ON+231 Radio Image	45
1.29	ON+231 SED	46
1.30	ON+231 EGRET Spectrum	48
2.1	STACEE Concept	54
2.2	Aerial View of the NSTTF	55
2.3	Schematic of the Tower	56

2.4	Schematic of an NSTTF Heliostat	58
2.5	Digital Nature of Heliostat Control	59
2.6	STACEE Spider Schematic.	61
2.7	STACEE Secondary and Camera Schematic.	62
2.8	Off Axis Aberrations	63
2.9	Canister Cross Section	65
2.10	Actual DTIRC and Ray trace	66
2.11	Optical throughput of STACEE-32	68
2.12	Single Photoelectron Pulse Spectrum	70
2.13	STACEE Electronics Block Diagram	72
2.14	Dynamic Delay Example	73
2.15	Rate vs. Threshold Curve	75
2.16	STACEE-32 heliostat/cluster distribution	77
2.17	STACEE Trigger and Delay systems	78
2.18	STACEE ADC system	80
3.1	Mie Scattering of white light.	88
3.2	CCD Image of a sun calibration spot.	92
3.3	Sunspot Curves: Simulated and Measured.	93
3.4	Camera occultation	95

3.5	Simulated DTIRC Response Curve	96
3.6	Photocathode Efficiency at 400 nm	97
3.7	Light Ray Diagram of Photocathode	98
3.8	Lagging Photons in a Čerenkov Wavefront	101
3.9	Trigger Ratio variation with Tube Time	102
3.10	Azimuth and Elevation Angle Distribution of ON+231 Data Set .	107
3.11	Effective Area Curves	108
3.12	Crab Effective Area Curves	109
3.13	Average Effective Area Curve	110
3.14	ON+231-STACEE-32 Energy Threshold	112
4.1	A typical night with STACEE.	117
4.2	L1 Rate Model	121
4.3	L1 Rate Ratio Cut	123
4.4	“Choppiness” in the L1 Rates	124
4.5	TDC Residuals	125
4.6	TDC Distribution of a Transit Run	126
4.7	ON+231 livetime	127
4.8	Reconstructed Arrival Times	129
4.9	Slewing Correction	130

4.10	Timing Resolution	132
4.11	Spherical Showerfront	135
4.12	Reconstructed RA and DEC	136
4.13	χ^2 distributions for ON and OFF data	137
4.14	χ^2 distributions of simulated protons and γ showers	138
4.15	χ^2 Cut Efficiency	140
5.1	Integral Flux Dependence on the Spectral Index	147
5.2	STACEE-32 ON+231 Integral Flux Result	155
5.3	EGRET ON+231 Flux with Upper and Lower Bounds	157

List of Tables

1	γ -ray astronomy nomenclature	viii
2	Acronyms	x
2.1	Properties of the STACEE DTIRCs.	67
2.2	Specifications of the Photonis XP2282 photomultiplier tube.	69
2.3	Current trip conditions.	83
3.1	Run Summary	100
3.2	Effect on χ^2 distribution of time cuts	103
3.3	Statistics of proton simulation.	105
5.1	ON+231 data significance: basic cuts only	143
5.2	ON+231 data significance with quality cuts	144
5.3	Systematic uncertainty summary	154

Chapter 1

Introduction

1.1 VHE γ -ray Astronomy: Review of a Young Field

For millennia people have observed the night sky. Until the 20th century these observations were based solely upon the visible light spectrum. Since the advent of radio astronomy we have been probing the cosmos over a greater range of the electromagnetic spectrum. Simply stated, γ -ray astronomy is the exploration of the upper energy frontier of the electromagnetic spectrum. Because the technology enabling the observation of high energy photons is rather recent, γ -ray astronomy is one of the youngest disciplines in astronomy. The field was truly opened in the 1970s, with the advent of new astronomical instruments based on the technology used in nuclear and particle physics. Since γ -rays have wavelengths much smaller than the atomic scale, conventional methods for observing photons in this energy range (> 1 MeV), such as focusing with mirrors and lenses, simply don't apply. For this reason the progress in γ -ray astronomy (and high energy astrophysics) has been intimately linked to the development of new detection techniques. Thus

VHE γ -ray astronomy is very much an experimentally (or observationally) driven field.

1.1.1 Satellite-Based Experiments

The earliest observations of celestial γ -rays were performed in the 1960s with simple satellite detectors. Many of the first satellites capable of detecting γ -rays were in fact missions designed to detect γ -rays produced in nuclear detonations. Gamma Ray Bursts (GRB) were first discovered with these satellites. Unfortunately the early detections of GRBs obtained by the military were kept secret for decades. In 1972 observational high energy γ -ray astronomy was begun with the deployment of the SAS-II satellite [1]. The SAS-II instrument was used to observe high energy γ -rays from the Vela pulsar as well as the Crab and Geminga [2].

The next γ -ray telescope to be deployed was the COS-B telescope. The field of γ -ray astronomy was widened considerably when one considers that COS-B detected 25 γ -ray point sources (including the first extragalactic γ -ray source 3C279) and the diffuse γ -ray glow of our own galaxy [3].

1.1.1.1 EGRET: A great leap forward

The field of γ -ray astronomy took a great leap in 1991 when NASA's Compton Gamma Ray Observatory (CGRO) was launched. The CGRO was one of NASA's Great Observatories (along with the Hubble Space Telescope (HST) and the Chandra X-ray telescope). The CGRO, depicted in Figure 1.1, carried four independent instruments covering different energy ranges in the γ -ray spectrum: BATSE (20-600 keV), OSSE (0.05-10 MeV), COMPTEL (0.8-30 MeV) and EGRET (20 MeV-10GeV). With a mass of 17 tonnes, the CGRO was the largest payload placed in

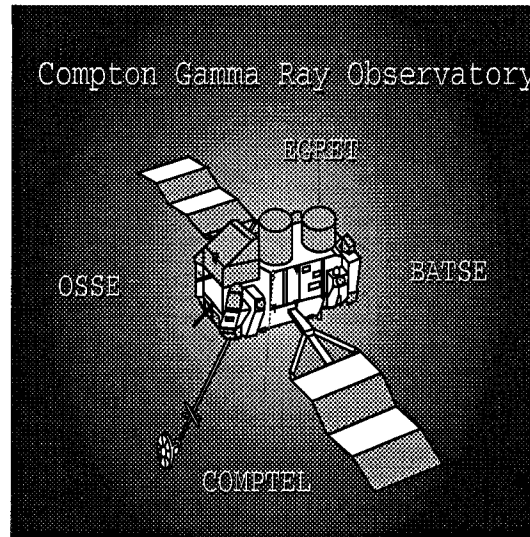


Figure 1.1: NASA's Compton Gamma Ray Observatory and its four instruments. Note that there were eight BATSE detectors, one on each corner of the CGRO.

space at the time of its launch. After 9 years of operation the satellite was decommissioned in 2000 when the gyroscopes which steered the spacecraft showed signs of failure.

The CGRO instruments spanned an energy range from 20 keV to 10 GeV. The most important instrument for high energy γ -ray astrophysics was EGRET (Energetic Gamma Ray Telescope). The upper limit of the EGRET energy range was determined primarily by the low flux of γ -rays rather than the intrinsic performance of the detector. At this energy (roughly $E > 10$ GeV) the power law nature of γ -ray energy spectra (usually $\frac{dN}{dE} \sim E^{-\alpha}$ where $\alpha \sim 2$), results in a flux that is so low that a telescope with EGRET's effective area, becomes statistically limited. Due to the limited payload size of current launch vehicles, this problem is common to all satellite experiments.

In spite of this limit, the EGRET instrument was an exemplary telescope for

γ -ray astronomy. The basic detection process employed by EGRET was e^+e^- pair production. Incoming γ -rays produce e^+e^- pairs due to the 27 layers of tantalum foil sandwiched between 28 separate spark chambers in the upper part of the detector. The spark chambers record the trajectories of these e^+e^- pairs, which can then be used to calculate the initial direction of the γ -ray. The energy of the γ -ray is measured with a sodium iodide crystal calorimeter. The entire detector is covered by a scintillation anti-coincidence dome. If a charged particle (which are much more numerous than γ -rays) is detected passing through this dome the event is vetoed. Time-of-flight counters are used to discriminate between upward (from the earth) and downward moving γ -rays. These components are illustrated and labelled in figure 1.2. A more detailed explanation of the EGRET instrument components and its performance is beyond the scope of this thesis but can be found in [4].

The third EGRET catalog (shown in figure 1.3) contains 271 point sources [5]. Of these sources, 66 are high confidence Active Galactic Nuclei (AGN) identifications with an additional 27 sources that are possibly associated to AGN. There are also 6 pulsars, 1 radio galaxy (Cen A), 1 normal galaxy (LMC) and one solar flare. EGRET has also measured the diffuse γ -ray emission of our own galaxy along the galactic plane and at high galactic latitudes. The detectors of the Burst and Transient Source Experiment (BATSE) aboard CGRO were used as triggers with EGRET to measure the high energy γ -ray spectra of dozens of GRBs. The most numerous class of objects in the EGRET 3rd catalog is actually composed of unidentified sources, of which there are 170! The reason for this large number of unidentified sources was EGRET's "error box". At 1 GeV, EGRET's angular resolution was 0.8° . Because of this large pointing error more than one optical counterpart could be associated with many EGRET detections. This source confusion lead to the large number of EGRET unidentified sources.

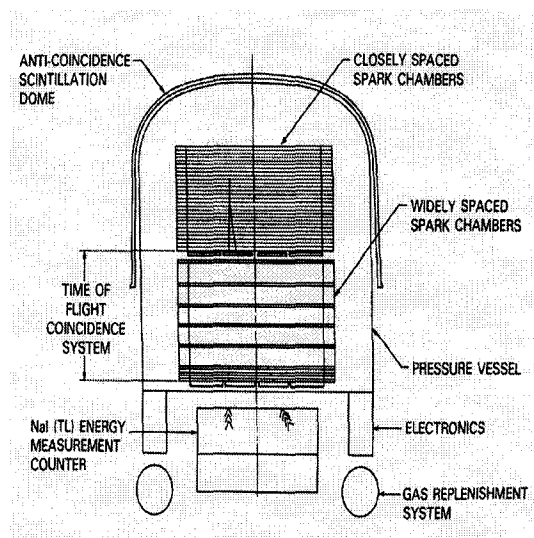


Figure 1.2: Schematic of EGRET with the various components of the telescope labelled. From top to bottom the detector is a collection of spark chambers sandwiched between a time of flight system, followed by a calorimeter to measure the total energy of the incoming γ . The entire system is covered by an anti-coincidence veto that signals the passage of charged particles.

EGRET's widening of the field of γ -ray astronomy can be understood quantitatively when we compare it to its predecessors. Roughly speaking, EGRET measured 10 times as many sources as the SAS-II and COS-B satellites combined. Not only did EGRET detect more sources, but it did so with greater angular accuracy, sensitivity and energy resolution. Despite CGRO's demise in 2000, the large number of unidentified sources will provide the field with many new targets. No satellite-based experiment to replace CGRO is scheduled until 2006 when the Gamma Ray Large Area Space Telescope (GLAST) [6] instrument is scheduled for launch.

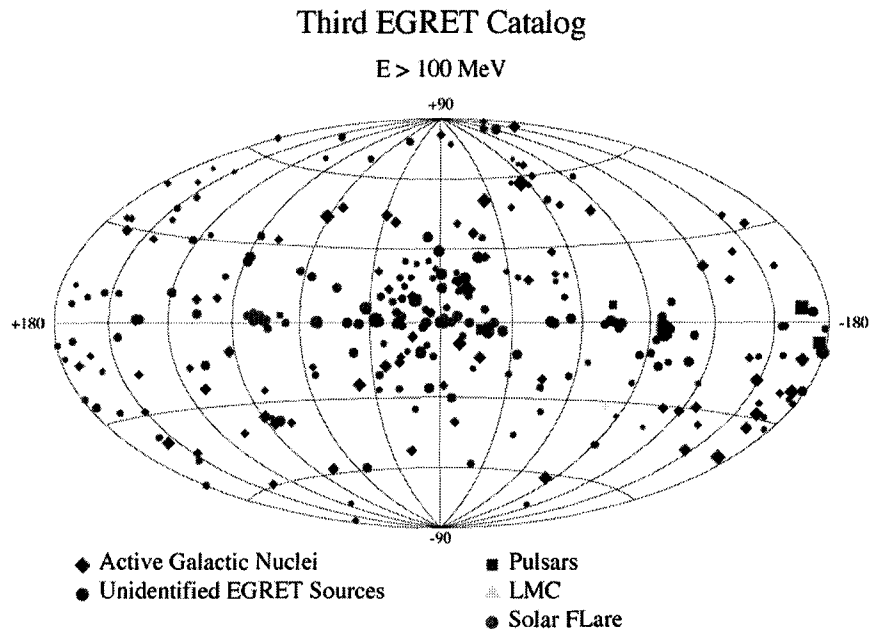


Figure 1.3: Sources of γ -rays at energies above 100 MeV from the 3rd EGRET catalog, plotted in galactic coordinates. The size of the points is proportional to the intensity of the γ -ray sources. Unidentified sources clearly outnumber any other class of source in the distribution.

1.2 Ground-based VHE γ -ray astronomy

The greatest shortcoming of satellite experiments is an earth-based experiment's greatest asset: effective area. As previously explained, due to the limited size of payloads and the power law distribution of γ -ray flux, satellite-based telescopes have not observed astrophysical objects at energies >30 GeV. In contrast, imaging earth-based experiments have demonstrated observability from 250 GeV and beyond. Of course, earth-based experiments have their own drawbacks. For most wavelengths of light the atmosphere poses serious problems. For ultraviolet light, X-rays and γ -rays direct observations by ground-based experiments are impossi-

ble. At sufficiently high energies indirect γ -ray observations are possible by using the electromagnetic cascades or showers created by VHE γ -rays. These showers are created when VHE γ -rays strike the upper atmosphere and interact with the matter in the atmosphere. In a sense one uses the atmosphere itself as a detector. Before discussing ground-based VHE astronomy, an introduction to the physics of extensive air showers (EAS) is needed.

1.2.1 Electromagnetic Showers

When high energy photons interact with matter a shower of lower energy particles is created. To understand this cascade we can create a simple model by using the two well known quantum electro-dynamics (QED) processes of pair production and bremsstrahlung iteratively. If a high energy photon of energy E_0 penetrates a material, it will pair produce, on average, after one radiation length. The energy of the initial photon will be split evenly between the two leptons. The e^+ and e^- will then also travel one radiation length, on average, before emitting a photon through bremsstrahlung. So at two radiation lengths there will be 4 particles (2 photons and an e^+e^- pair), each with energy $E_0/4$, see figure 1.4. This process will continue until the electrons and positrons created by the pair production process have energies that have slipped below the critical energy, E_c , the energy at which ionization becomes a more important energy loss process than bremsstrahlung.

From this simple model we can make a few observations. After t radiation lengths the number of particles will be

$$N \approx 2^t \tag{1.1}$$

and the average energy of these particles will be

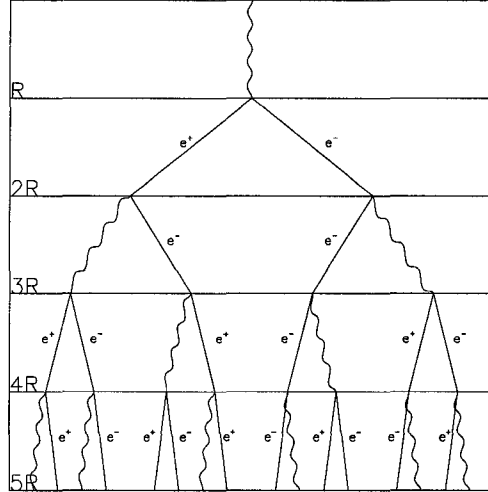


Figure 1.4: A simple model of electromagnetic shower evolution using only the two processes of bremsstrahlung and pair production in an iterative manner. The number of particles doubles at every radiation length, thus the energy per particle is halved at every radiation length. This continues until the energy of the electrons falls below the critical energy, E_c .

$$E(t) \approx \frac{E_0}{2^t} \quad (1.2)$$

If we assume that the shower stops at the critical energy, $E_c \approx 85$ MeV in air then:

$$E(t_{max}) \approx \frac{E_0}{2^{t_{max}}} = E_c \quad (1.3)$$

solving for t_{max} , the maximum penetration depth of the shower is

$$t_{max} = \frac{\ln \frac{E_0}{E_c}}{\ln 2} \quad (1.4)$$

and the maximum number of particles produced in an electromagnetic shower can

be expressed in terms of the initial photon's energy and the critical energy

$$N_{max} \approx \frac{E_0}{E_c} \quad (1.5)$$

The width of a shower can be characterised by the Molière radius. The Molière radius is the radius of a cylinder containing, on average, 90% of the total energy of the shower. It can be expressed as a function of the critical energy:

$$R_M = L_{rad} \frac{E_s}{E_c} \quad (1.6)$$

where E_s is 21.2 MeV and L_{rad} is the radiation length for a material. The point at which the shower achieves its maximum number of particles is called shower maximum. In this model shower maximum occurs in the last step but in practice, the shower exists for a relatively long distance after reaching shower maximum, see figure 1.5.

1.2.2 Atmospheric Showers

Predicting the evolution of electromagnetic showers in the atmosphere is very complicated. The atmosphere's density varies as a function of altitude and there is no way to explicitly test the atmosphere's response to high energy photons. The atmosphere's depth also poses significant problems. Using equation 1.4 from the previously described model, and assuming that the density of the atmosphere is constant with a radiation length of 300 m for air, the shower maximum depth of a 100 GeV photon striking the upper atmosphere would be ≈ 3 km. Using equation 1.5 and the value of E_c in air, we can calculate the Molière radius of the shower to be ≈ 75 m. Figure 1.5 shows the maximum penetration depth in the atmosphere of showers of varying energies.

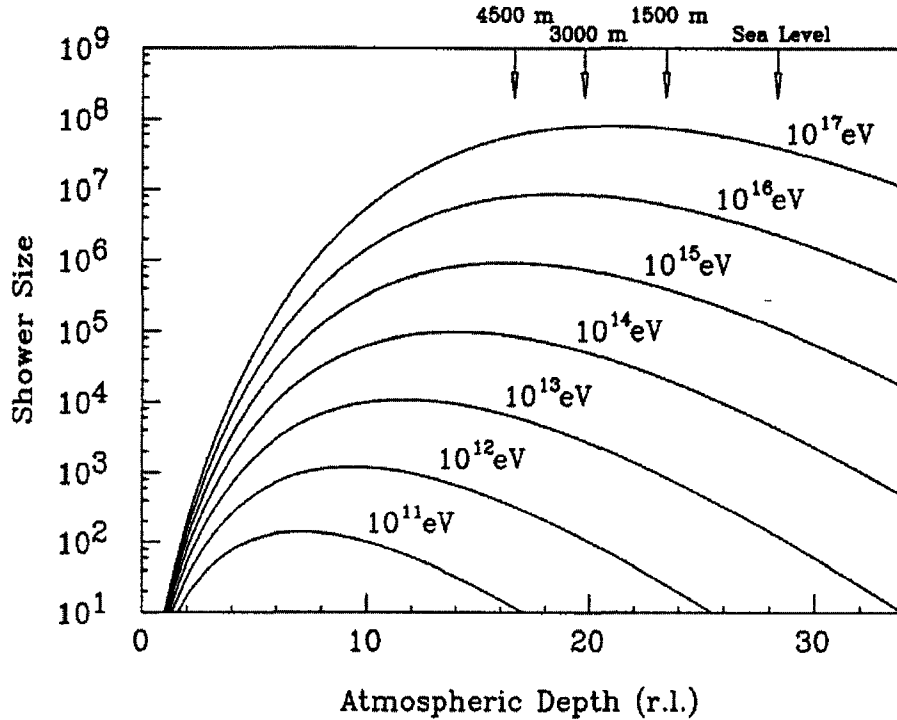


Figure 1.5: Shower size (i.e. the number of particles in the shower) as a function of penetration depth of γ -initiated electromagnetic showers in the atmosphere for energies of the primary ranging from 100 GeV (10^{11} eV) to 100 PeV (10^{17} eV).

For all but the largest energies and highest elevations, secondaries from atmospheric showers do not reach the earth’s surface. However, some experiments have been designed to detect these secondaries. These experiments are aptly named “air shower arrays”. Air shower arrays sample the charged particles that reach the ground and use fast timing between detector elements, with a measure of the shower core location on the ground, to estimate the primary particle’s direction and energy. The energy of the primary γ -ray is calculated from the number of secondaries measured in the array. At these high energies the γ -ray flux is so small that the effective area of these arrays must be very large. The largest of

these arrays, CASA-MIA, had an effective area of 230 000 m^2 .

Air shower arrays generated a tremendous amount of excitement in the 1980s with several reported detections of γ -ray sources at energies ranging from 1 TeV to 1 PeV. The most notable of these sources were the Crab Nebula, and the well known binary X-ray sources Cygnus X-3 [7] and Hercules X-1 [8]. Unfortunately these detections (with the exception of the Crab) were not confirmed by subsequent generations of more sensitive ground-based experiments. At Ultra-High energies, large scintillator arrays, such as CASA [9], equipped with muon detectors for hadronic shower rejection, set upper limits on γ -ray emission from sources above 100 TeV that were orders of magnitude below the earlier “detections”.

1.2.3 Čerenkov Light from EAS

Although, charged secondaries from γ -initiated showers seldom propagate through the atmosphere to the earth’s surface, some energy from these showers does propagate all the way through the atmosphere. In particular, this is the case for Čerenkov radiation, which occurs when a charged particle traverses a material with a speed greater than the speed of light in that medium. In such cases an electromagnetic shock wave is created. This shock wave is comparable to the sonic “boom” produced when an object travels faster than the speed of sound in a medium, or to the bow waves created by boats that travel faster than the speed of wave propagation in water. In such cases the shock wavefront is conical in shape. This effect is shown schematically in Figure 1.6. For a Čerenkov wavefront the half angle of the Čerenkov cone is given by the equation:

$$\cos \theta_C = \frac{1}{\beta n(\lambda)} \quad (1.7)$$

Where $\beta = v/c$ and $n(\lambda)$ is the index of refraction of the medium as a function of the wavelength. When incident on a surface perpendicular to the direction of

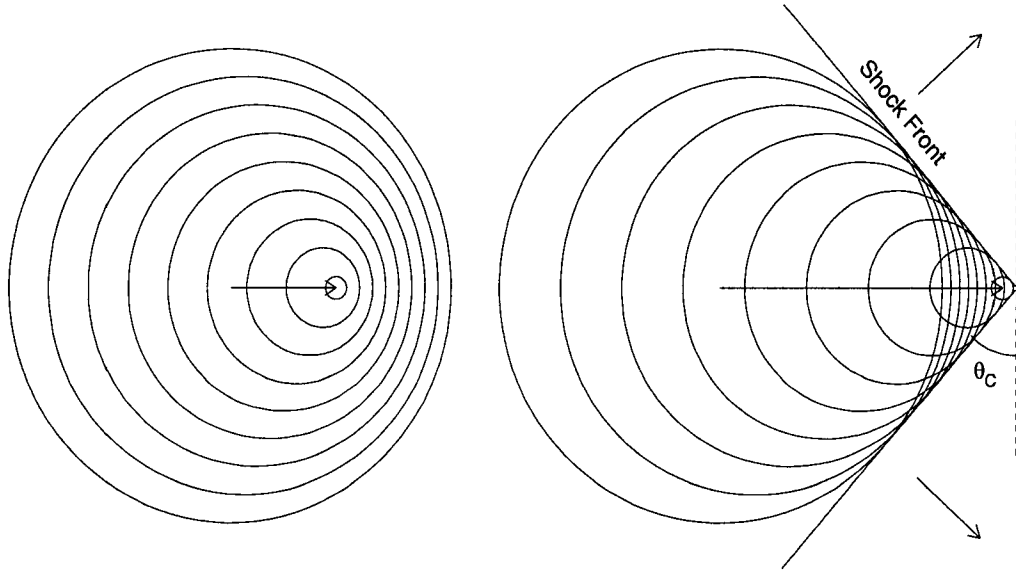


Figure 1.6: Two particles travelling through a medium, one at a speed below the speed of light (left), the other above (right). In both cases spherical wavefronts emanate from the moving particle. When the particle exceeds the local speed of light a conical Čerenkov shock front is created.

propagation of the particle, these Čerenkov photons will form a disk, or when a particle only exists for a brief amount of time, or when its speed exceeds the local speed of light very briefly, an annulus or ring. Figure 1.7 illustrates how Čerenkov rings and filled circles are created in the atmosphere. The number of Čerenkov photons emitted along a path length dx in a wavelength interval of $d\lambda$, is:

$$\frac{d^2N}{dx d\lambda} = \frac{2\pi Z^2 \alpha}{\lambda^2} \left(1 - \frac{1}{\beta^2 n^2(\lambda)} \right) \quad (1.8)$$

where Z is the particle's charge and α is the fine structure constant. If $n(\lambda)$ is constant the number of photons emitted as a function of wavelength has the form $dN/d\lambda \propto 1/\lambda^2$. Consequently the bulk of Čerenkov radiation is emitted in the ultraviolet and blue parts of the spectrum.

Typically the index of refraction of the atmosphere at sea level is 1.000283 [11].

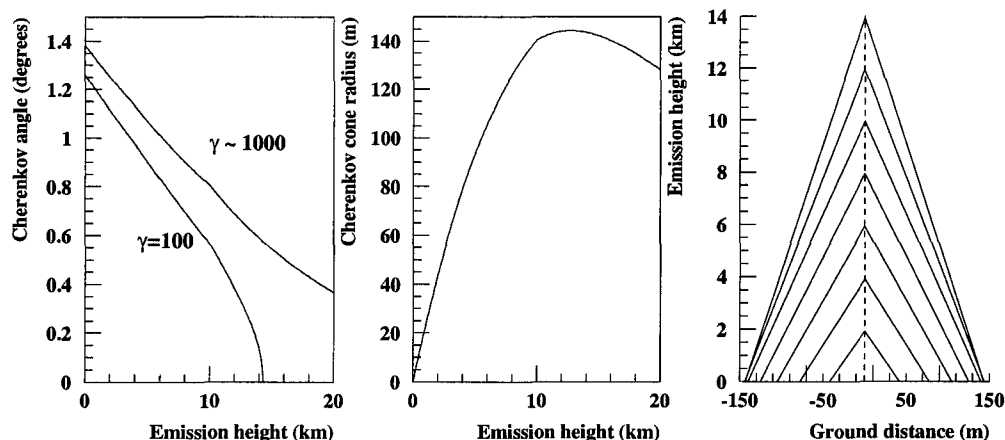


Figure 1.7: Čerenkov emission for a single particle in the atmosphere. *Left:* Čerenkov angle for particles with $\gamma = 100$ and 1000 . *Centre:* Čerenkov cone radius on the ground as a function of emission height. *Right:* Diagram showing the production of Čerenkov light on the ground produced by a particle from [10]. Each pair of lines represents the opening angle of the Čerenkov cone produced at that altitude.

Thus for values of $\beta \sim 1$ for atmospheric showers, the half angle of the Čerenkov cone is approximately $\sim 1^\circ$. In an electromagnetic shower, the vast majority of the particles produced are e^+e^- pairs. The amount of Čerenkov light produced by the shower is proportional to the number of e^+e^- pairs produced; in this manner if the number of Čerenkov photons reaching the earth is measured one can use the atmosphere as a calorimeter and infer the energy of the primary particle from the total Čerenkov light yield.

Since most of the particles travel close to the central axis of the shower, the Čerenkov photons produced will be tightly aligned and will form a relatively uni-

form disk or pancake of Čerenkov light. This disk is usually of the order of ~ 1 m thick (or about 3-5 nsec). The majority of the Čerenkov photons will fall within a circle of radius 100-200 m on the ground. Typically the area with the highest photon density is a ring of radius 100-150 metres. The radial distribution of the photon density is plotted in figure 1.8.

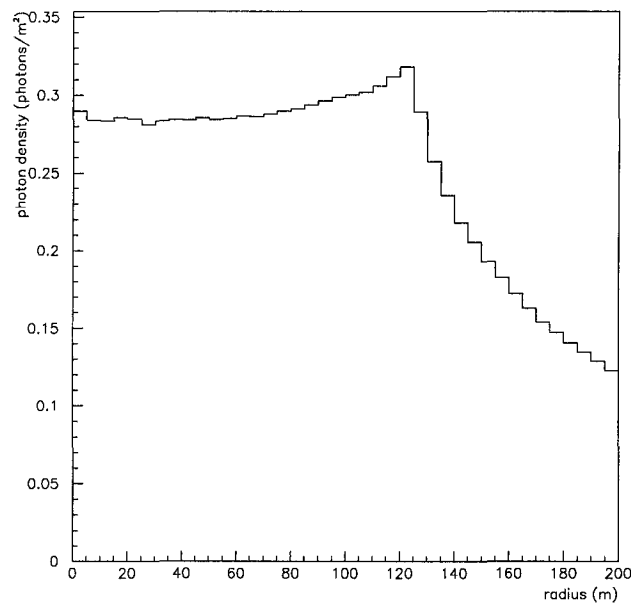


Figure 1.8: Average Čerenkov photon density as a function of radius at the ground from simulated 100 GeV γ -rays at zenith. Note the characteristic peak of such distributions at a radius of 120 m.

1.2.4 Differentiating Between Proton- and γ -induced Showers

The flux of cosmic rays in an acceptance solid angle of 1 msr is at least four orders of magnitude larger than that from the strongest known γ -ray source[12]. Because these charged cosmic rays (which are mostly hadronic in nature) also produce Čerenkov radiation, it is important to learn how to distinguish between hadron initiated showers and electromagnetic showers. The main intrinsic differences between hadronic and electromagnetic showers are in their composition and interaction mechanisms. Secondaries in hadronic showers, initially created by strong interactions (those governed by quantum chromodynamics (QCD) instead of QED), typically have more transverse (with respect to the direction of the primary) momentum, p_T , than those of electromagnetic interactions. γ -induced showers are composed almost exclusively of e^+e^- pairs while hadronic showers produce pions ($\pi^{\pm,0}$) and muons (μ^{\pm}) in addition to e^+ and e^- . These differences can't be observed directly, but they are at the root of some measurable phenomenological differences, such as lower Čerenkov yield and shower front inhomogeneity, between γ - and proton-initiated showers.

lower Čerenkov light yield in hadronic showers The more massive particles produced in hadronic showers have higher Čerenkov thresholds, and therefore produce a lower density of Čerenkov photons. Figure 1.9 shows the result of simulations where the atomic number of the initial particle is varied. We also see that at energies below 100 GeV light emission from protons starts to drop off whereas the yield for γ -initiated showers stays proportional to the energy of the primary. The presence of more p_T in hadronic showers causes a greater lateral spread between secondaries in the shower, this has the effect of spreading the Čerenkov light over a greater area on the ground.

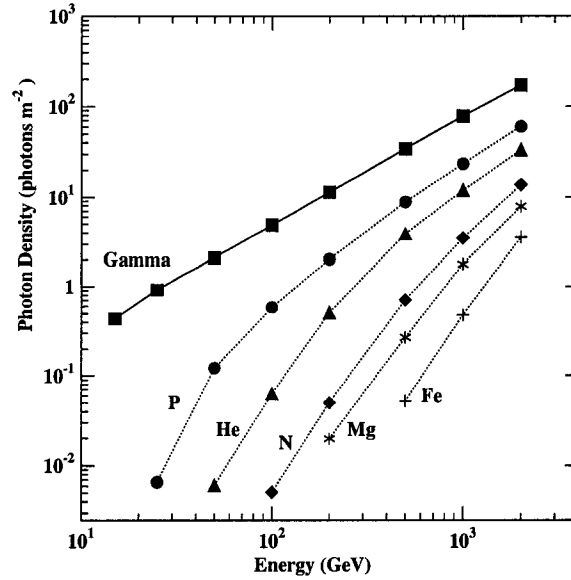


Figure 1.9: Čerenkov photon density as a function of energy for different primaries. One can clearly see that γ -rays generate a greater Čerenkov photon density than proton showers, especially at lower energies. The Čerenkov yield is also a strong function of the primary mass: the photon yield drops very quickly with the primary mass.

Muons, because of their greater mass, ($M_\mu > 200M_e$) do not shower in the atmosphere and will often reach the ground. Unlike electrons they will not create more charged particles that in turn radiate more Čerenkov light, thus further reducing the amount of Čerenkov light produced in proton-initiated showers. Figure 1.10 illustrates these differences in light yield on the ground.

inhomogeneity of hadronic showers The composition and p_T of hadronic showers also play roles in making these showers less homogeneous than γ -initiated showers. In hadronic showers nuclear collisions can generate hadronic fragments with large p_T , particularly in the initial stages of shower development.

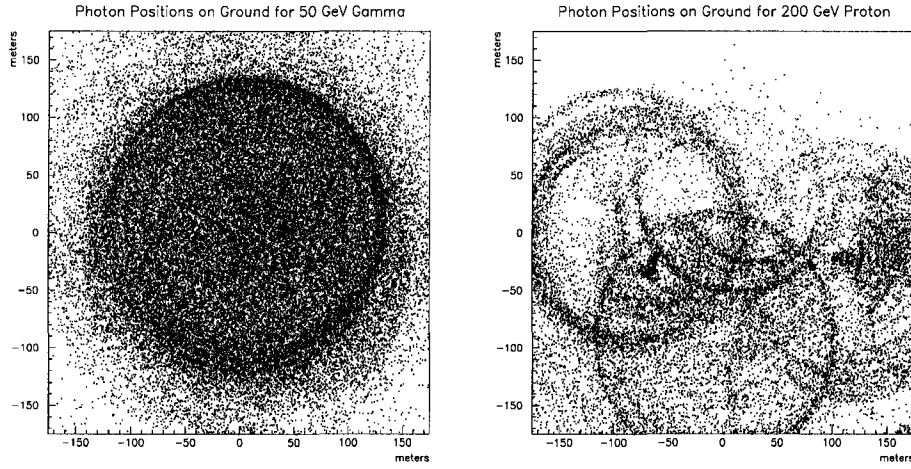


Figure 1.10: Position of Čerenkov photons reaching the ground from a simulated 50 GeV γ -initiated shower (left) and from a simulated 200 GeV proton-initiated shower. γ -initiated showers form uniform discs while the proton shower photon distribution is much more irregular and sparse. One can also see the individual Čerenkov rings (annuli) caused by short lived pion initiated electromagnetic showers.

This causes much of the shower's energy to be contained in a small number of particles which can create their own sub-showers. In particular energetic neutral pions usually decay to two photons that can then initiate their own, short lived electromagnetic showers. This inhomogeneity distorts the timing profiles of cosmic ray showers enough that differences in arrival times on the ground can be observed. Figure 1.11 shows the differences in timing profiles between proton and γ -initiated showers.

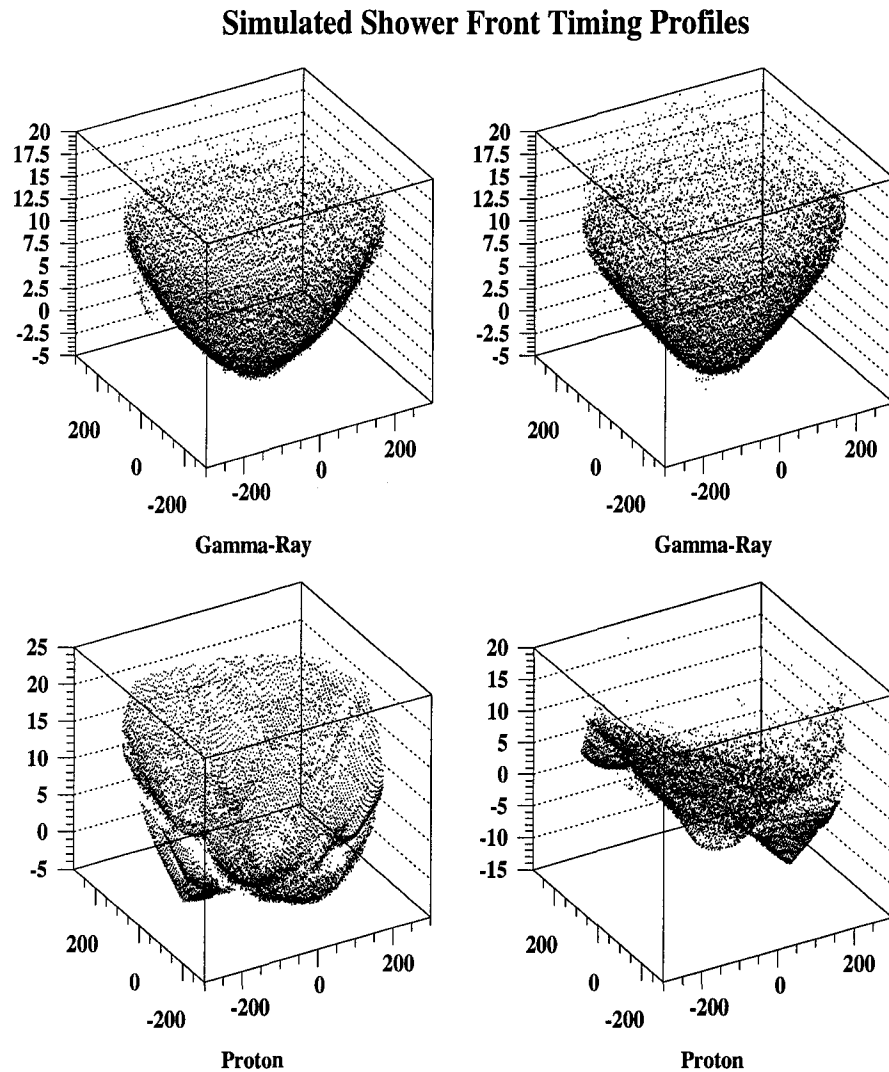


Figure 1.11: Simulations of γ -ray and proton showers. The arrival times of the shower wavefronts (in nsec) are plotted on the z-axis against the x-y arrival position in metres. Proton-initiated showers have a more irregular shape than γ -initiated showers.

1.2.5 Imaging Atmospheric Čerenkov Telescopes

The field of ground-based γ -ray astronomy matured quickly in the late 1980s. One pioneering instrument in particular was responsible for this. In 1985 the

Whipple telescope atop Mount Hopkins saw a clear signal (5.6σ) from the Crab [13]. Whipple is an Imaging Atmospheric Čerenkov Telescope (imaging ACT or IACT). IACTs usually consist of a multifaceted primary mirror assembly with a pixelated camera situated at its focus. Figure 1.12 shows a schematic of the Whipple telescope. The entire structure can rotate in azimuth and elevation to track sources through the night.

The camera for an imaging ACT typically consists of a tight array of photomultiplier tubes (see figure 1.13). The telescope electronics trigger and record the data from the photomultiplier tubes, when a sufficient number of tubes see a preset number of photons. Because of the faint amount of light in the Čerenkov images, the telescope must be operated on clear moonless nights: otherwise the sensitive phototubes would be damaged and/or background light levels would be too high. The pixelated camera allows one to image the shower produced in the upper atmosphere. Analysis of these images can then be used for hadronic shower rejection to increase the purity of the sample. The rejection of hadronic showers is accomplished by measuring the position and shape of the image recorded by the phototube camera. γ -ray showers usually have an elliptical shape that points towards the centre of the camera. Hadronic showers tend to be amorphous, consisting of more than one area of triggered tubes and have no preferential pointing direction in the camera. Figure 1.14 illustrates idealised images of γ -ray and hadronic showers. Further discussion of the proton rejection properties of IACTs is beyond the scope of this thesis but can be found in [14, 12].

The initial 1985 Whipple result was the result of 34 hours of observation. The 1998 version of the Whipple telescope detected a 20σ signal from the Crab in 30 hours. Whipple's success and technological improvements in instrumentation paved the way for many groups around the world to build their own IACTs. Today there are 7 such telescopes distributed over both hemispheres. The lowest energy

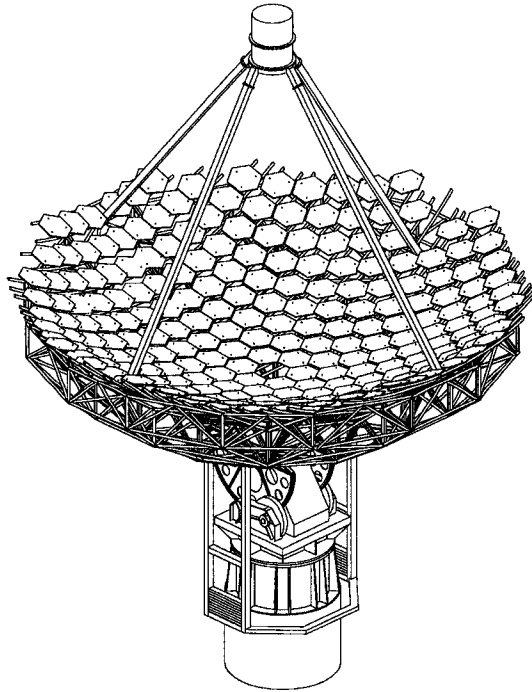


Figure 1.12: Schematic of the Whipple telescope. The 10 m diameter mirror assembly has a camera located 7 m from the centre of the dish. The first incarnation of the Whipple camera in 1983 consisted of 37 phototubes. The latest version of the Whipple camera has 490 phototubes.

threshold of such telescopes is presently ~ 250 GeV.

The biggest collective result of these observations has been the relative dearth of sources. To date only 8 sources have been observed at high significance. Only 4 of these sources have been confirmed at high significance by multiple experiments [15]. Figure 1.15 shows the 8 sources plotted in galactic coordinates. Comparing figures 1.15 and 1.3, we see that the sky at TeV energies is a desert compared to the hundreds of sources seen by EGRET at GeV energies. Even though one would expect fewer sources at high energies because of the rapidly diminishing fluxes this result is still surprising. If the EGRET spectra for many sources are

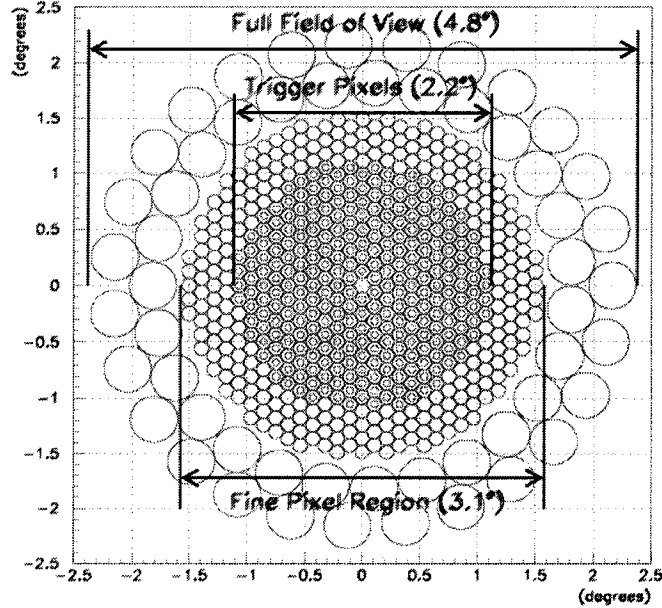


Figure 1.13: Schematic of the fine grained CAT telescope PMT camera. The circles are PMTs of various sizes.

extrapolated to IACT energies, the upper limits set by higher energy threshold experiments usually lie well below the EGRET extrapolations. Figure 1.16 displays the spectra for two such AGN. The AGN observed at these energies have been the subject of many multi-wavelength campaigns aimed at understanding the emission mechanisms of AGN. At TeV energies blazars have been observed to vary on hourly time scales. Such rapid variability has been shown to imply that the emission region is extremely compact: on the order of a few light hours across [17]. This flaring activity has given considerable support to the unified AGN scheme (discussed in section 1.3.2.1) that supposes that a supermassive black hole is involved in the emission of AGN.

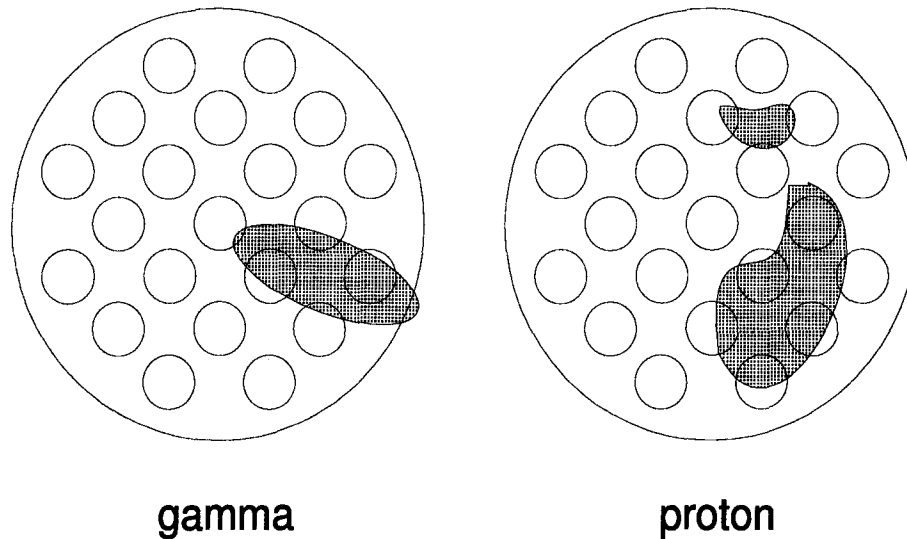


Figure 1.14: Schematic of a proton and a γ -ray shower viewed in the focal plane of an IACT. γ -ray showers tend to have an elliptical shape and point towards the centre of the camera.

1.2.6 The Unobserved Gap and the Need for New Instruments

What is striking in any review of the state of high energy γ -ray astronomy, both ground-based and satellite-based, is the difference in the number of sources observed in the two distinct energy ranges covered by these experiments. Satellite experiments have a statistically imposed upper limit in energy due to the finite size of the detectors that can be launched into space. All satellite experiments (both past and proposed) have an upper energy limit of ≈ 10 GeV. The most advanced imaging IACTs have detection thresholds starting at 250 GeV. As a result, there is an unobserved energy gap in the γ -ray spectrum, spanning roughly a decade in γ -ray energy where no existing detector can observe. This unopened window remains one of the last unexplored regions of the electromagnetic spectrum. The

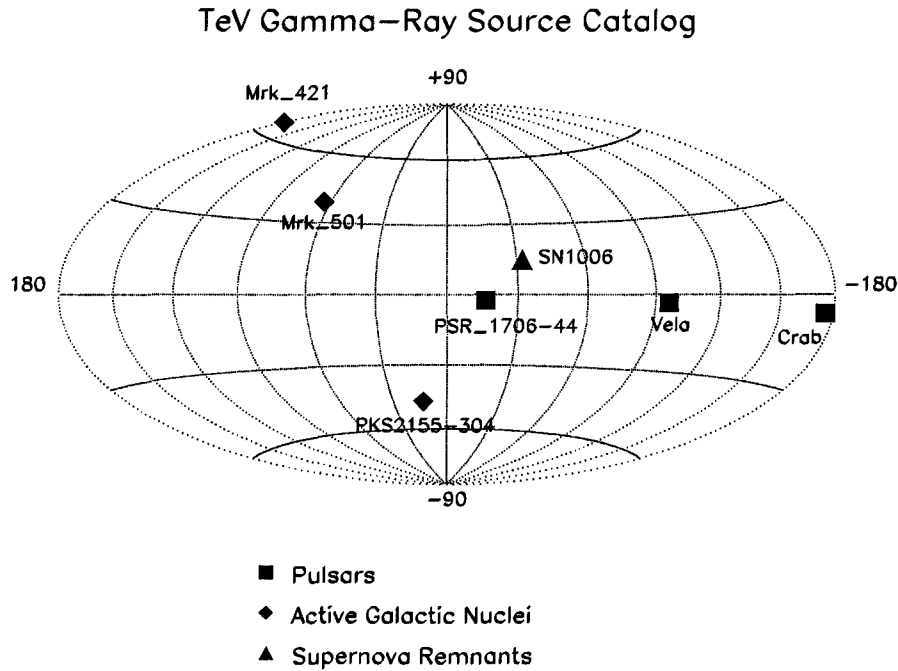


Figure 1.15: Source list adapted from [15]. The TeV γ -ray sky is sparsely populated. The supernova remnant RXJ713.7-3946 is not shown because it would be obscured by PSR 1706-44 on this plot. This figure also doesn't include the AGN 1ES-2344 which was recently observed (spring 2001) at IACT energies.

reasons to explore this gap go far beyond simple curiosity. The large drop in the number of sources across this energy range is an indication that some physical process is involved either in the emission mechanisms of the sources themselves or in the absorption of their signals.

If the source spectral cutoffs are intrinsic (i.e. in the sources themselves), studying where the cutoffs fall in the energy spectra will give important insights into the mechanisms responsible for the γ -ray emission.

If we consider AGN, studying the spectral cutoffs as a function of distance to the source might be the best way to measure the intergalactic infrared field (see

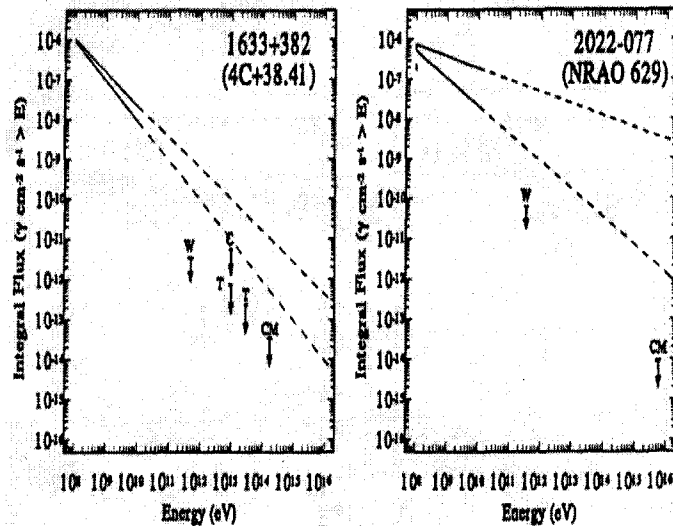


Figure 1.16: The extrapolated EGRET integrated spectra (solid lines represent the part of the spectra where EGRET data exists, and the dashed lines are the extrapolations of these data) and the upper limits from various experiments (W=Whipple, T=Tibet Air Shower Array, C=Cygnus experiment, CM=CASA-MIA) for two EGRET detected AGN. The presence of multiple spectra indicates individual measurements taken at different epochs in the CGRO observations [16].

section 1.3.1.2). Because of their rapid time variability and broad emission spectra, the key to understanding the mechanisms that power these AGN is simultaneous multi-wavelength campaigns. Observations in this gap would be crucial for such campaigns.

1.3 Astrophysics of the γ -ray sky

Particle physics and astronomy merge naturally when one turns an eye towards cosmic and γ -ray physics. This is evident when one reviews the earlier history of particle physics: the positron, pion, muon and kaon were all discovered while

studying cosmic rays with instruments initially developed with nuclear and atomic physics in mind. As particle accelerator technology improved, cosmic rays were no longer needed to perform nuclear and particle physics. However, in addition to their use in early particle physics cosmic rays were interesting in themselves: the sources of these particles and the objects that could create and accelerate them were unknown. Because of the magnetic fields of the earth and our own galaxy, charged cosmic rays can not give very much information about their celestial origins. A magnetic field of ~ 1 micro Gauss (μG) exists throughout the Milky Way. The radius of the trajectory of a charged particle in a magnetic field perpendicular to the motion of the particle is described by:

$$R = 0.01 \cdot \left(\frac{p}{ZB}\right) \quad (1.9)$$

where p is the momentum in $\frac{\text{TeV}}{c}$, the magnetic field B is in μG , Z is the charge of the particle in terms of electronic charge and the radius, R , is given in parsecs. Thus all protons with energies below $\sim 10^{18}$ eV coming from galactic sources ~ 10 kpc away have lost all directional information [12]. Since γ -rays (and neutrinos) are not charged they are not deviated by this magnetic field and they conserve their directional information. It is for this reason that extragalactic point sources can be observed with γ -rays in the TeV regime. Neutrinos also conserve their directional information; but, since they only interact with matter via the weak force, they are much more difficult to detect. In this sense γ -ray astrophysics is a natural outgrowth towards newer energy frontiers of more traditional areas of astronomy: photons are still used to observe the sources. Exactly how these high energy photons are generated is still not known. Most models postulate violent, non-thermal phenomena associated with supernova and black holes.

1.3.1 Physics Processes in γ -ray Astronomy

For the sources that are studied with STACEE there are two basic models of particle acceleration that lead to emission of VHE γ -rays: shock wave acceleration and acceleration in electric fields. Shock wave acceleration (also known as first order Fermi acceleration) is based on the model of second order Fermi acceleration [18]. When a shock wave propagates through an interstellar medium, charged particles that cross the shock wave gain energy. In the rest frame of the shock wave, particles upstream and downstream move towards the shock, thus gaining multiple crossings of the shock front and imparting more energy to the charged particles with each crossing [19]. Upon crossing the shock front the particles achieve a thermalised state, where the particle directions are random. A small fraction of these particles have directions that will allow them to collide once more with the shock front. In this manner the ratio of particles left in the acceleration process decreases with each shock front crossing. Figure 1.17 demonstrates how this process accelerates charged particles. The shock front acceleration process reproduces the general power law spectrum that is observed in all γ -ray sources. Shock wave acceleration is believed to be the mechanism responsible for the first step (shock front acceleration in itself doesn't describe how the charged particles transfer their energy to γ -rays) in the production of the high energy γ -rays observed from supernova remnants and AGN jets. Another accepted mechanism for charged particle acceleration is by electric fields. If even a small electric field is present the particle can be accelerated to very high energies, if the field persists over a long enough distance. The electric fields needed for this mechanism to work can be created in disks of rotating charged matter where, the outer regions of the disk rotate at a slower rate than the inner regions. This differential rotation of a conducting disk forms an electric generator known as a unipolar inductor [12]. Accretion disks, believed to exist around black holes, could lead to charged particle acceleration

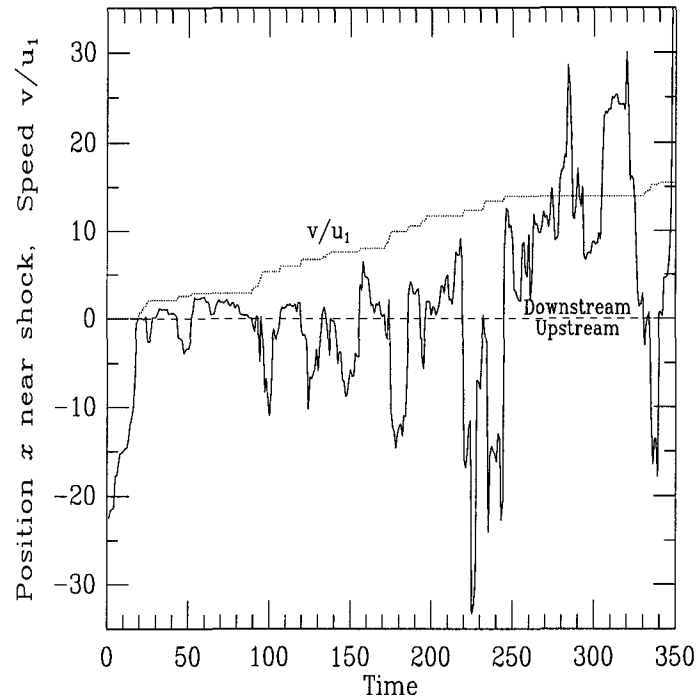


Figure 1.17: Particle position and speed versus time in first order Fermi acceleration. v is the instantaneous particle speed and u_1 is the initial particle speed. The particle's speed increases monotonically with time as the number of shock front crossings increases. The units of time are arbitrary. [20]

in this manner. It has been estimated that accretion disks surrounding neutron stars could give rise to particles with energies up to 10^{17} eV [21].

1.3.1.1 Inverse Compton Scattering and Synchrotron radiation

As previously stated, little can be learned directly about the origin of high energy charged cosmic rays. In order to be observable here on earth, these charged particles must transfer their energy to neutral particles, preferably photons. High energy charged particles can interact with photons via Inverse Compton (IC) scattering. The cross section for this process, σ_c , is given by the Klein-Nishina

equation:

$$\sigma_c = 2\pi r_e^2 \frac{1 + \alpha}{\alpha^2} \left[\frac{2(1 + \alpha)}{1 + 2\alpha} - \frac{1}{\alpha} \ln(1 + 2\alpha) \right] + \frac{1}{2\alpha} \ln(1 + 2\alpha) - \frac{1 + 3\alpha}{(1 + 2\alpha)^2} \quad (1.10)$$

where r_e is the classical electron radius and α is the ratio of the initial photon energy to the electron energy in the rest frame of the electron, $\alpha = \frac{h\nu_i}{m_e c^2}$. In the low energy limit, known as the Thomson scattering limit, where the energy of the initial photon $h\nu_i \ll \frac{m_e c^2}{\gamma}$ (here γ is the Lorentz factor), the final energy of the photon is:

$$h\nu_f \approx \gamma^2 \cdot (h\nu_i) \quad (1.11)$$

The energy of the photon is therefore increased by a factor of γ^2 , which can be very large for highly relativistic electrons. However, the energy gained by the photon has an upper limit of

$$\delta e_\gamma < \gamma m_e c^2 \quad (1.12)$$

In the extreme Nishina-Klein limit $h\nu_i \gg \frac{m_e c^2}{\gamma}$ the energy of the scattered photon is then

$$h\nu_f \approx \gamma m_e c^2 \quad (1.13)$$

In order for IC scattering to occur there must not only be a sufficient density of energetic charged particles, but also of photons. These photons can be generated by synchrotron radiation, as the charged particles rotate in magnetic fields. The energy radiated per turn by a charged particle is:

$$E_{loss/turn} \propto \left(\frac{E_p}{m_p} \right)^4 \frac{1}{r} \quad (1.14)$$

where E_p is the energy of the charged particle, m_p its mass and r the radius of curvature. Since the energy radiated is inversely proportional to the fourth power of the mass of the rotating particle, lighter particles give off much more of their energy, and as such are much more difficult to accelerate to high energies. Protons, which are ~ 2000 times more massive than electrons, radiate much less and are therefore more efficiently accelerated.

The synchrotron radiation generated in the vicinity of AGN and neutron stars usually accounts for the bulk of the X-ray emission from these objects. The higher end of the emission spectra are usually dominated by the IC components of these sources. These two processes form two characteristic and distinct humps (known as the synchrotron and IC peaks) in the emission spectra of many SNR and AGN. The description of these two processes in a single model, where electrons spiraling in a magnetic field generate synchrotron radiation which is then IC scattered by the same population of electrons, is called the Synchrotron Self Compton (SSC) model [22]. SSC models have been devised for AGN and SNRs that reflect the data with great success. Figure 1.18 demonstrates how well this model predicts the differential Crab spectrum.

1.3.1.2 γ -ray absorption via pair production

Attenuation of γ -rays can occur through the pair creation process:

$$\gamma\gamma \rightarrow e^+e^- \quad (1.15)$$

The threshold energy for this reaction is such that the invariant mass of the photons is equal to the rest mass of the electron positron pair:

$$2\epsilon E_\gamma(1 - \cos\theta) \geq (2m_e c^2)^2 \quad (1.16)$$

where ϵ is the lowest of the two photon energies, E_γ is the energy of the high energy γ and m_e is the rest mass of the electron. The cross section for this process is maximised just above its threshold energy so that:

$$\epsilon E_\gamma \approx 2(m_e c^2)^2 = 0.52(\text{MeV})^2 \quad (1.17)$$

Using this relation, we see that TeV γ -rays will preferentially pair create with ~ 0.5 eV ($\lambda \sim 2.5 \mu\text{m}$) photons. This soft photon energy corresponds to photons in

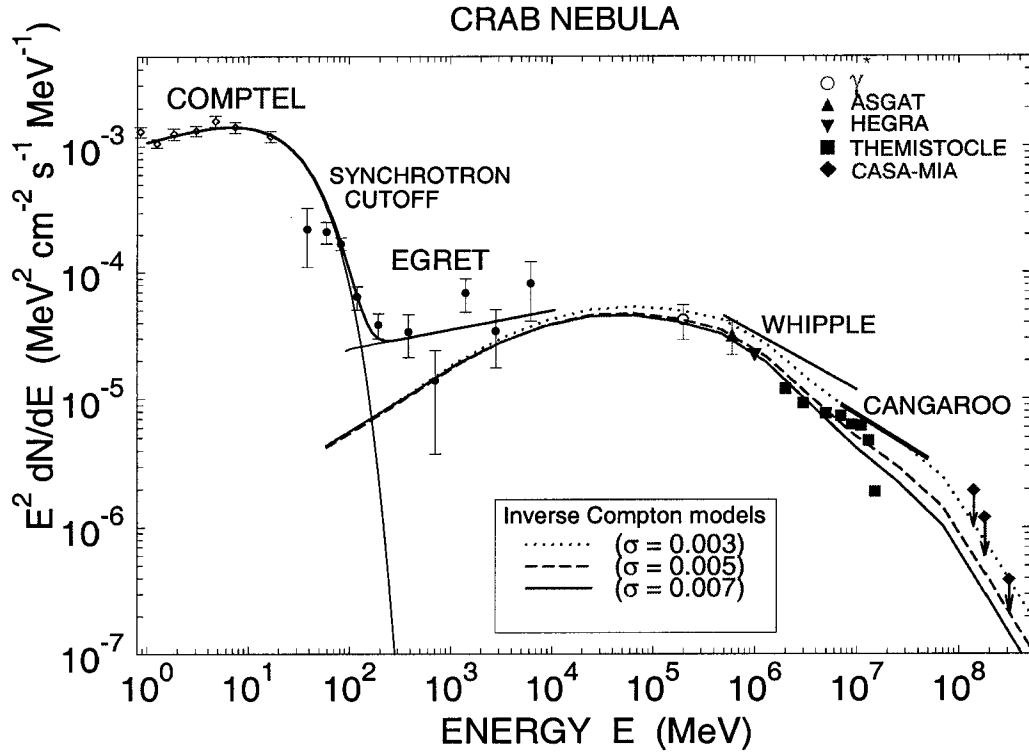


Figure 1.18: Comparison of γ -ray unpulsed emission from the Crab Nebula and predictions of the SSC model, for 3 values of the σ parameter (the ratio of magnetic to particle energy density) [23]. The Crab spectrum is plotted as E^2 multiplied by the differential spectrum. The SSC model agrees with the data over decades in energy.

the intergalactic infrared field (IIR). In order to pair create with the photons from the cosmic microwave background a γ -ray would need an energy of 3×10^{15} eV. Thus, IIR photons attenuate VHE γ -ray emission from AGN over cosmological distances. If the source emits a spectrum of radiation $I_0(E)$ the spectrum observed

on Earth is:

$$I(E) = I_0(E)e^{-\tau} \quad (1.18)$$

where $\tau(E_0, z_e)$ is the optical depth of the infrared field as a function of the energy of the γ -ray and the redshift (distance) to the source, z_e . Roughly one can think of τ as:

$$\tau \sim n_{IR} D \sigma_{\gamma\gamma} \quad (1.19)$$

where n_{IR} is the infrared photon density, D is the source distance, and $\sigma_{\gamma\gamma}$ is the pair creation cross section. When one takes into account the density variation as a function of the distance, the expansion of the universe and the centre of mass energy dependent cross section the expression for the optical depth becomes [24]:

$$\begin{aligned} \tau(E_0, z_e) &= c \int_0^{z_e} dz \frac{dt}{dz} \int_0^2 dx \frac{x}{2} \\ &\times \int_0^\infty d\nu (1+z)^3 \left[\frac{u_\nu(z)}{h\nu} \right] \sigma_{\gamma\gamma}(s) \end{aligned} \quad (1.20)$$

where $s = 2E_0 h\nu(1 - \cos\theta) \cdot (1+z)$, ν is the IR photon frequency at redshift z , z_e is the redshift of the γ -ray source, $x = (1 - \cos\theta)$, h is Planck's constant, $u_\nu(z)$ is the radiation density as a function of redshift and $\sigma_{\gamma\gamma}$ is the pair creation cross section as a function of the centre of mass energy. The opacity of IR photons as a function of the energy of the high energy gamma for various values of the distance to the source (redshift) is shown in figure 1.19. Figure 1.20 displays the results of applying this model to well known blazars.

1.3.2 Active Galactic Nuclei

The first Active Galactic Nuclei (AGN) observed were quasars. They were first observed with the radio telescope at Jodrell Bank and were initially thought of as quasi stellar objects (hence the name quasar) that reside in our own galaxy. In

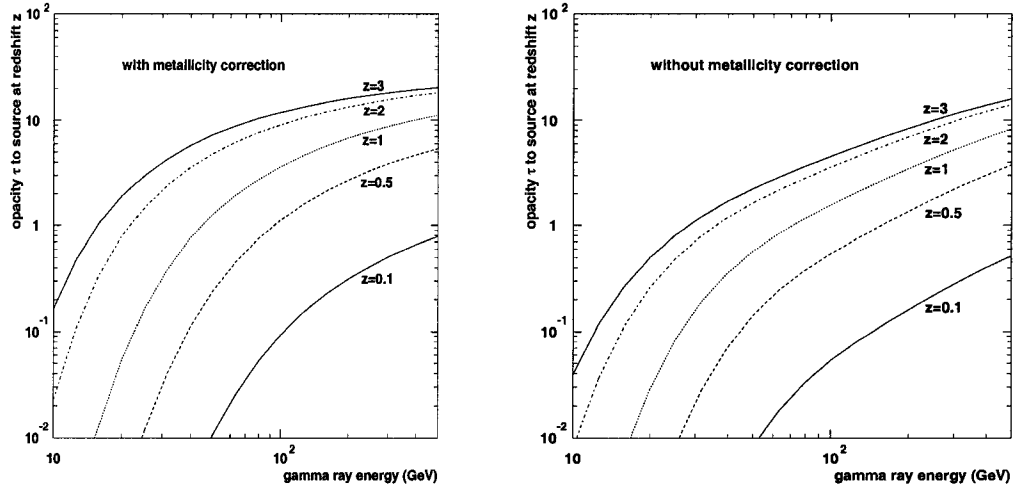


Figure 1.19: Opacity of the intergalactic IR field to γ -rays as a function of the γ -ray energy and source redshift [24]. The metallicity correction is made to compensate for the evolution of the stars that emitted the soft photons while they were forming. The calculation performed without the metallicity correction assumes the value for the sun's metallicity.

the 1960s, when the angular resolution of radio telescopes became good enough to allow astronomers to find the optical counterparts to these sources, the scientific community realised that these were actually extragalactic sources at relatively high redshifts.

Because of the large distances involved these objects were much too luminous to be stars and it was realized that they were most likely galaxies of a special type. Since then many new classes of AGN have been observed. An individual object is classified with respect to its observable characteristics, mostly in the radio and optical regimes of the electromagnetic spectrum, instead of the nature of the underlying object. However, it should be stressed that many classes share at least some characteristics.

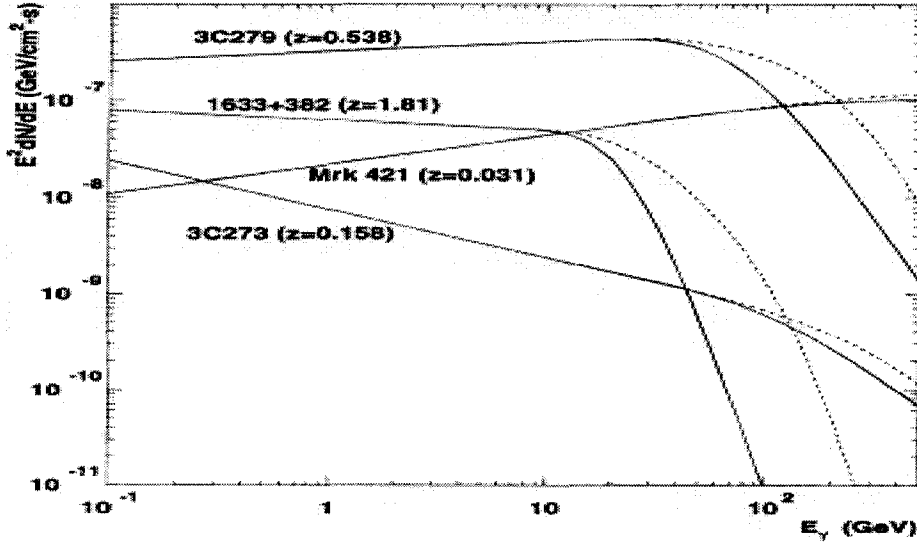


Figure 1.20: The effects of intergalactic absorption combined with the power law spectra of four prominent EGRET AGN. Note the spectral cutoffs arising from absorption alone. The solid curves are calculated with the metallicity correction function, the dashed curves are without [24].

1.3.2.1 Unified Model of AGN

Over the past 20 years a consensus has begun to emerge in the AGN community on some general characteristics that all AGN share. We will describe the basic components that are thought to be common to all AGN starting from the centre of the galaxy and working outwards. The elements to be described in the next few paragraphs are depicted in an schematic representation in figure 1.21.

Central Supermassive Black Hole At the centre of every AGN there exists a supermassive black hole, of mass $M \sim 10^7 - 10^{10} M_{\odot}$. Observational evidence for this hypothesis can be observed in gas dynamical tests. When these methods are applied to the radio galaxy M87 the mass within 18 pc of the galactic nucleus is estimated to be $2.4 \times 10^9 M_{\odot}$ [25]. Ultimately it

is the accretion onto this black hole that acts as the energy source for the AGN. The actual dimensions of the black hole are tiny with respect to the rest of the host galaxy: a $2 \times 10^{10} M_{\odot}$ black hole would have a Schwarzschild radius of about 0.001 pc.

Accretion Disk Immediately outside the black hole is a thin accretion disk. The in-falling material assumes a disk shape, instead of a spherical one, because it is the most time-stable geometry. The temperature of this disk ranges from 10^5 K at its inner radius to 10^4 K on its outer limit. The accretion disk extends out to distances on the order of 0.1 pc. The accretion disk emits thermal radiation, from the blue end of the visible light spectrum at its outer edge to soft X-rays at its inner radius. The accretion process can convert up to 10% of the rest mass of the accreted matter into radiation [26].

Dust Torus Outside the accretion disk is a thick torus lying in the equatorial plane of the black hole at a distance on the order of 1 parsec from the centre of the AGN. The torus itself is very wide and can extend up to a distance of several hundred pc from the centre. The torus is thought to be made of slow moving dust rotating around the black hole at ~ 1000 km/s, and can be observed in the infrared. The torus is also thought to shield other emissions from the AGN at observation angles close to the equatorial plane of the galaxy.

Relativistic Jets Radio loud galaxies and blazars have been observed to have well collimated jets perpendicular to the accretion disk. How these jets are formed and evolve is poorly understood. These jets extend far beyond the host galaxy, to distances on the order of Megaparsecs. As the jets interact with the intergalactic medium, shock waves form within the jet and can be sources of shock wave acceleration along the axis of the jet. These particles (it is not known whether they are leptonic or hadronic) then interact with

photons (possibly originating from synchrotron acceleration in the jet itself or from other parts of the AGN) via the IC mechanism to produce high energy γ -rays.

Clouds of matter At distances of ~ 1 kpc from the central black hole there are two distinct groups of clouds in and around AGN: those that are situated above the disk (possibly distributed almost spherically around the black hole and are responsible for broad-line emissions) and those that are situated in the plane of the disk at large radii (responsible for narrow-line emissions). The former are thought to be much closer to the central black hole and moving at a greater velocity than the latter. Both distributions are non-uniform.

With these basic constituents (shown in figure 1.21) a unified AGN model has emerged. Starting from the basic morphological model it is possible to understand most classes of AGN as consequences of viewing the AGN at different angles with respect to the jet axis.

The absence of various characteristics in some classes of AGN can be explained in this model by occultation by the large dust torus. Figure 1.22 demonstrates this idea with a cross sectional view of the unified AGN model. The lowest energy AGN are those that are viewed along the disk of the AGN (radio galaxies). As the angle between the line of sight and the central jet decreases, the emissions from the AGN increase in energy. The highest energy emissions from AGN occur when the observer is viewing the AGN down the axis of its central jet. All AGN observed in the TeV regime have been in this blazar class. In order to see TeV γ -rays the viewing angle must be within $\approx 10^\circ$ of the jet axis [27].

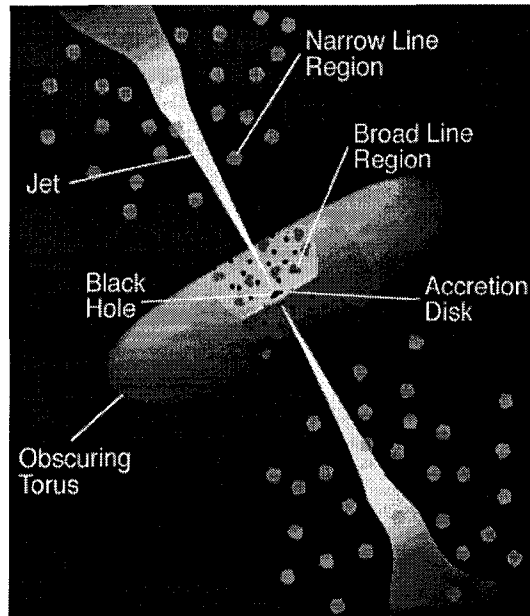


Figure 1.21: Highly conceptualised artist's impression of an AGN. The central torus is the dust torus which is responsible for absorption. The jets emerging from the centre of the galaxy on an axis perpendicular to the disk are composed of highly relativistic particles. The dark circles represent high velocity clouds responsible for the broad emission lines characteristic of most AGN. The lighter circles represent slower moving clouds of matter that are thought to be responsible for the narrow line emission of AGN.

1.3.2.2 VHE γ -ray emissions from AGN: Hadronic vs. tonic models

With only 3 AGN observed above EGRET energies there is very little data to prove or discredit the numerous models for AGN VHE γ -ray emissions. The one point that the various models share is that the initial charged particle acceleration takes place in the jets. The two main classes of models for particle acceleration in AGN are the hadronic and electronic beam models. The electronic model has two main variants: the SSC model and the external IC model where the photons

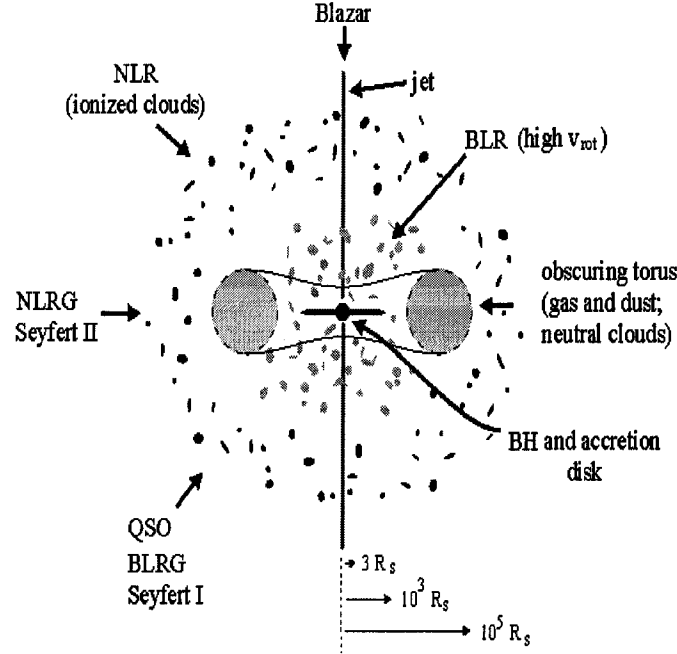


Figure 1.22: AGN schematic diagram with the AGN classification labelled with the viewing angle. BLRG and NLRG are broad line and narrow line region galaxies respectively. The galaxies are classified as quasars (QSO) at mid range angles and as blazars when one is within 10° of the central jet axis. The distance scale is indicated in terms of factors of the Schwarzschild radius, R_s and BH stands for black hole.

are generated outside the jet [28]. Both hadronic and electronic models tend to rely on shock acceleration of the charged particles (be they e^- or p) in the shock fronts that occur as the jets interact with the intergalactic medium surrounding the AGN. The two models differ mostly in their mechanism for energy transfer from charged particles to photons. The electronic models rely on the IC process while the hadronic models rely on neutral pion decay:

$$p + \gamma \rightarrow p + \pi^0 \rightarrow p + \gamma + \gamma \quad (1.21)$$

The hadronic jet model has an SSC variant called the Synchrotron-Proton-Induced Cascade (S-PIC) and a variant that is comparable to the external IC model called the E-PIC model. In both models γ -ray production must occur far away from the torus in order to avoid absorption of the γ -rays by the intense infrared radiation field emitted by the torus. Figure 1.23 illustrates the QED and QCD processes that take place in AGN for both the hadronic and electronic jet models. Although many more measurements will be needed to rule out or strongly

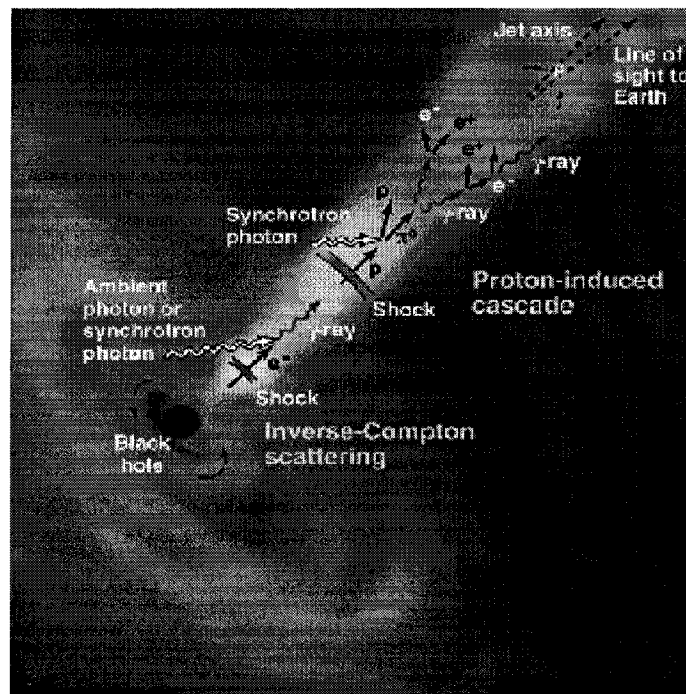


Figure 1.23: Cartoon of AGN γ -ray emission models. Both leptonic and hadronic beam models are shown with their respective energy transfer mechanisms. In both cases the initial charged particles are accelerated to high energies using shock wave acceleration. The electrons produce γ through the IC mechanism whereas the high energy protons rely on neutral pion decay. It is important to note that in order to avoid absorption by the hot clouds that surround the AGN the production of high energy γ -rays must occur at a sufficient distance down the jet axis.

support one of these models, the measurements taken to date pose some problems for both the hadronic and electronic models. Since electrons radiate more energy when they are in magnetic fields, they are more difficult to accelerate to high energies than protons. The maximum attainable energies of the charged particles depend on the magnetic field strengths within the jets, but for a comparable magnetic field strength, protons can achieve higher maximum energies than electrons. Measurements of AGN emissions up to 10-20 TeV then favour the hadronic beam model.

AGN have been observed to have γ -ray emission rates that vary on a time scale of hours. This rapid variability seems to favour the electronic beam models, where the electrons can lose their energy in much less time than the protons [29].

1.4 AGN ON+231

AGN ON+231 is part of the Coma Cluster of galaxies and is also known as W Coma. In EGRET studies this AGN is also known as AGN 1219+285. ON+231 has been observed since the early 1900s. The earliest observations of this object date to 1892 and the first data published by Maximilian Wolf date to 1916 [30]. However, the quality of this data has been questioned and it is often excluded from historical light curves. Figure 1.24 shows the historical light curve of ON+231 with the original Wolf points removed. In 1971 ON+231 was one of the first objects to be classified as a BL Lac object (BL Lac objects are characterised by their rapid time variability and their strongly polarised power law continua which are nearly devoid of emission lines). [32, 33]. ON+231 has been observed in the radio, optical, X-ray and γ -ray bands. These observations have yielded many interesting characteristics of this AGN. These include, the “extraordinary optical outburst” in 1998, a 3.8 year period for optical outbursts, a distorted jet structure and the

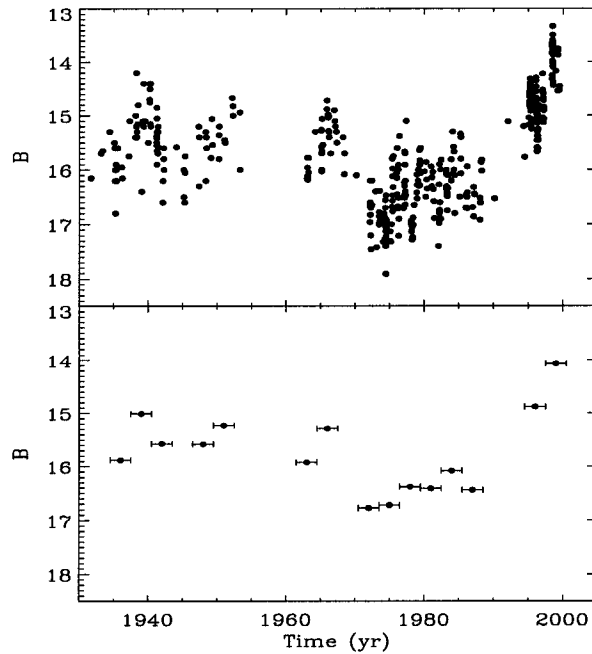


Figure 1.24: The historical light curve of ON+231 from 1930 to 1992. Magnitude in the B band is plotted versus years. In the lower plot the same data is presented averaged over intervals of 3 years.[31]

flattest (hardest) γ -ray spectrum of all EGRET blazars.

1.4.1 Optical Observations

Very few BL Lacs have been observed for as long as ON+231. The historical light curve (shown in Figure 1.24) dates back to the early 1900s, when it was in a very bright state, and shows how variable this source has been over the years. It seemed to reach a quiet period between 1960 and 1975, a period when ON+231 reached its lowest brightness of 17.4 in B magnitude. The flux then started increasing in the mid 1970s but always showed fluctuations with a typical

amplitude of 1.0-1.5 mag. In the 1990s ON+231 entered a new active state that culminated in the “extraordinary optical outburst of 1998” [34]. The recent light curve of ON+231 including the 1998 outburst is illustrated in Figure 1.25. During

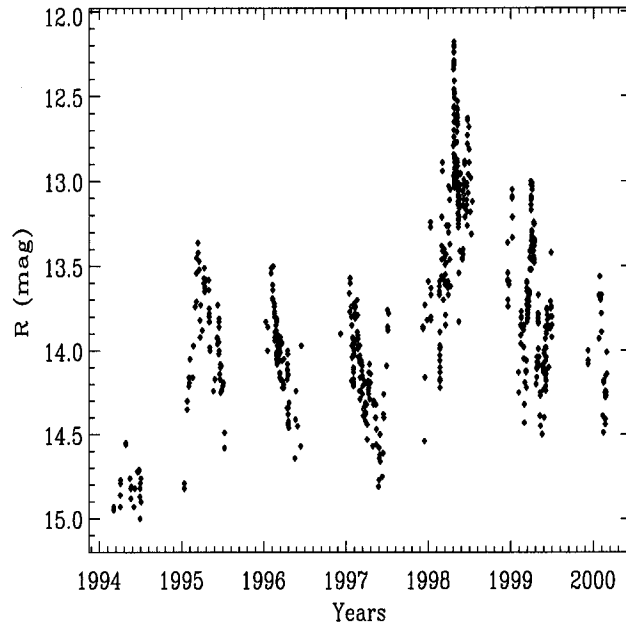


Figure 1.25: The recent light curve including the extraordinary optical outburst of the spring of 1998 [35].

this burst ON+231 was 3 times brighter than in the previous years and a factor of 60 brighter than the minimum flux measured in the early 1970s. Outburst frequency analysis of the B band data collected between 1971 and 1998 reveal that the outbursts have a possible periodic structure with $P=3.8$ yrs [36]. The exact causes of periodic optical emissions aren’t well known. Thin accretion disk theory proposes several processes responsible for this effect ranging from binary black holes [37] to radial acoustic oscillations [38] amongst others [39]. The large outburst measured in 1998 can be considered as an ordinary structural peak of the periodical outbursts that has nearly the same amplitude (in mag.) as ones which

occurred in previous cycles. The amplitudes of the previous outbursts were nearly constant at ≈ 2 mag. The 1998 outburst followed an underlying slow increase in brightness that started about 2 decades earlier. The frequency analysis of the B band data is presented in figure 1.26.

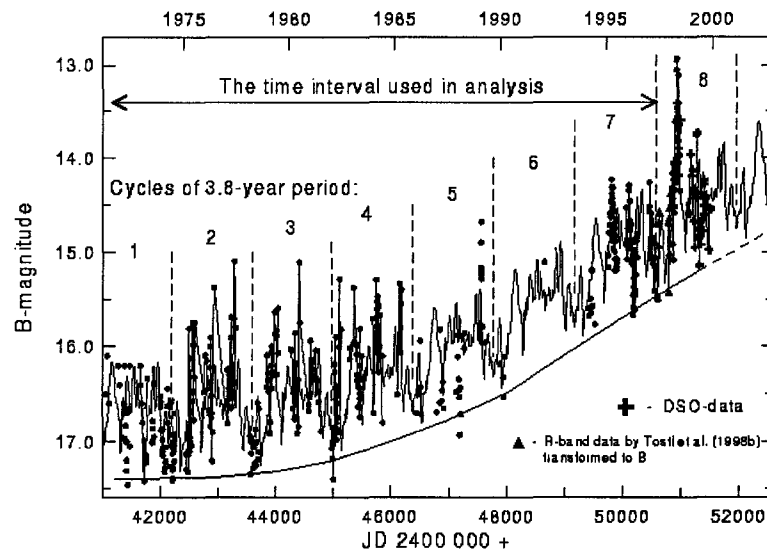


Figure 1.26: Outburst frequency analysis of the B band data from the recent light curve. The 1395 day (3.8 year) periods are marked by dotted lines. The straight line shows the underlying slow increase in brightness. The x-axis is in Julian days +2400 000. Julian day 0 was on January 1st 4713 BC and Julian day 2435 000 was on September 14, 1954.[36]

1.4.2 Radio Observations

After BL Lac and 3C273, ON+231 was one of the first quasars to be recognised as an extragalactic source. This was a result of a 2695 MHz radio survey of a narrow strip in declination performed with the Jodrell Bank Mark II instrument in 1971 [33, 32]. It was remarked at the time that ON+231 had a possible jet-like

structure associated with it, extending to 12 arc seconds from the main source. Later images of ON+231 taken in 1982 [40] and again at 5 GHz in 1985 [41] suggest the presence of a possibly curved jet extending from the central component to an eastern “hot spot”. The leading explanations for the curving of the jet are a wobble of the jet itself or an interaction of the jet with an external medium. In addition to a curving of the jet (or perhaps because of it) the jet is not aligned with the rotation axis of the galaxy.

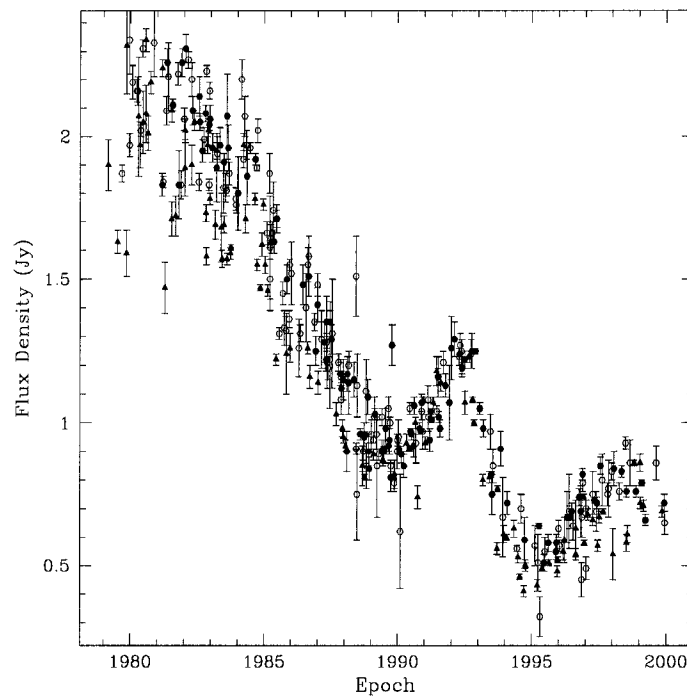


Figure 1.27: The radio light curve for ON+231. The filled circles are 4.8 GHz data, the open circles are data taken at 8 GHz and the triangles were taken at 14.5 GHz. The graph shows a steady decrease in radio output with two distinct peaks in the 1990s [35].

Because of these peculiar characteristics, ON+231 has been the subject of radio monitoring since the 1980s. Unlike the visible light curve, the radio light

curve shows a steady decrease in flux with two distinct periods of brightening. Although the latest peak in radio emissions coincides with the optical outburst of 1998, there is little evidence that these two events are related. Figure 1.27 shows the radio light curve.

Because of Doppler shift considerations, we can usually only see one side of the jets present in AGN. The details of apparent superluminal motion in AGN jets are beyond the scope of this thesis (an explanation of this effect can be found in [42]). However, the result of this effect is that the intensity of the jet that is moving towards the observer is Lorentz boosted up while the jet that is moving away from the observer is Lorentz de-boosted with the result that one jet becomes too faint to be detected. With a modest Lorentz factor $\gamma = 2.3$ and loose constraints on the angle between the jet and the line of sight, $\psi \leq 20^\circ$, the intensity ratio between the jet moving towards the observer and the jet moving away from the observer is $> 10^3$ [27].

The latest radio observations of ON+231 (performed after the 1988 optical outburst) with the Multi-Element Radio Linked Interferometer Network (MERLIN), seem to indicate that ON+231 has two visible radio jets. The unprecedented sensitivity and resolution of the MERLIN very long baseline interferometer was needed to detect the weak counter-jet. Figure 1.28 is taken from a recent publication where evidence for a counter-jet in ON+231 is presented. The newly detected jet of ON+231 is the area labelled **a** to the right of the core on Figure 1.28. On the basis of radio and optical data alone ON+231 is emerging as a unique AGN that seems to defy adherence to any but the smallest and most specific classification of galaxies.

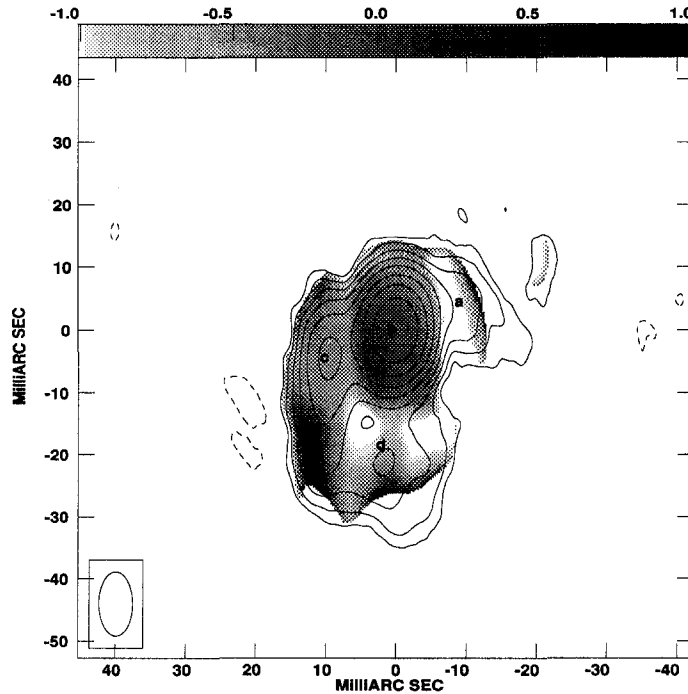


Figure 1.28: Spectral index (grey scale) map computed from MERLIN superimposed on the image at 1.67 and 5 GHz. a) is the newly observed jet structure, b) represents the core of the galaxy and c) is the previously observed jet. The small peak at d) is tentatively explained as the bending of the jet due to interaction with the near environment [35].

1.4.3 X-ray Observations

In the weeks following the 1998 optical outburst, ON+231 was the object of intense simultaneous observations using X-ray and optical telescopes. The BeppoSax satellite observed it in May and June following the optical outburst in 1998, measuring the X-ray spectrum between 0.1 and 100.0 keV. During these observations a high variability event, where the X-ray flux below 4 keV changed by a factor of three in 5 hours, was also observed. The resulting spectrum did not fit the usual power law distribution; instead two distinct peaks were noted. It

is believed that these two humps are the synchrotron and Inverse Compton (IC) components of the AGN's spectrum. ON+231 is the only AGN to have its synchrotron and IC peaks resolved with the same instrument. Figure 1.29 shows the Spectral Energy Distribution (SED) of ON+231 synthesised from the observations of the AGN ranging from radio frequencies to TeV energies.

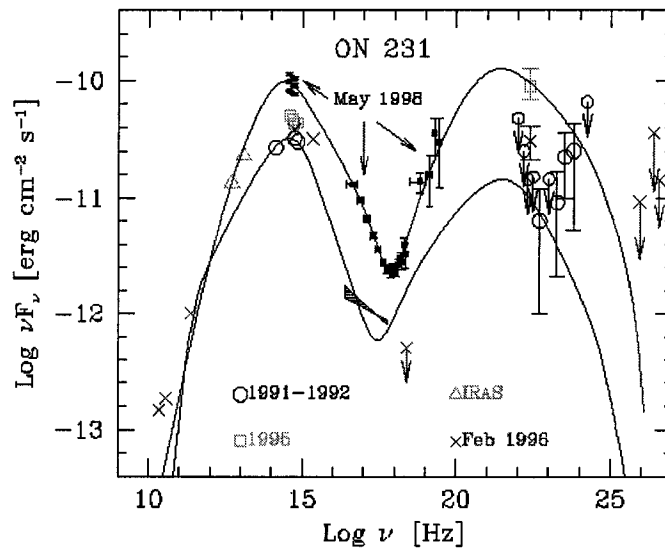


Figure 1.29: The Spectral Energy Distribution of ON+231. The lines are SSC models with different input parameters. 1991-1992 points (empty circles) are composed of infrared, optical, X-ray and γ -ray (EGRET observations). The 1995 points (empty squares) are composed solely of optical data and γ -ray data. The solid squares are optical and X-ray data gathered in the May and June 1998 observations [43].

Because ON+231 had its synchrotron and IC peaks resolved by the same

instrument it became an ideal source for comparison to established SSC models. ON+231 has been used as the defining example of an Intermediate BL Lac Object [43].

1.4.4 γ -ray Observations

ON+231 was observed by EGRET in all of the instrument's campaigns. The observations gathered by EGRET on this source over CGRO's lifetime are summarised in Figure 1.30. Like all EGRET sources the energy spectrum was fit to a 3 parameter power law:

$$dN/dE = N_0(E/E_0)^{-\Gamma} \frac{\gamma's}{secMeVcm^2} \quad (1.22)$$

Where the fitted parameters are the spectral index Γ , the overall scaling factor, N_0 , and the energy scale factor E_0 (of these parameters only Γ and E_0 are independent). Early measurements of ON+231 placed its spectral index at $\Gamma = 1.39 \pm 0.44$ [44]. Later emissions in the EGRET energy range resulted in a softer spectrum, listed in the third EGRET catalog.

$$dN/dE = (2.1 \pm 0.37) \times 10^{-11} (E/721)^{-1.73 \pm .18} \frac{\gamma's}{secMeVcm^2} \quad (1.23)$$

Despite this newer, softer spectrum, ON+231 still possesses the hardest spectrum of all EGRET-detected blazars. This fact has two interesting consequences: namely that these data points do not seem to agree with the X-ray data and that with such a hard spectrum and relatively short distance from us ($z = 0.102$) one would expect to detect this blazar at Whipple energies.

X-ray data taken on this blazar following the 1998 optical outburst seemed to agree with SSC models and made this the signature blazar for the intermediate energy blazar class. The 1991-92 EGRET points in figure 1.29, indicate a trend that opposes the predictions of the SSC model. This disagreement with the SSC

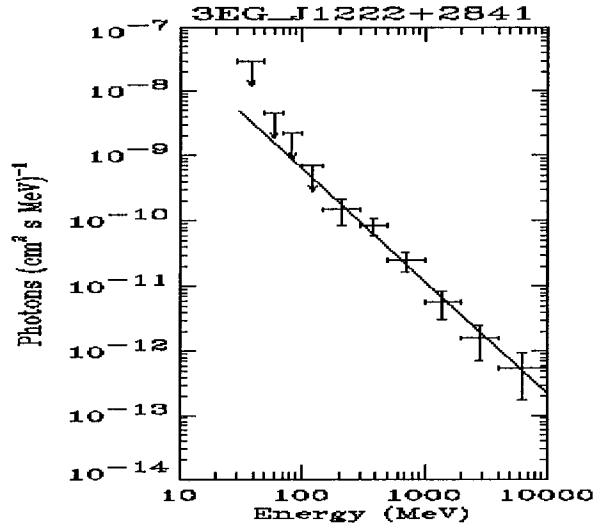


Figure 1.30: The EGRET spectrum of ON+231 from the 3rd EGRET catalog [5].

model has led the authors of [43] to conclude that the hard 1991-92 γ -ray spectrum is due to another source within the EGRET error box, or, that if the γ -ray data is indeed confirmed to be associated with ON+231, the hard γ -ray spectrum is produced by another component not directly associated with the AGN jet [43].

Prior to the 1998 optical outburst, ON+231 was the object of a multi-wavelength campaign [45]. Emissions at energies $E > 1$ TeV were not observed by either the HEGRA [46] or Whipple telescopes. A later study conducted with the Whipple telescope [47] at a lower energy threshold of 350 GeV, still revealed no observation of this AGN. The upper limit placed on emissions by the Whipple collaboration is well below the extrapolated EGRET spectrum. The simplest explanation for the non-detections at higher energies (namely that the TeV γ -rays suffer pair production attenuation off the diffuse intergalactic background) is problematic in the case of ON+231 because of its low redshift (distance). The Whipple collaboration and the authors of the multi-wavelength campaign conclude that the cutoff must be intrinsic and could possibly be due to absorption of VHE γ -rays by a “warm

dusty torus” surrounding the central part of the galaxy.

The relatively small distance to this AGN combined with its non-detection at energies above 350 GeV, along with its unique properties in the radio, optical and X-ray regimes, make it an attractive candidate object to search for in the unopened window that will be covered by such experiments as STACEE and CELESTE [48]. The following chapters will detail the brief search conducted for this AGN with the STACEE-32 prototype telescope in 1999.

Chapter 2

The STACEE-32 Detector

To observe in the unopened window from 10 to 250 GeV, one has to either increase the energy range of satellite experiments or lower the threshold of ground-based γ -ray telescopes. As mentioned earlier, above 10 GeV the flux of γ -rays is so low that satellite experiments, with their relatively small effective area, would not be able to detect a statistically relevant number of γ rays. Thus, to observe in this energy range, a new generation of ground-based Čerenkov telescopes must be constructed. The STACEE-32 telescope was one of the first steps in constructing such an instrument. The following chapter will consist of a brief general discussion on ACT energy thresholds and a detailed description of the STACEE-32 telescope.

2.1 ACT Energy Threshold

The energy response of an atmospheric Čerenkov telescope is in general a complicated issue that often requires simulation to explain. However, some general aspects of the energy response of ACT can be addressed quite simply. We start

by defining a scaling factor for the Čerenkov photon yield, y_γ :

$$y_\gamma \equiv \rho_\gamma/E \quad (2.1)$$

where ρ_γ is the density of Čerenkov photons on the ground and E is the energy of the primary γ -ray.

The signal one would expect from a Čerenkov telescope of area A and collection efficiency ϵ given a photon density ρ_γ would be:

$$S = \rho_\gamma A \epsilon = y_\gamma E A \epsilon \quad (2.2)$$

Every telescope, no matter how ideally situated will be subject to night sky background consisting of random photons from sources other than atmospheric Čerenkov light. These sources can vary from telescope to telescope, but are generally such things as sky glow from nearby cities, building lights, starlight etc. The noise one can expect from a Čerenkov telescope arises from fluctuations of the night sky background. It is these fluctuations in the night sky background (NSB), more than simply the amount of NSB, which is the most limiting factor to an ACT's response. The number of NSB photons accepted by the telescope will be $B\Omega A\epsilon\tau$ where B is the night sky background photon flux, Ω is the solid angle of the field of view, and τ is the electronic trigger formation time. Since the arrival of the NSB photons is random in nature, the statistical variation on this number is the background noise, which will be equal to its square root. Therefore, the noise can be expressed as:

$$N = \sqrt{B\Omega A\epsilon\tau} \quad (2.3)$$

Using these two equations one can express the signal to noise ratio as:

$$S/N = y_\gamma E \sqrt{\frac{A\epsilon}{B\Omega\tau}} \quad (2.4)$$

If we define the minimum energy, E_{min} , as the minimum γ -ray energy for which a shower will generate enough Čerenkov light to have signal-to-noise sufficient to adequately trigger the detector we may express E_{min} as:

$$E_{min} \propto \frac{1}{y_\gamma} \sqrt{\frac{B\Omega\tau}{A\epsilon}} \quad (2.5)$$

2.1.1 Reducing the Energy Threshold

Reducing the energy threshold of ACT's has emerged as the only way to observe in the unexplored energy gap between 10 and 250 GeV. Using equation 2.5, it is evident that one must try to reduce the night sky background flux as much as possible and similarly increase the detection efficiency of the detector as much as possible: these are goals of all types of experiments. The ACT characteristics that can be modified to allow them to conduct γ -ray astronomy in the unexplored energy band are the collection area, the integration time and the opening angle. Unfortunately the latter two parameters have limitations set by the physical properties of extensive air showers.

1. The duration of the Čerenkov pulse itself is about ~ 5 nsec. This is due to the actual thickness of the Čerenkov wavefront (between 1 and 2 metres) which arises from the fact that not all secondaries are created at the same time or at the same depth in the atmosphere. Trigger formation times less than the width of the Čerenkov shower width would result in cutting into the signal and thus degrade the signal to noise ratio. This means that the τ parameter in equation 2.5 can not be minimised further to reduce the energy threshold.
2. When showers evolve in the atmosphere they have a measurable angular width. The width of the shower at shower maximum sets the minimum value

for the field of view; a smaller field of view would diminish the Čerenkov signal. The angular size of the Čerenkov shower is about 0.5° as viewed from the ground. Thus, the variable Ω in equation 2.5 has a limit beyond which one would lose signal.

Because existing detectors have already approached the limits of the field of view and the trigger formation time, the most direct method to lower the energy threshold is to increase the collection area, A , of an ACT.

2.2 STACEE Concept

Present ACTs have maximum collection areas of $\approx 75 \text{ m}^2$. To achieve the mirror area needed to lower the threshold to cover the unobserved energy band, one must either use several imaging telescopes, which is what is planned for the VERITAS [49] and HESS [50] experiments or employ a large primary mirror like the MAGIC experiment [51]. A complimentary method is to use the large mirror area of solar power plants. The idea of using solar power plants to conduct γ -ray astrophysics is not a new one. In the early 1990s two experiments Themistocle [52] and then ASGAT [53] detected unpulsed signals from the Crab at energy thresholds of 2.0 and 0.6 TeV respectively. The new generation of solar power plant experiments will have much lower thresholds. The STACEE experiment is one of four such experiments (the others being CELESTE [48] Solar 2 [54] and GRAAL [55]). The STACEE detector, when completed, will have a collection area of $\approx 2400 \text{ m}^2$. Hence, the potential of solar power plants to conduct lower energy threshold measurements of γ -ray sources is tremendous.

STACEE uses the large solar mirrors (called heliostats) at the National Solar Thermal Test Facility (NSTTF) in New Mexico to collect Čerenkov light which

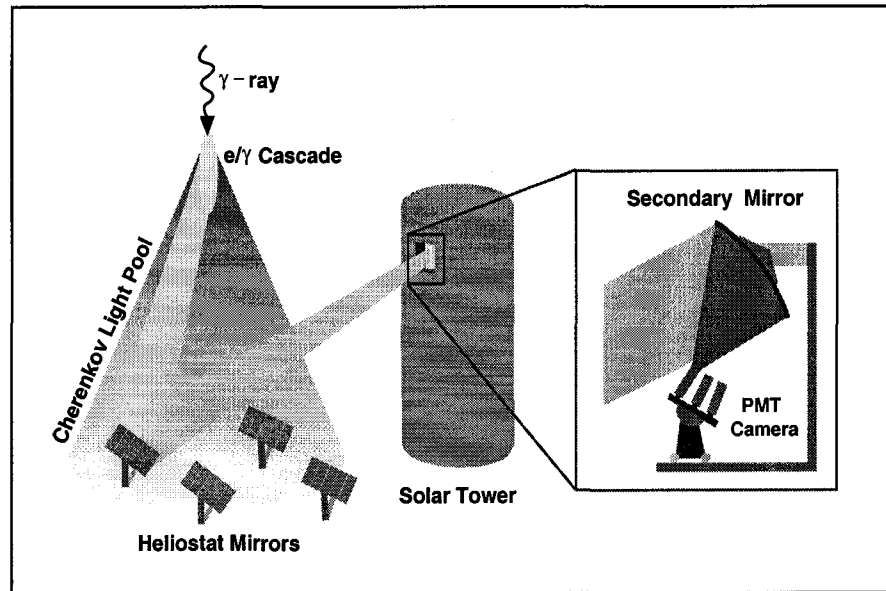


Figure 2.1: The STACEE telescope concept. Instead of using several imaging telescopes STACEE uses a solar power plant to increase the mirror collection area.

is then focused on a secondary optical system. The light is detected by cameras composed of photomultiplier tubes (PMT) with one PMT for each heliostat used. The signal from the PMT contains amplitude and timing information that can be used to discriminate against cosmic rays at the trigger level, and to reconstruct the Čerenkov wavefronts offline. Figure 2.1 illustrates these broad concepts.

2.2.1 NSTTF

The NSTTF is located at Sandia National Laboratories near the city of Albuquerque, New Mexico. Figure 2.2 shows an aerial photograph of the entire NSTTF site. Only a brief description of certain key elements of the facility relevant to STACEE's purposes shall be mentioned.

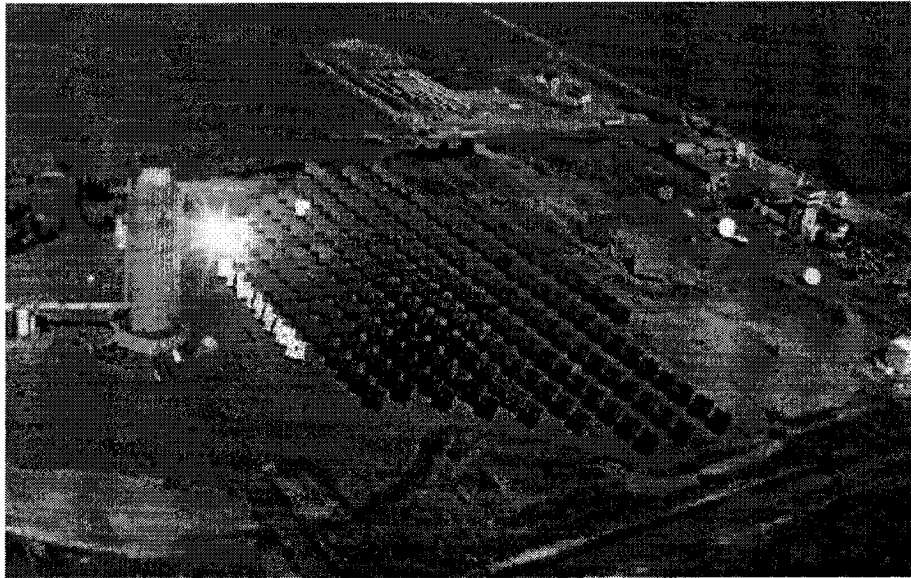


Figure 2.2: Aerial view of the National Solar Thermal Test Facility. The solar tower is to the south of the field. The heliostat control tower is to the north. The city of Albuquerque (a major source of ambient light) is also to the north.

The mirrors used to collect the sunlight are called heliostats. The NSTTF has 220 functioning heliostats. The entire collection of heliostats is called the heliostat field, or simply the field. South of the heliostats is the tower. The tower's main purpose is to house and maintain the sunlight receiver. The tower is a 200 foot tall structure (which also goes 100 feet into the ground). The bulk of STACEE's electronic equipment and data acquisition system is housed in a climate controlled room on the 200' level (200' signifies 200 feet from the bottom of the tower so 100 feet above the ground). The secondary optical system and front end electronics are situated at the 260' level bay. These locations on the tower are depicted in Figure 2.3. The heliostats are controlled from a different building called the control tower. The control tower is to the north of the field and contains the heliostat control room and the offices of the NSTTF personnel.

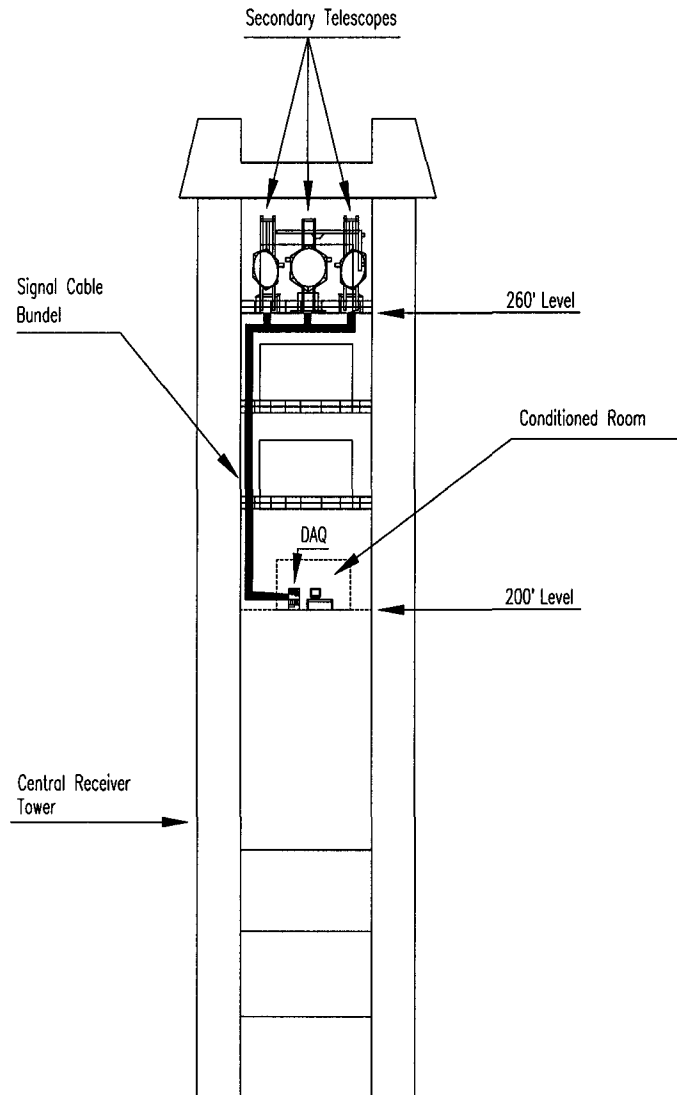


Figure 2.3: NSTTF solar tower with secondary optical system. For STACEE-32, only the outer two secondary mirrors are used.

The weather in Albuquerque is ideal for generating solar power. Many of these same conditions also make it an ideal site for an ACT [56]. Specifically the attractive aspects of the NSTTF for our experiment are:

Elevation Sandia is at an elevation of 1.7 km above sea level. This makes the detector physically closer to the showers and reduces loss in the atmosphere.

Dryness This area of New Mexico is exceptionally dry. This also improves the transmission of Čerenkov light in the atmosphere.

Clear Weather This area of New Mexico has exceptionally clear weather. This area provides the experiment with an average of 4.1 hours of cloudless, moonless observing time per night during the observing period from September through May [56].

Support The NSTTF is supported by the Department of Energy and is maintained by highly specialised personnel.

Large Mirror Area There are $\approx 220\ 37m^2$ mirror that are maintained and can potentially be used.

2.2.2 Heliostats

Heliostats are large composite mirrors used by the NSTTF to collect and focus sunlight onto a target. Each heliostat is a square array of 25 square facets mounted on a rigid framework (see figure 2.4). Each facet is four feet (≈ 120 cm) wide. The back of each heliostat facet is constructed with a steel ring connected to brackets that hold four set screws attached to the mirror itself. Three set screws are located along the ring and the fourth is at the centre of the facet. The mirror's shape can be made parabolic by adjusting the central set screw, while the facet's pointing

direction can be finely tuned by adjusting the three other screws along the ring on the back of the facet.

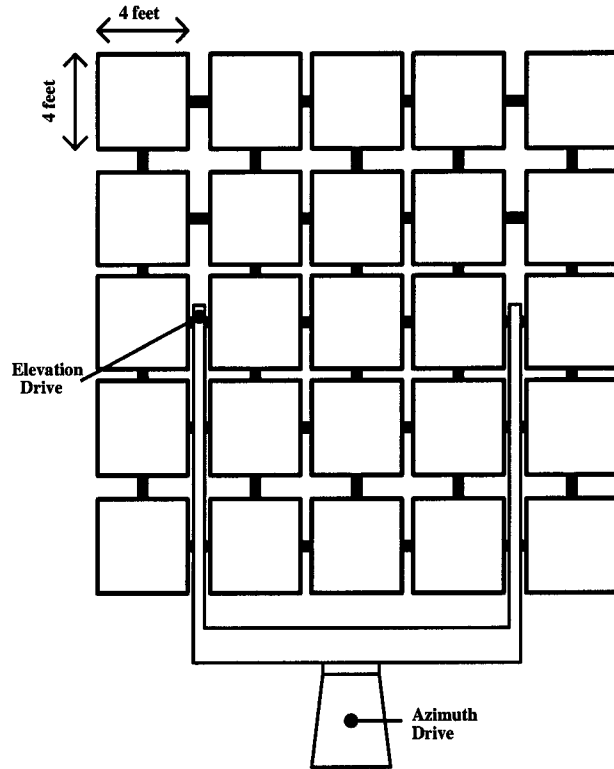


Figure 2.4: Schematic of an NSTTF heliostat. Both azimuth and elevation drives are shown.

The facets are back aluminized glass panels that are about 0.5 cm thick. Being back reflecting entails a light loss in the glass itself. The heliostat reflectivity was measured by members of the STACEE collaboration. The measured reflectivity as a function of wavelength is presented later in figure 2.11. The reflectivity curve reaches a maximum at $\approx 90\%$ and decreases rapidly below 400 nm.

The Moon and the Sun can be used as calibration sources since they are both about the same size as the maximum width of an extensive air shower $\approx 0.5^\circ$. A heliostat that is perfectly aligned when imaging the sun should project 25

superimposed facet images that result in a spot that is roughly 2 metres wide.

The heliostats can be moved in azimuth and elevation using two drive motors. Both drive motors are controlled by 13-bit encoders which allow each heliostat to be positioned to a precision of 0.044° . Each drive has two slewing speeds: coarse and fine. The coarse control is used to cover large variations in as little time as possible, while the fine control is used to make final adjustments. When a source is being tracked the fine control is used. But, even with the fine tracking speed and the good pointing accuracy, the system is not an analogue one. When a heliostat tracks a source, the encoders are updated one bit at a time. The effect of the digital nature of the control system can be seen clearly in figure 2.5.

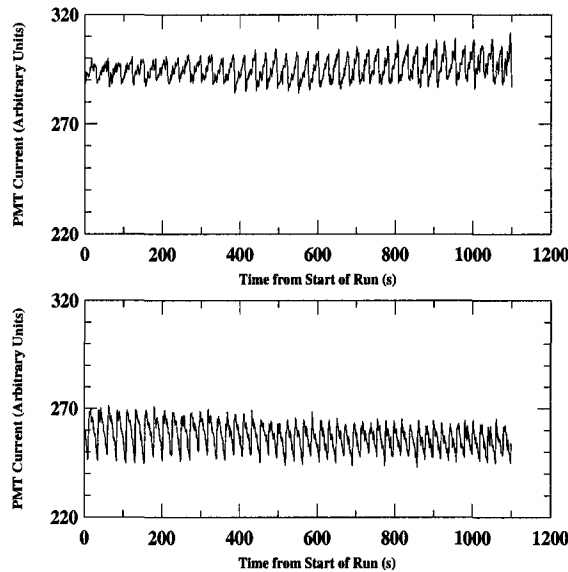


Figure 2.5: Phototube currents, obtained by tracking a star, are plotted as a function of time. The sawtooth pattern is due to the digital nature (tracking in increments of 1 bit (or 0.044°) steps) of the tracking system.

The software used to control the heliostats resides in one computer and is called the Master Control System (MCS). It is from this computer that scripts

are run to allow for the tracking of various sources, the proper deployment and stowing of the heliostats and for performing calibration runs. The overall pointing of each heliostat is calibrated using the MCS. This calibration is called “biasing”. This is usually performed by tracking the Moon and changing the offsets to the azimuthal and elevation drives (the “bias bits”) to obtain a maximum brightness of the image. When a heliostat is improperly biased one will not see the image in the focal plane of the camera move off target: the image stays in the same position but fades in intensity. Because the image projected onto the secondary mirror moves with biasing, fewer and fewer photons hit the secondary [57]. Every time an azimuthal or elevation drive is changed the heliostat must be re-biased. An error in biasing of only a few bits can result in a significant loss of light from a heliostat. The STACEE heliostats were all biased with the Moon in November of 1998, just before the start of the first Crab observations.

2.2.3 The Secondary Optical System

The purpose of the secondary optical system is to collect light coming from the heliostats and focus it onto the camera. For every 16 heliostats used in the STACEE experiment there is one secondary mirror. The secondary mirrors are composed of 7 hexagonal spherical sections, each with a 2 m focal length, that are held in place to form a spherical mirror that is 1.9 m wide. The secondary mirrors are supported by structures known as “spiders”. The spiders are specially designed to provide a rigid adjustable framework that keeps the mirrors in a spherical configuration. Figure 2.6 shows the seven facets mounted on the spider.

The central facet is fixed, but the spider allows the 6 other facets to be adjusted so that they can be co-aligned with the central facet. The outer six facets were aligned by placing a point source of light, surrounded by a small white screen, at

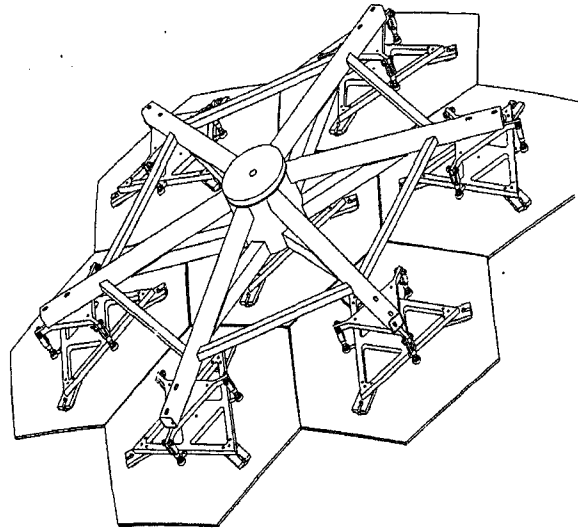


Figure 2.6: Back view of the spider with the seven secondaries mounted.

the centre of curvature of the mirror and adjusting the spider until the reflected images from all seven facets overlapped.

The spider is in turn mounted on a stacker (an industrial hydraulic lift) used to position the secondary in the z direction (height), to an accuracy of 1 mm. The entire secondary optical system is depicted in figure 2.7.

The secondary mirror facets are front silvered in order to minimise the amount of light that would be lost in traversing the glass twice. The reflectivity as a function of wavelength is plotted in figure 2.11. The secondary mirrors' front silvering gives them much better response to low wavelengths. The light from the heliostat field comes in on average, 12.8° off axis above the camera, the light is then reflected and focused, again off axis onto the PMTs.

The nature of the off axis optics results in some spherical aberrations and coma tails, which can sometimes stretch the image into other channels. Figure

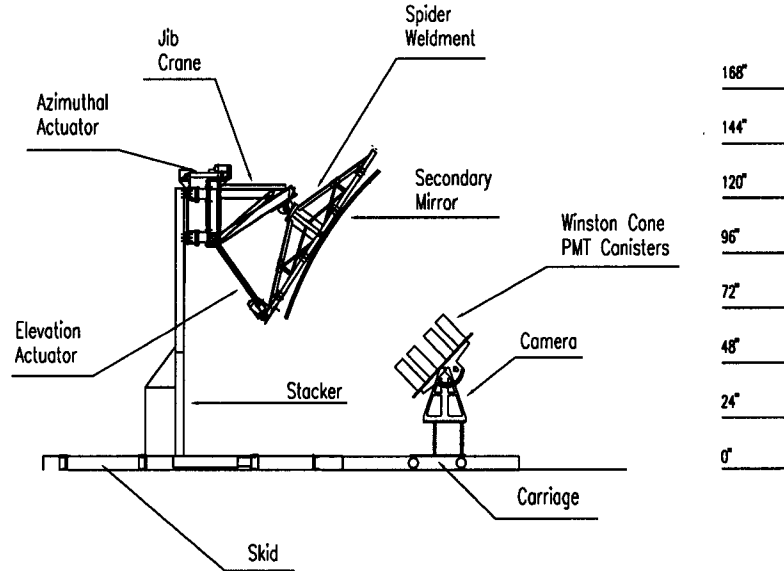


Figure 2.7: The secondary mirror and its support structure, the spider and stacker, deployed in the standard running position.

2.8 is the result of a simple simulation of off axis aberrations with a spherical mirror. The object being reflected was a $10\text{m} \times 10\text{m}$ metre square, essentially a heliostat, 50 m off axis horizontally and vertically from the principal axis of the secondary and 150 m away from the secondary. The stretching of one heliostat image into another heliostat's channel results in crosstalk between the channels. This crosstalk can be easily detected and cut out of the analysis offline, due to the differences in the times of flight between the two heliostats. The shortest difference in time of flight between two STACEE-32 heliostats is 50 nsec, since we only accept a narrow band of ± 6 nsec around the principal signal (see section 4.2.4) crosstalk does not affect our data.

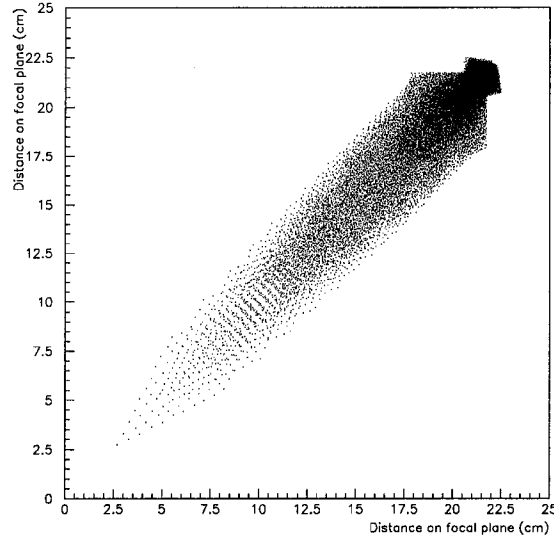


Figure 2.8: Result of a simple simulation of a spherical secondary mirror. The object (a $10\text{m} \times 10\text{m}$ square facing the secondary) was placed 50 m off axis horizontally and vertically, and 150 m away from the mirror.

2.2.4 The PMT Cameras

The camera used by STACEE resembles detectors used in particle physics experiments more than it resembles any type of traditional optical camera. The STACEE cameras perform the same role as PMTs in calorimeters: they detect quick flashes of Čerenkov light that are the result of showers (be they electromagnetic or hadronic). The PMTs must be as fast as possible since a response time on the order of nanoseconds is essential for observing Čerenkov light from atmospheric showers. We have seen in equation 2.5 that the “exposure” time of the STACEE camera must be as close to its theoretical limit (of the order of a few nanoseconds) as possible in order to improve our signal over background.

The camera is mounted on a wheeled cart that is moved out over the edge of

the tower to observe and then moved back onto the bay for storage and repairs. Both the camera and the secondary mirror are mounted on a heavy steel I-beam structure called the skid. The skid is in turn permanently welded onto the steel girders of the tower. The purpose of the skid is to anchor the secondary and camera, and to provide a track on which the camera can be deployed and stored (see figure 2.7). The PMTs are held inside canisters with light concentrators and optical couplers. These canisters are held in place and positioned on the camera by mounts that allow adjustment in azimuthal and elevation angle relative to the camera plane. Figure 2.9 is a cross section of such a canister assembly. The canisters are positioned so that they point to the centre of their secondary mirror. The backplane is held on a camera support structure that keeps the backplane at a fixed angle of 44.8° from the vertical. This angle was chosen so that the heliostat images could be projected 12.8° below the secondary's principal axis.

2.2.4.1 Light Concentrators.

The STACEE light concentrators serve two functions. First, they concentrate light from an 11 cm diameter (roughly the size of the heliostat image in the focal plane of the secondary optical system) to the 5 cm diameter photocathode, effectively expanding the acceptance area of the phototube by a factor of 4. The second purpose of the light concentrators is to limit (and somewhat equalise) the field of view of the phototubes so that only light from a selected portion of the secondary can be seen by the PMTs. The light concentrators are called DTIRCs (Dielectric Total Internal Reflection Concentrators) [58]. They are a variation of the more familiar Winston cones used extensively in particle physics. DTIRCs were chosen over solid Winston cones because they could be made smaller and less massive which makes them both mechanically easier to handle and less expensive to fabricate.

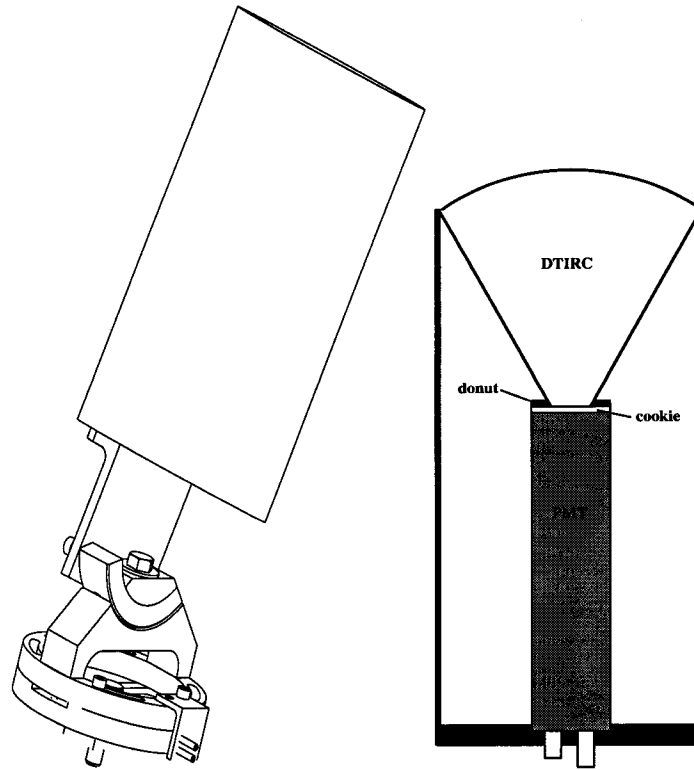


Figure 2.9: Left: The canister support structure used to fasten and orient the PMT cans. Right: Schematic of all of the elements used in the canisters: the photomultiplier (PMT), the optical coupler (cookie) and light concentrator (DTIRC). The donut was added to the assembly to prevent any stray light entering the PMT.

The STACEE DTIRCs are made of solid acrylic given to the collaboration by the Sudbury Neutrino Observatory (SNO) experiment. This particular type of acrylic is transparent to blue and UV light (good transmission down to $\lambda \approx 320$ nm). The transmission curve for this acrylic is plotted in figure 2.11.

A STACEE DTIRC has a spherical front surface on a truncated cone. DTIRCs don't necessarily need to take this form; this form was chosen for compactness and for ease of fabrication. Three types of DTIRCs are used in the STACEE cameras, each with the same front face but differing cone angles and therefore different

acceptance angles. These were used to roughly equalise the fields of view of the channels. Figure 2.10 demonstrates with a ray trace how photons arriving at the curved surface of the DTIRC can be accepted or rejected.

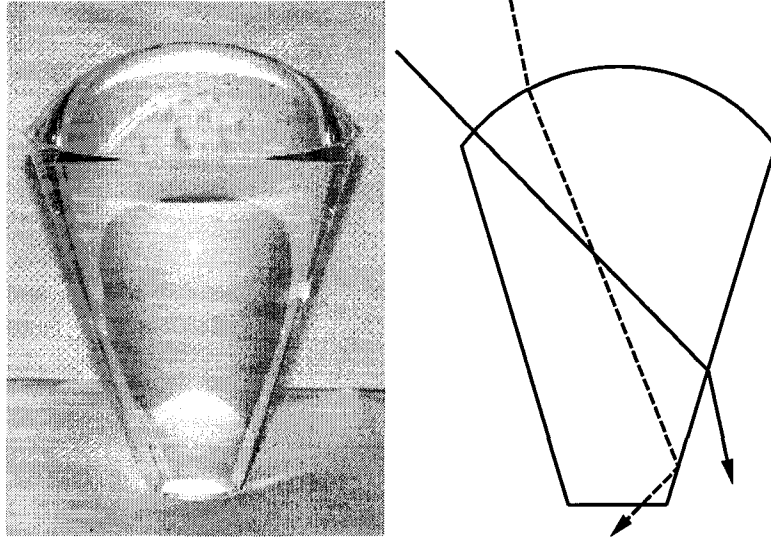


Figure 2.10: Left: a photo of a STACEE DTIRC. The DTIRCs were initially cut from 1 m^2 acrylic slabs, and then machined and polished to optical quality in the McGill machine shop. Right: a ray trace is used to illustrate the DTIRC's field of view limit. The dashed line strikes the DTIRC within its acceptance angle and is accepted, the solid line is rejected.

The field of view for a heliostat is the ratio of the effective diameter of the secondary mirror to the distance between the heliostat and the secondary. DTIRCs with narrower angular acceptances were used for the channels with nearby heliostats (thereby limiting how much of the secondary those channels can see). The DTIRC with a larger angular acceptance were used to view the more distant heliostats.

This rule was generally followed with the exception of channels that experienced significant smearing due to the off axis nature of the optics. Although this configuration would seem counter-intuitive (since distant heliostats should appear smaller and thus necessitate DTIRCS with smaller acceptance angles), the large coma tails spread the image out over a greater area on the focal plane, and necessitated the use of larger acceptance angle DTIRCs for the most distant off axis heliostats. Table 2.1 summarises the properties of the three DTIRC types.

Angular Acceptance (Degrees)	Entrance Diameter (cm)	Exit Diameter (cm)	Total Height (cm)	Diameter Viewed On Secondary (cm)
19.0	11.0	2.55	14.40	1.30
24.0	11.0	3.25	13.58	1.63
28.1	11.0	3.83	12.96	1.88

Table 2.1: Properties of the STACEE DTIRCs.

2.2.4.2 The PMTs

PMTs are used extensively in particle physics detectors because of their fast response time (of the order of nanoseconds) and for their extreme sensitivity; they can detect single photons. The STACEE collaboration uses the Photonis XP2282B phototube with a borosilicate window and a VD182K/C transistored voltage divider. The borosilicate glass allows the passage of UV photons with wavelengths as low as 270 nm. The tube's bialkali photocathode provides a peak photoconversion efficiency of $\approx 28\%$ at a wavelength of 400 nm. The PMTs acceptance as a function of wavelength is plotted along with the reflectivity and transmission curves of the other optical components in figure 2.11.

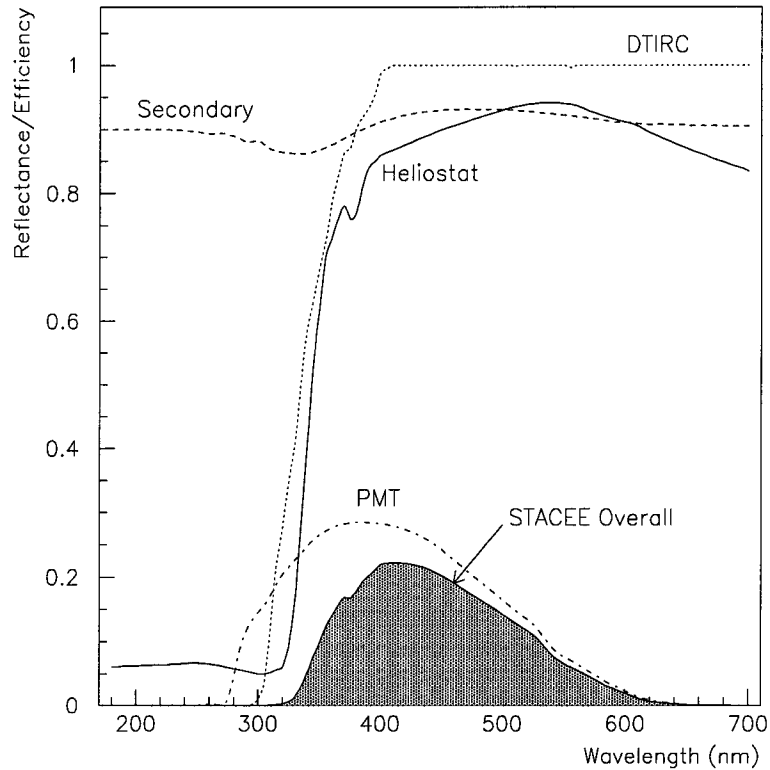


Figure 2.11: The optical throughput of the STACEE-32 telescope. The heliostat reflectivity, the secondary mirror reflectivity, the DTIRC transmission and the PMT acceptance as functions of wavelength are all included. The hatched area displays the net effect of all of these components.

This phototube can also handle currents up to $180 \mu\text{A}$, which is important for a high rate experiment such as STACEE where the tubes are exposed to the night sky. The properties of this tube are summarised in table 2.2 [59].

The basic requirements for PMTs in the STACEE experiment are that they have good response to Čerenkov (blue) light and that they be very fast. The specific timing properties of the phototubes that affect the resolution are usually related to how the discriminator can handle its output. These properties are the rise time of the phototube pulse and transit time spread (TTS). Since most

discriminators trigger on an edge, a fast rise time provides a more definite edge for the discriminator to trigger on. The TTS through the phototube is the intrinsic jitter in the timing of the pulses. It sets the lower limit on the timing resolution.

Spectral range	300-650 nm
Quantum efficiency at 400 nm	28%
Number of dynodes	8
Typical operating gain	1.1×10^5
Transit time spread (TTS)	0.5 nsec
Rise time	1.5 nsec
Typical dark current	5 nA
Diameter of photocathode	5.25 cm

Table 2.2: Specifications of the Photonis XP2282 photomultiplier tube.

Photons incident on the PMT surface generate electrons in a photocathode via the photo-electric effect. The single electrons are then accelerated up to energies of a few hundred eV in an electric field and focused onto the first of many multiplying stages or dynodes. Through the process of secondary emission, dynodes generate 2-10 electrons for every electron incident on their surface. Using this process large gains can be achieved. If the initial number of photoelectrons generated at the photocathode is n_{pe} and the gain at each diode is g_i then the total number of electrons arriving at the output of the PMT is:

$$n_k = n_{pe} \prod_{i=1}^N g_i \quad (2.6)$$

If the PMT has ten stages with a gain of 4 for each stage the current amplification M is:

$$M = \frac{n_k}{n_{pe}} = \prod_{i=1}^{10} g_i = 4^{10} \approx 10^6 \quad (2.7)$$

STACEE PMT gains were measured using two different methods. The first method used absolute gains determined for each tube individually with relative *in situ* gains. Absolute gains were measured in laboratory conditions by placing the PMTs in a dark box and digitising single photoelectron pulses with a 2 GHz sampling digital oscilloscope. The total charge in the pulse is integrated over 20 nsec, and the average charge as a function of applied voltage is determined. Figure 2.12 is a typical charge distribution used in the absolute gain calculation.

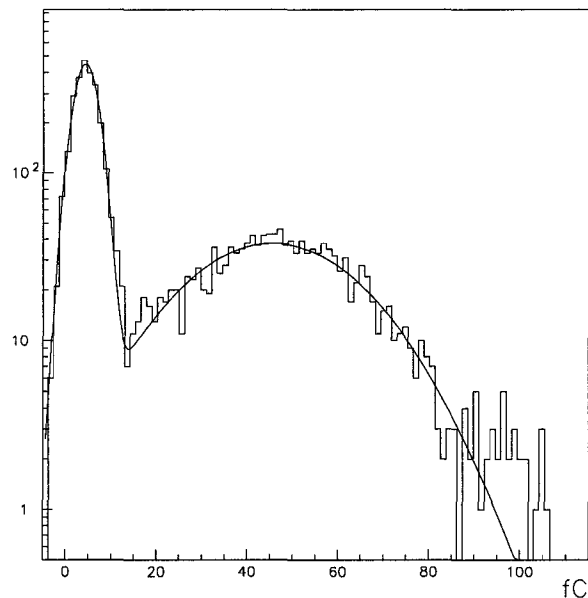


Figure 2.12: Pulse charge spectrum from a STACEE PMT used in the absolute gain determination. The light striking the PMT is kept very faint so that on average the number of photons striking the photocathode is much less than one. The first peak is pedestal. The second broad peak is the single photoelectron peak.

The relative *in situ* gain measurements were performed with the PMTs deployed in the camera at the 260' level with the use of a light emitting diode (LED).

The LED is pulsed, and the amplitude of the resulting PMT signal is measured with an oscilloscope. The *in situ* measurement provided superior relative gain measurements (to better than 5%) for every tube under actual conditions. The absolute gain measurements performed in the lab are combined with the relative *in situ* measurements to determine a final set of absolute gains, with the overall normalisation taken from the absolute gain measurement.

The second gain measurement method used a statistical approach. Due to statistical fluctuations in the number of photoelectrons released at the first dynode, the width of the charge distribution varies with the square root of the light intensity, while the mean of the distribution shifts linearly with the intensity. The ratio of the square of the distribution's width to the mean of the distribution should then give a quantity proportional to the absolute gain [60]. The two methods used to determine PMT gains agreed to within $\sim 10\%$.

2.2.5 Electronics

STACEE's electronics requirements are quite unusual. Most of the electronics are devices well known in the particle physics community: discriminators, time to digital converters (TDC), analogue to digital converters (ADC), counters and coincidence units. The electronics system block diagram is presented in Figure 2.13. These units operate in the NIM and CAMAC standards. What makes the system requirements unique is that we are using the detector to trigger on events from a moving source. In order to form the coincidences (see section 2.2.5.3), our delay modules have to be adjusted dynamically depending on the time of day and which source we want to observe. Figure 2.14 is a simple 2 dimensional example that illustrates how the delays for each heliostat are a function of the elevation angle.

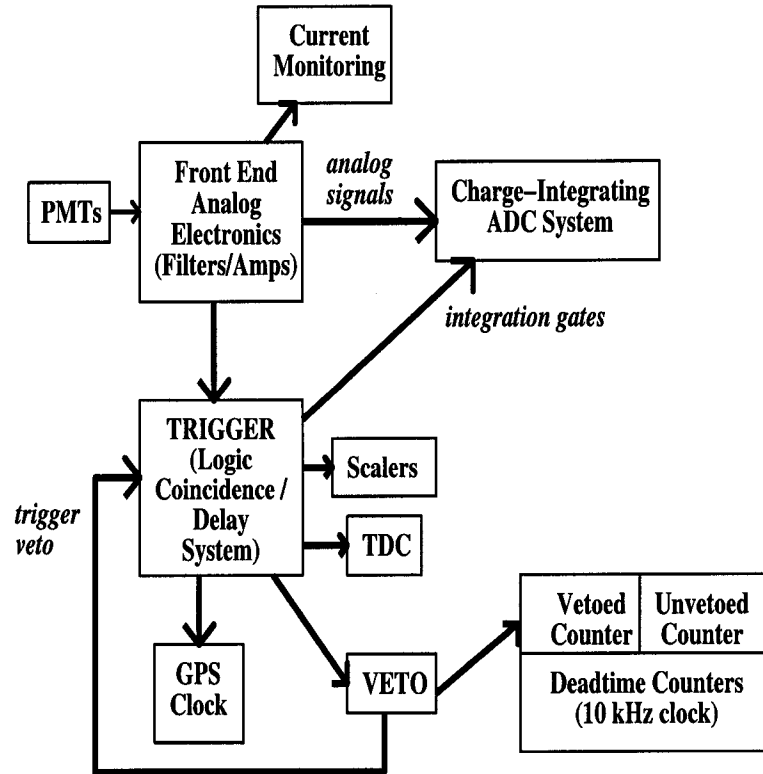


Figure 2.13: Block diagram representation of the STACEE-32 electronics system.

Figure 2.14 demonstrates the case for a two channel system. If we want to form a trigger on the incoming wavefront, the delay setting for the right heliostat will have to be $T_1 - T_2$ longer than the delay setting for the left hand heliostat.

The fact that we are using PMTs designed for extremely low light collection to observe the night sky also pushes us towards the design limitations of these electronics. For instance the individual PMT rates (that is after the phototube pulses have passed through a discriminator that only chooses those pulses which have an amplitude that would correspond to about 4-5 photoelectrons) are typically several megahertz. With these high initial rates (most of which are due to night sky background) a two level trigger system with the smallest possible coincidence forming time (of the order of 10 nsec) and timing data with a resolution of about

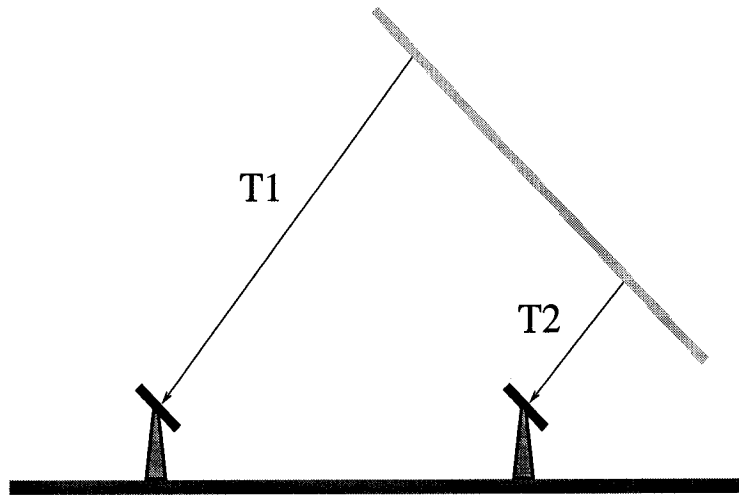


Figure 2.14: Simple 2 dimensional cartoon illustrating the dependence of the of the dynamic delays on the elevation angle. The light blue line represents the incoming Čerenkov wavefront. So that the signals from both heliostats arrive at the same time to the trigger formation system the signal from the right heliostat will have to be delayed by a time $T_1 - T_2$.

≈ 1 nsec must be used to reduce the amount of data recorded and to reconstruct the events offline.

2.2.5.1 Front End Analogue Electronics

The front end analogue electronics refers to all electronics between the phototubes and the trigger system at the 200' level. The PMT outputs are carried by 10 m long RF shielded RG58 cables to a small metal shed on the bay at the 260' level, called the "doghouse". The current output from each phototube is measured by passing the phototube's signal across a known resistance ($10 \text{ k } \Omega$) and measuring the voltage drop with a scanning ADC module (Joerger ADC-32).

Each signal from the phototubes is then passed through a high-bandpass RC

filter with an RC constant of 75 nsec in order to block out the DC component of the PMT signal and the slow PMT transients which are not associated with Čerenkov signals. Each channel is then amplified using two cascaded Phillips Scientific NIM 776 amplifiers for a total gain of 100. This amplification allows a lower gain operation of the phototubes which is necessary to prevent damage to the phototubes given the high night sky background. After the phototube output has been filtered and amplified it is sent to the 200' level via a 50 m long low loss RG213 cable. Once at the 200' level the signal is split using a linear NIM fanout module (Phillips Scientific NIM 748) with one copy of the signal going to the trigger system and the other to the ADC system.

2.2.5.2 Discriminators

After the fanout, one of the signal copies is sent to the discriminators. The discriminator modules (LRS 4413) play a pivotal role in the experiment. The discriminator threshold is an amplitude cut-off, below which one does not accept the phototube pulses. This parameter is critical when trying to lower the energy threshold. If the discriminator threshold is too low we will be accepting many background events; if it is too high the experiment will stray from its goal of measuring the lowest energy showers possible. That is why the discriminator thresholds are set every night: in order to keep the energy threshold as low as possible they must be set at the nearest point above the background, which changes on a nightly basis. Although some runs were taken at thresholds of 155 mV, the average discriminator threshold for the ON+231 data set was 128 mV. This discriminator threshold roughly translates to a threshold of 5 photoelectrons. Setting the discriminator threshold is a balancing act between accepting too many accidental triggers in the data and keeping the threshold energy as low as possible.

The “breakpoint” in the rate versus discriminator threshold plot is the low-

est threshold one can use before forcing the detector to take an unacceptably high number of accidental NSB triggers. To help find this point, the rate versus threshold curve (depicted in Figure 2.15) includes a similar measurement where the dynamic delays for the trigger system are scrambled. Since the arrival of NSB photons is random, the chance of triggering on them does not change when random delays are used. We can see that for the configuration in figure 2.15 there is a break point at around 95 mV. At discriminator threshold values below 95 mV the trigger rate consists mostly of accidental coincidences due to night sky noise. Above 95 mV the Čerenkov signal due to cosmic ray air showers starts to dominate the signal.

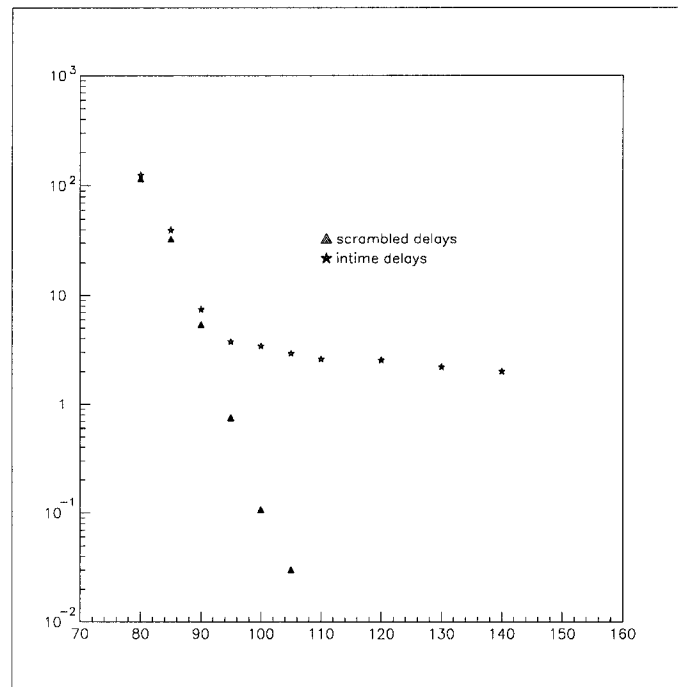


Figure 2.15: In this standard rate versus threshold plot the trigger rate (in Hz) is plotted as a function of the discriminator threshold (in mV). The scrambled delays show that as the threshold is increased the accidental rate falls off to zero and we are left with Čerenkov events.

2.2.5.3 Delay and Trigger System

For STACEE to be able to function, given the high rate environment the phototubes are exposed to, a multi-level trigger system must be used to reject the majority of the background. In order to lower the energy threshold to the minimum value, the coincidence formation time of this trigger system must be as short as possible. In order to impose a trigger within such a small time interval the signals from individual (and as we shall see, groups of phototubes) must be delayed so that their individual amplitudes can be summed and re-discriminated to form a trigger.

The 32 heliostats are divided into 4 groups of 8 heliostats. A group of 8 heliostats is commonly referred to as a cluster or patch. The heliostats composing the four clusters of the STACEE-32 prototype are shown in Figure 2.16. Before the master trigger can be formed, L1 triggers are formed from each patch. These L1 triggers are formed by delaying each individual discriminator pulse and requiring a coincidence of typically (for the ON+231 data) 6 of 8 individual tube triggers. The pulses are first delayed using three cascaded programmable delay modules (LRS 4518). The delays are calculated as a function of the direction of the incoming shower front calculated from the local pointing directions. The dynamic delay system can delay signals for up to 255 nsec with an accuracy of 1 nsec. In addition to the dynamic delays, static delays are used to compensate for the times of flight (TOF) from the heliostats to the secondaries. These delays are implemented by using the proper lengths of cable needed to achieve the TOF (given the speed of the signals in the co-axial cables). The signal pulses are re-discriminated to compensate for any deterioration caused by the TOF delay cables. A block diagram of the STACEE-32 delay and trigger system is presented in Figure 2.17. The delayed signals are then passed through an analogue sum module that combines the 8 channels into one signal; the outputs of the analogue

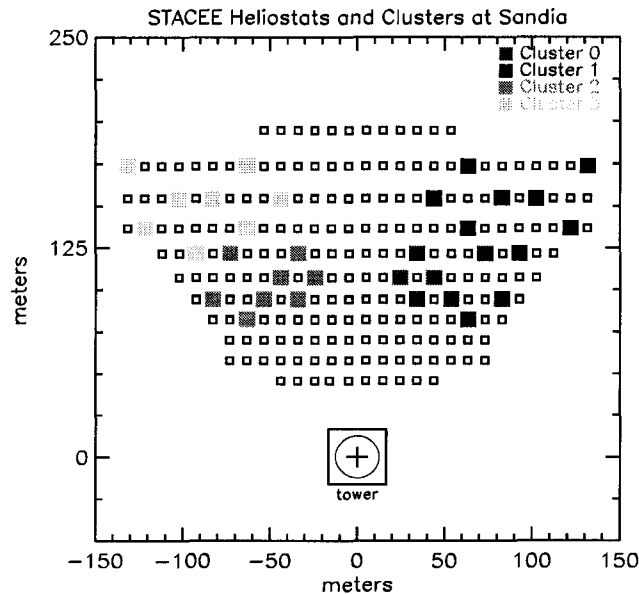


Figure 2.16: Diagram displaying the tower and the distribution of the STACEE-32 heliostats and their grouping into clusters.

sum modules are then sent to a discriminator (Phillips 711) that effectively sets the coincidence by applying the discriminator threshold. This coincidence can be set quite accurately since the sum module is summing fixed (discriminator output) pulse amplitudes. The coincidence is typically set at 6 or 5 channels out of 8. Commonly this is referred to as a “6/8” or “5/8” L1 trigger. The four L1 trigger patch rates are recorded with a scaler (LRS 2551).

Once the L1 triggers are formed the four patch triggers are sent to another delay module (CAEN C469) that is needed to form the second level trigger (the L2 or event trigger). The CAEN module can delay signals for up to 640 nsec to an accuracy of 2.5 nsec. The master trigger is formed in a logic coincidence module (Phillips 755) that is typically set to a “3/4” coincidence. The trigger conditions

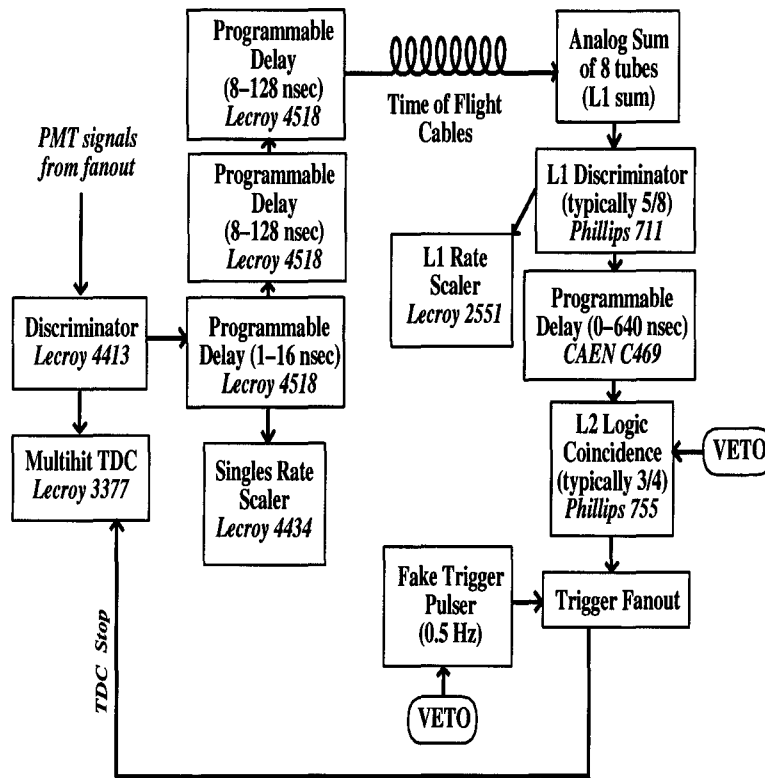


Figure 2.17: Block diagram representation of the STACEE-32 trigger formation and delay system. Not shown on this block diagram is the pulse reshaping discriminator that comes after the TOF cables and the ECL to NIM converter modules.

are thus referred to as “6/8 and 3/4” referring to the L1 and L2 coincidence requirements respectively. While the data from a triggered event is being processed by the DAQ, a veto signal is sent that prohibits the formation of additional triggers. In order to calculate the deadtime that results from the event veto, two copies of a 10 kHz clock signal are sent to the LRS 2551 scaler module. One of these clocks is never vetoed while the other is gated by the veto signal sent to the trigger electronics.

Calibration triggers, known as “fake” triggers, are taken at a rate of 0.5 Hz. These fake triggers are generated using a gate generator and are completely inte-

grated into the trigger logic: they generate the same chain of events as a real trigger. These triggers are useful for determining PMT rates, currents and pedestal values. When a trigger, fake or real, occurs, the veto signal preventing the taking of additional triggers is issued, the event readout is initiated, a common stop signal is sent to the TDC's, a GPS clock is read out to time-stamp the event and ADC integration gates are sent to the ADC for 24 of the 32 channels.

A block diagram of the ADC system is shown in Figure 2.18. In the ADC system the trigger signal is fanned out and each copy is delayed by a programmable CAEN C469 delay module. The delays on the gates are calculated so that the gate opens 5 nsec before the analogue signal reaches the input of the ADC module. The delays are updated as the source is tracked across the sky. For the STACEE-32 prototype only 24 of the channels were equipped with ADCs. This was a consequence of budgetary constraints, and will be addressed in the future incarnations of the STACEE telescope by substituting this system with a fast sampling waveform digitiser or Flash ADC (FADC). Since the ADC data were not used in the analysis of the ON+231 data, the reader is referred to a more detailed description of the system and its limitations in [61].

2.2.5.4 Laser Calibration System

In order to calibrate the electronic system and DAQ, and to obtain the time slewing corrections, a laser calibration system was devised for STACEE-32. This system uses a nitrogen laser with a dye wavelength shifter [62]. The laser is located on the 200' level of the tower and the light pulses from the laser are guided up to the 260' level by long fibre-optic cables. The light is flashed from wavelength shifter plates located at the centre of each secondary mirror. Filter wheels are used to control the intensity of the laser flashes. A PIN photodiode measures the amplitude of a copy of the pulse for calibration checking.

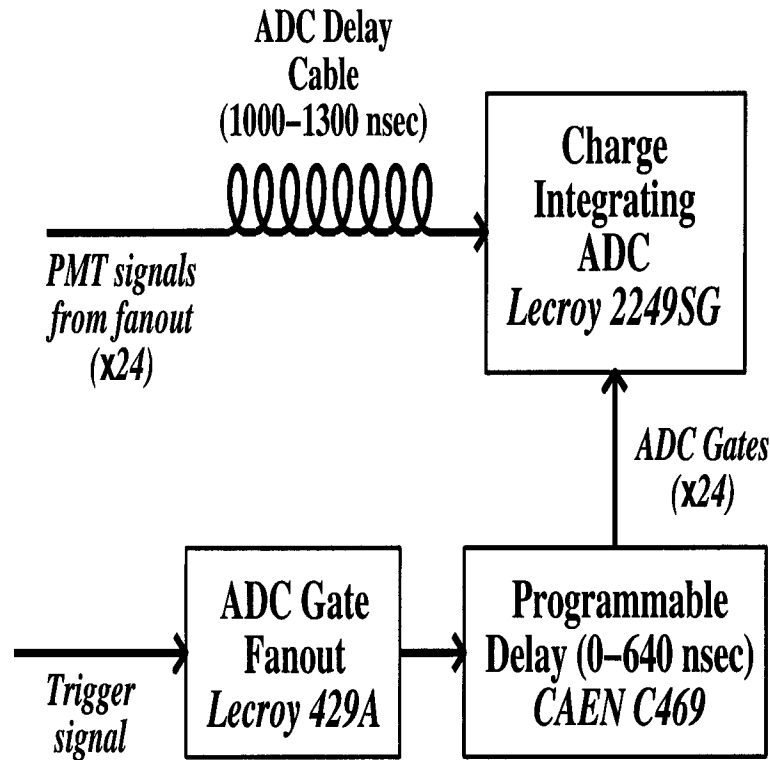


Figure 2.18: Block diagram representation of the STACEE-32 ADC system.

The laser is used to flash each camera with short, Čerenkov-like light bursts. Since each phototube is illuminated simultaneously, the laser can be used to measure the transit time of the PMT signals through the phototubes and electronics. This timing data is used in the setting of minor corrections in the delay calculation (trims). Due to slewing effects, the transit time will in general depend on the amplitude of the pulse being measured. By recording the TDC values for laser pulses of different amplitudes (measured with ADCs), one can determine pulse slewing corrections on a channel by channel basis.

2.2.5.5 Data Acquisition

The Data Acquisition (DAQ) system for STACEE-32 consisted of a Silicon Graphics Indy computer interfaced to the electronics via a Hytec Ethernet CAMAC crate controller. On a run by run basis the DAQ could be used to:

- start or stop runs
- set the discriminator thresholds
- set the high voltage settings
- add environmental information (shift takers, weather conditions, etc) to the data

The discriminator thresholds could be adjusted remotely before each run. The high voltage (HV) control system also resided on the DAQ but used independent software to talk to the mainframe. The DAQ used the right ascension and declination of the observed targets, along with the GPS time, to calculate the variable trigger delays sent to the LRS and CAEN delay modules. All alarms and warnings that could occur during a run (ranging from lack of disk space to high current PMT warnings) were also handled in the DAQ.

On an event by event basis the DAQ read out all of the ADCs, TDCs, scalers and the GPS clock. Event data structures were constructed in the SGI's shared memory arenas where various other processes (such as the alarms process and the monitoring processes) could access this event information in real time. After readout was complete the DAQ cleared the trigger veto to re-enable data taking. The data were stored locally on the SGI hard disk and wrote out to DLT tape at the end of each shift to be shipped to McGill and the University of Chicago for offline analysis.

2.2.5.6 High Voltage and Current Monitoring

The 32 PMTs in the experiment need to be supplied with a constant 1200 to 2000 Volts (depending on the individual PMT). This was achieved using an LRS HV4032 mainframe, which provided 32 channels of DC high voltage, located in the doghouse on the 260' level. This mainframe was controlled remotely from the DAQ SGI, in the 200' level control room, by using a LRS 2132 CAMAC interface module that communicated with the mainframe via ribbon cable. HV control software was kept independent of the main DAQ software so that emergency shut offs of the HV could be initiated irrespective of the DAQ program process status. Once operating HVs had been determined, through a process of gain equalisation, (the gain measurements are described in section 2.2.4.2), the HV control software was used at the beginning of the run to load the high voltage values into the HV4032 buffer and to turn on/off the HV from the control room in the 200' level.

The PMT current was calculated from the output of the scanning ADC and monitored from the alarms process within the main DAQ software. The alarms process monitored the currents and issued audio and visual warning messages to the user via the main DAQ graphical user interface (GUI) if individual tubes were higher than a predetermined threshold. If currents reached a potentially dangerous level, the current monitoring software shut off the HV without the shift takers' confirmation and then notified the user of the problem via the main DAQ GUI. See Table 2.3 for the various conditions for warnings and for the high voltage trip.

Current Monitoring Condition	Action
Single tube current $> 70\mu\text{A}$	Warn the user
Average current for one camera $> 70\mu\text{A}$	Warn the user
Single tube current $> 175\mu\text{A}$	Turn HV off
Average current for one camera $> 85\mu\text{A}$	Turn HV off

Table 2.3: Warning and HV trip conditions used for the current monitoring process.

Chapter 3

Simulations of STACEE-32

Monte Carlo studies play important roles in the design of any high energy physics detector and in the analysis of the data gathered from such a detector. In an accelerator based detector or with a satellite based telescope, one can always use test beam results to characterise the response of the detector. Unfortunately, for an experiment such as STACEE that uses the atmosphere itself as a calorimeter, there exists no test beam. For this reason we must rely on Monte Carlo studies to understand the response of the atmosphere and telescope. The problem is further complicated when one considers that the atmosphere itself would make a poor choice as a calorimeter: it consists of several substances, it varies in density and is not stable in time. Luckily there exist extensive MC packages for the purpose of modelling the atmosphere.

From a purely instrumental point of view STACEE also poses serious challenges. Until we built and tested it the technique of using a solar power plant as an ACT was not proven; even though valuable scientific data was collected with STACEE-32 it was still a prototype. Luckily we had a start: the NSTTF was a fully functional facility and most of the electronics and phototubes to observe

Čerenkov light could be bought off the shelf. Like most accelerator based experiments the characterisation of the instrument is based on a chain of models: one for the basic physics, one for the phenomenological consequences of the initial reactions and several other modelling packages for the various hardware systems in the detector. One can describe the model chain by following the path of an initial particle through the various components. We use this approach in the following sections: we shall consider the event path of initial atmospheric events, through the atmosphere, onto the field of heliostats, through the various optics and into our trigger system.

3.1 Atmospheric Shower Simulation

Initially air shower simulations were done analytically using empirical data. Models used today have espoused the Monte Carlo technique to simulate extensive air showers. These models combine experimental nuclear and particle physics cross sections with standard meteorological data to predict shower evolution in the atmosphere. The two most widely used atmospheric shower simulation packages today are MOCCA [63] (the package chosen for predicting STACEE-32's response) and CORSIKA [64].

3.1.1 Monte Carlo Technique

The Monte Carlo method is a technique used to perform complicated, multi-dimensional integrals. As its name indicates, the Monte Carlo method, works by choosing initial events at random, and letting these events evolve through whatever model we have. A good example of how the Monte Carlo technique works would be the example of trying to calculate the area of a pond in a field. It

would be difficult to do this using standard numerical integration techniques since ponds have mathematically indescribable shapes. If the pond is contained within a field of known geometrical shape, say a square for simplicity's sake, one could estimate the area of the pond by throwing stones randomly and uniformly into the field and counting the number of stones that are accompanied by a splash.

The ratio of stones that fell into the pond to the total number of stones is equal to the ratio of the area of the pond to the known area of the field. From this simple example it is also easy to see that instead of having an error that is determined by the number of degrees of freedom, the error is statistical in nature [65]. So by using computers to generate large numbers of Monte Carlo events one can obtain good relative errors.

3.1.2 Atmospheric Modelling

The MOCCA package requires a choice of specific atmospheric parameters. The atmosphere's response to high energy radiation is difficult to model because its density and composition vary as a function of depth. When considering Čerenkov light produced in these showers, these variations result in changes in the index of refraction of the atmosphere which play an important role in the end photon yield of the shower. For STACEE the atmospheric input uses a five layer model, in which the density profile follows an exponential distribution with a characteristic scale height in each zone [61]. The model parameters are determined from a parameterisation of the U.S. standard atmosphere [63]. When considering atmospheric models one must look at the various Čerenkov light attenuation mechanisms present: namely Rayleigh and Mie scattering and molecular scattering. These mechanisms are all included in the atmospheric model. The most important source of atmospheric attenuation for STACEE is Rayleigh scattering.

The regime of Rayleigh scattering is when scattering centres can be considered small compared to the wavelength of the scattered light. In Rayleigh scattering, electrons surrounding the atom are set into forced oscillation of the same frequency as the electric field of the incident light wave. This induced electronic oscillation produces ultra-violet light (since the resonant frequencies of bound electrons are in this energy regime) that is irradiated in all directions. The irradiated intensity can be shown to be inversely proportional to the fourth power of the wavelength, which leads to an absorption length that is directly proportional to the fourth power of wavelength:

$$L = \frac{3}{32\pi} \frac{N\lambda^4}{(n-1)^2} \quad (3.1)$$

In this equation N is the number density of molecules, atoms and ions, λ is the scattered photon's wavelength and n is the index of refraction. This property is the reason why Rayleigh scattering affects Čerenkov effect experiments: photons at the lower wavelength end of the visible light spectrum (where the Čerenkov photons are most likely to be situated) are preferentially scattered through this process.

Scattering of Čerenkov photons by molecular oxygen (O_2) and ozone (O_3) is a small effect [10] since this process only absorbs wavelengths that are below 340 nm [66]. This wavelength regime is below STACEE-32's peak acceptance frequency.

Mie scattering occurs when light is scattered by particles or refractive index inhomogeneities of a size of the order of the wavelength of the light. Mie scattering uses the well known laws of refraction and reflection applied to relatively large particles or droplets, suspended in the atmosphere: mostly dust, pollution and water vapour. All wavelengths are scattered so if white light hits a region of particles that are of the right size to allow for Mie scattering, the scattered light will also have the same spectrum. This is the reason why clouds are white. Figure 3.1 shows the Mie scattering cross section of white light with particles of

various size. This being said, Mie scattering is not meant to account for specific cloud formations that could interfere with the STACEE data. STACEE uses an empirical model for Mie scattering measured by the Santer experiment [67]. The effect is small compared to the losses due to Rayleigh scattering since most particles that would scatter light using the Mie mechanism are near to the ground (≈ 1 km from the ground). This represents a short path length compared to the 10 kilometres light travels from the shower maximum position in the atmosphere. For the larger parts of the Čerenkov photons' path lengths, Rayleigh scattering would occur, thus Rayleigh scattering dominates over Mie scattering.

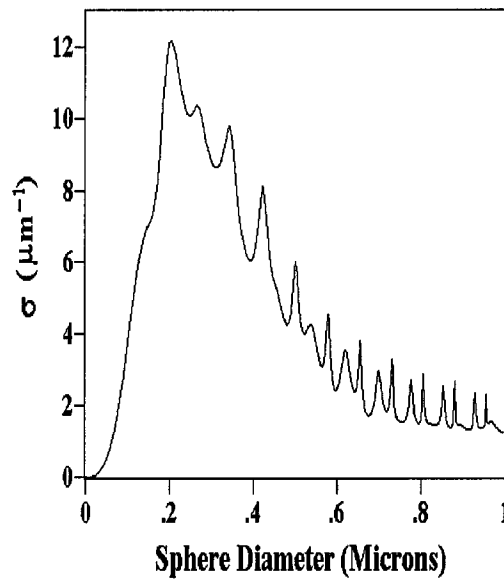


Figure 3.1: Mie scattering coefficient for white light plotted versus particle radius. The scattering coefficient is the cross section divided by the particle volume.

3.1.3 MOCCA Shower Simulation Package

To simulate showers in the atmosphere the STACEE collaboration used the MOCCA simulation package. MOCCA simulates air showers by following shower development from the initial interaction down to when the secondaries reach the ground or when they fall below the energy threshold needed to continue the shower process. Showers are simulated using a recursive process. For every interaction in the shower the subsequent products of the reactions are traced down until their energies prohibit them from further reactions. Each time a particle is produced or scattered, the simulation follows that 'branch' to the end, until all the possible branches have been traced. The main processes that MOCCA simulates during these reactions are bremsstrahlung, ionization, pair production and Coulomb interactions. The earth's magnetic field is also taken into consideration.

MOCCA's chief shortcoming is in the modelling of hadronic interactions. Hadronic cross sections can be difficult to calculate and the outcomes of nuclear reactions are generally more complex than those of electromagnetic reactions. In air showers many reactions involve the heavy nuclei that constitute the atmosphere. Most knowledge of hadronic interactions comes to us from accelerator experiments where the interactions are tested with simple hadrons. Hadronic interaction modelling in air showers relies on extrapolations from these data to lower energy regimes that are poorly constrained by direct measurement. MOCCA uses the "almost simplest splitting representation of scaling" for hadronic interactions and a simplified model of nuclear interactions where most Lorentz transformations are ignored and where the production and decay of short lived intermediate particles are ignored [68, 69].

For STACEE-32, the most important input parameters in MOCCA are the initial particle's type (one can choose between photons and particles of different

atomic numbers), energy and direction. Although there are many other parameters these don't tend to change on a shower to shower basis.

3.2 Telescope Simulation

Sandfield (short for Sandia Field Simulator) is a simulation package developed by the STACEE group to model the optical properties of the NSTTF and the STACEE optics, and thus the optical throughput of the detector for photons from atmospheric Čerenkov showers. Sandfield traces the optical path of simulated atmospheric Čerenkov photons from their arrival on the heliostats to the secondary mirrors, through the DTIRC's and finally to the front face of the phototubes. The package takes MOCCA output files and a parameter file as input and produces a list of photoelectrons generated at each PMT. In order to optimise computer resources a single MOCCA shower can be used several times by re-scattering the primary hit location randomly over a circular area. The parameter file represents an excellent summary of our understanding of the experiment. Actual calibration measurements of the detector ranging from the positions of the components of the detector to the optical properties are used in the package. The absorption of Čerenkov photons is taken into account by recording the wavelength dependent properties of the heliostats, secondaries, DTIRCs and cookies.

3.2.1 Heliostat Modelling

Although the NSTTF heliostats were initially conceived to collect sunlight on an industrial scale, their optical properties also permit them to be used for collecting Čerenkov light. One can conceptualise these large mirrors as an array of 25 facets, each one having a slight parabolic shape with a focal length tuned to the distance

of that heliostat to the tower. However, to model these mirrors as so would lead to false results. Heliostats are made to concentrate light on an industrial scale and with the accompanying level of accuracy: the spot sizes for heliostats are $\sim 2m$. The shape of the facets is not perfectly parabolic due to the rather simple mirror bending mechanism (discussed in section 2.2.2) and because the glass has sometimes cracked. These imperfections often resulted in irregularly shaped images that can't be modelled from simple geometric optical models of the facets. To address this problem, measurements of each heliostat's image of the Sun were taken with a CCD camera [70] and corrections to the idealised models were incorporated into the sandfield package. Figure 3.2 shows a CCD image of a sun calibration spot.

Because the angular size of the Sun is comparable to the angular size of an atmospheric shower viewed from the ground, one can use the Sun to obtain information about the optical collecting properties of the heliostats. Imaging the Sun with a heliostat can give a good measure of the light density distribution produced by a heliostat. The proportion of total light gathered as a function of the radius of an idealised circular image on the tower is a good means of quantifying the spot accuracy. These plots of efficiency as a function of radius are called sun calibration curves. These curves have been successfully modelled within sandfield by giving each ideal facet image a Gaussian error. The linear displacement of the image on the tower was expressed in terms of a parameter called σ , and corresponds to the RMS of the error distribution. The σ parameter reflects how well each facet was aligned and had a typical value \sim of 0.5 m. The σ parameter was determined by fitting the sandfield simulations to sun calibration curves. Figure 3.3 shows a comparison of simulated and measured sun calibration curves for four heliostats. The fraction of the total light within a radius is plotted as a function of the radius.

A secondary source of light loss in the heliostats is absorption. Because the

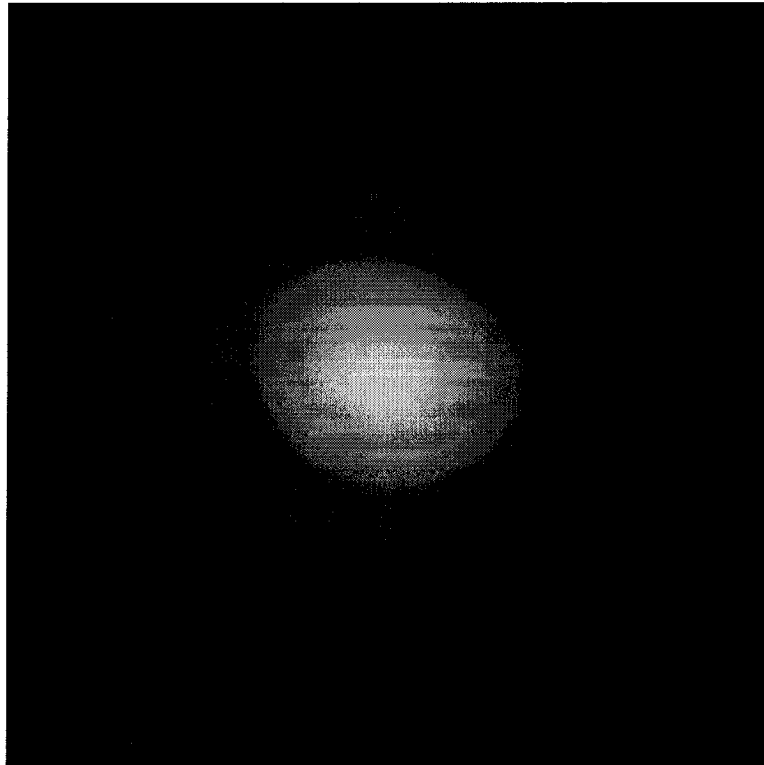


Figure 3.2: CCD image of a sun calibration spot for an NSTTF heliostat used in STACEE-32. One notices that the image is not uniformly circular and thus differs from an ideal spot. The vertical deformation of this image is due to “bleeding” caused by CCD saturation [70].

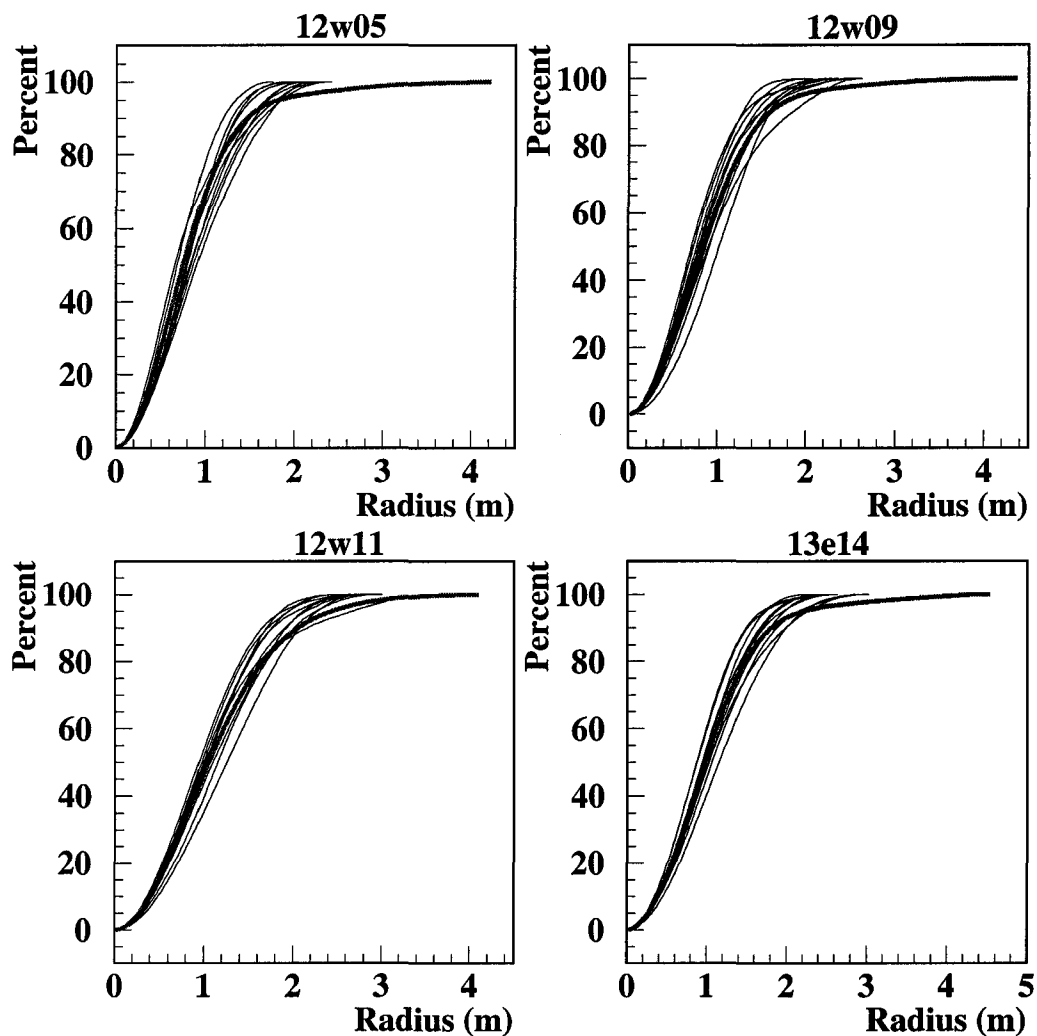


Figure 3.3: Measured sun calibration curves for four heliostats plotted with 10 simulated curves. The measured curve is the thick line and the simulated curves are in thinner lines. At a one metre radius we are capturing approximately 60 percent of the light. From these plots one could conclude that most sun calibration spots have a radius of approximately 2m.

facets are back silvered, light is absorbed as it passes through the glass twice. The sandfield package also accounts for absorption of light from the heliostats.

3.2.2 Secondary Mirror Modelling

At every step of the STACEE optical system, some Čerenkov photons are lost. The secondary mirror is no exception. STACEE's off-axis optics are the most significant source of photon loss. The photons are specifically lost in off-axis tails that stretch beyond the contour of the DTRICs and also in occultation by the cameras themselves. Figure 3.4 demonstrates the loss of Čerenkov photons due to camera occultation when 10000 showers from a fake moon at zenith were used in the simulation. Camera occultation was a more serious source of loss for heliostats that were closer to the tower. For the nearest heliostats nearly 25% of the photons were lost due to camera occultation. This number grew to 40% when the camera boxes (boxes that were constructed and installed around the cameras to shield them from rain) were included [71].

Since the secondary mirrors are front silvered (unlike the heliostats) losses due to absorption at the secondary are comparatively small but still included in sandfield. The mirrors themselves are modelled as spheres and because the modelling relies on an exact ray trace it automatically accounts for any spherical aberrations. The mirrors' exact positions were measured with surveying equipment while they were assembled.

3.2.3 DTIRC and Cookie Modelling

The sandfield package includes a 3 dimensional optical ray trace of photons through a DTIRC. This ray trace includes dielectric reflection off the spherical front face

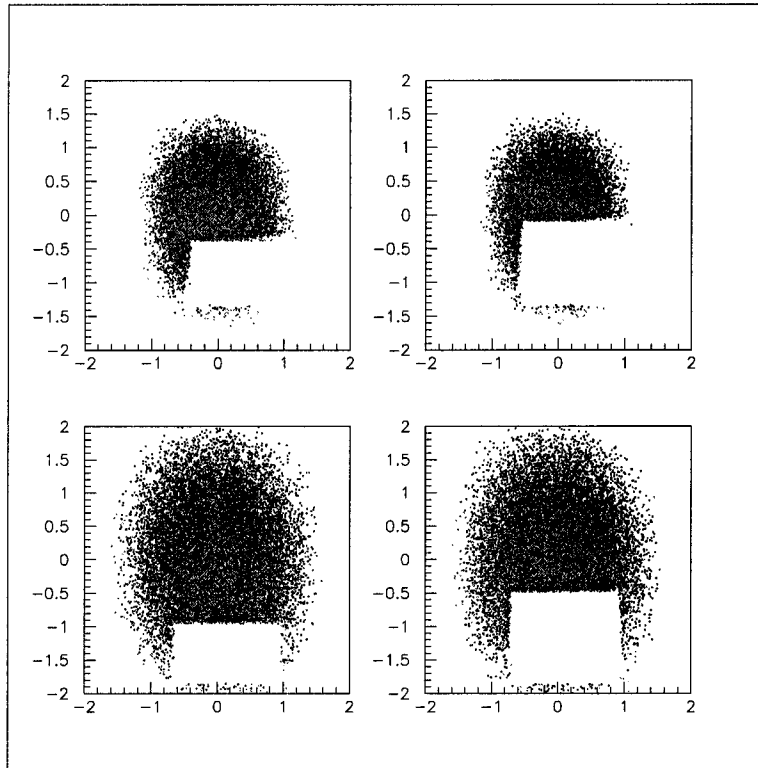


Figure 3.4: Simulated secondary spot images from a nearby STACEE-32 heliostat (top) and a distant heliostat (bottom). The right images include the camera box, left images are with the camera only.

and internal reflection off the sides and the bottom of the DTIRC. On the bottom the different index of refraction from the DTIRC to the silicon cookie is also taken into account. The optical cookie used to couple the DTIRC to the photocathode is also modelled. Dielectric reflections at the DTIRC-cookie and cookie-photocathode boundaries are taken into account. The cookie's absorption curve was folded into the model. Figure 3.5 shows the transmission as a function of incident angle.

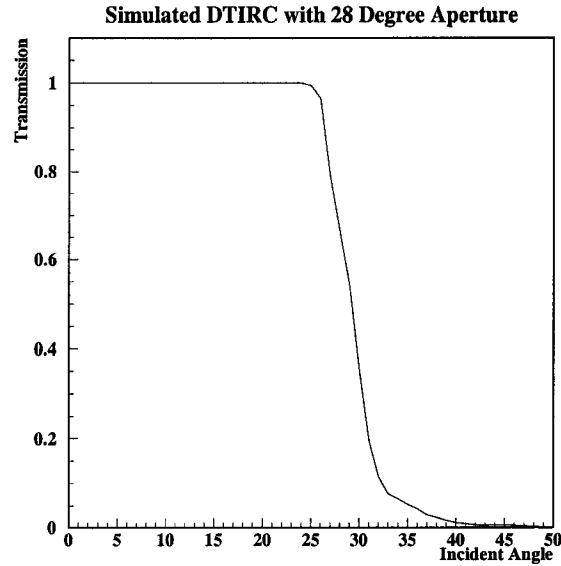


Figure 3.5: The transmission curve plotted as a function of incident angle for a DTIRC with an opening angle of 28° . The 100 % transmission is due to the fact that the absorption of the SNO acrylic is not accounted for in this plot.

3.2.4 Modelling of the Photocathode

The Philips product catalog only considers the photocathode response as a function of wavelength in its description of the PMT quantum efficiency [59]. In fact the photocathode's quantum efficiency (QE) varies as a function of incident angle also, as shown in figure 3.6. This angular dependence is due to a variation in the thickness of photocathode material being traversed by a photon when entering the front face at an angle. The exact theory is more complicated and takes loss inside the photocathode into account by introducing a complex index of refraction. The model takes into account 3 distinct optical path sections shown in figure 3.7. On average, the enhancement of the PMT QE for oblique incident angles increases the QE for Čerenkov photons by $\sim 11\%$ [61]. Variations of the QE as a function

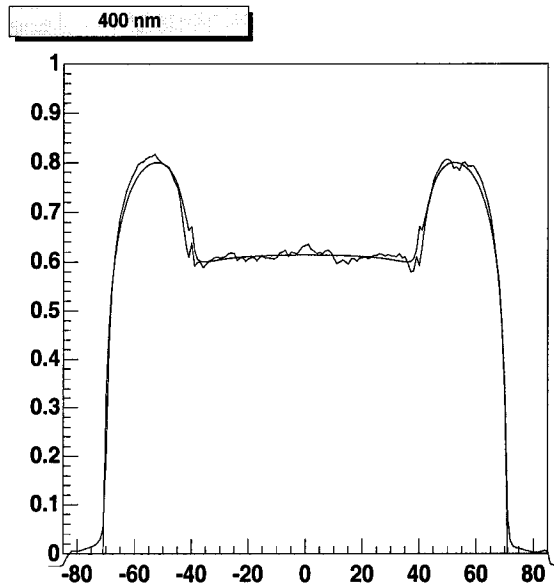


Figure 3.6: Photocathode efficiency plotted as a function of incident angle of the arriving light. The smooth line is the model while the jagged line is data. The thickness of photocathode material was assumed to be uniform and 30 nm thick [72].

of the position on the photocathode are not included in the simulation.

3.2.5 Trigger Model

Once showers have been generated and the Čerenkov photons tracked through the optics we must decide whether the photoelectrons from an individual shower trigger the experiment. This task is accomplished by a trigger model. Čerenkov photons that pass the optical modelling are sorted according to their arrival time, various timing and amplitude cuts corresponding to settings in the experiment are applied, and if the shower passes these cuts, the event is considered accepted. The trigger model algorithm can be summarised in five steps:

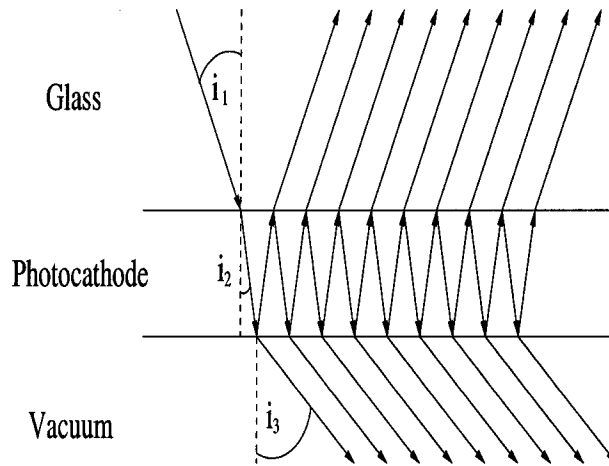


Figure 3.7: Light ray diagram of the photocathode showing the three optical path sections. The first section experiences loss because of the reflection at the glass-photocathode interface. The second section experiences attenuation inside the photocathode material where the index of refraction is complex. The third section simply considers the light ray angle in the vacuum.

Initial Check: Passive Trigger To save processing time a passive trigger is imposed as soon as the sandfield output is read. The passive trigger only checks to see if the minimum number of photoelectrons have arrived on each photocathode irrespective of timing considerations and then imposes the $6/8$ $3/4$ trigger conditions used for most of the ON+231 data. If a shower does not pass the passive trigger it is rejected and the next shower is read from the sandfield output file.

Dynamic Delays Before any timing cuts can be applied to the photoelectrons, the dynamic delays used in the actual experiment must be calculated and applied to the photoelectron arrival times. These delays are calculated from the azimuth and elevation angles and assume spherical wavefronts.

Individual Tube Trigger The photoelectrons from events that have passed the passive trigger are sorted according to their arrival times on a tube by tube basis. A 5 nsec sliding time window is applied to the sorted photoelectrons. If the number of photoelectron arriving within the time window exceeds the photoelectron threshold (N_{pe}), that tube is considered to have triggered and the activation time for that tube is considered to be the arrival time of the last photon in the group of N_{pe} that triggered the tube.

L1 Trigger Once all the tubes have been checked for individual tube triggers, the activation times are sorted and a second sliding time window is passed through these times on a cluster by cluster basis. If one finds a number of tubes exceeding the L1 trigger setting (6/8 for these studies) within a 13 nsec time window, an L1 trigger is said to be formed. This time window width was chosen as a result of the L1 trigger model that was used to model the L1 rates described in section 4.2.2. The L1 trigger is then time-stamped using the average of the individual tube times that participated in the L1 trigger.

L2 Trigger The L1 trigger times are then sorted and a third time window, this one corresponding to the setting in the Level 2 trigger electronics (20 nsec), is applied. If at least 3 L1 triggers are in a 20 nsec window, the event is considered to have triggered the experiment.

The most critical parameters in this model are the photoelectron threshold, N_{pe} , and the single tube trigger formation time. The photoelectron threshold, analogous to the discriminator threshold, is set at 5 photoelectrons. With the amplification provided in the front end electronics a single photoelectron generates a ~ 25 mV amplitude pulse. The average discriminator threshold for the ON+231 data was 128 mV, (Table 3.2.5 shows the complete list of threshold values), so the photoelectron threshold is set to 5 photoelectrons/tube. The time taken to

Run1	Run2	Threshold	Trigger Conditions
		(mV)	L1 L2
1186	1187	155	5/8 3/4
1188	1189	155	5/8 3/4
1242	1243	130	6/8 3/4
1244	1245	130	6/8 3/4
1254	1255	130	6/8 3/4
1258	1259	130	6/8 3/4
1268	1269	125	6/8 3/4
1270	1271	125	6/8 3/4
1273	1274	125	6/8 3/4
1275	1276	125	6/8 3/4
1318	1319	125	6/8 3/4
1320	1321	125	6/8 3/4
1322	1323	125	6/8 3/4
1333	1334	125	6/8 3/4
1434	1435	115	6/8 3/4
1436	1437	115	6/8 3/4
1445	1446	115	6/8 3/4

Table 3.1: Run summary with discriminator settings and trigger conditions.

form a single tube trigger was initially taken simply as the thickness of a Čerenkov shower ~ 5 nsec. The actual shape of a shower as it hits the array is not a perfect thin spherical shell with a finite thickness; there are lagging photons behind the initial front that in reality don't participate in the trigger. Figure 3.8 is a plot of arrival time versus distance from the shower core for a typical shower. One can note the 5 nsec thick wavefront and the late photons behind this shell.

For this reason as one increases the trigger formation time, the shape of the showerfront (as recreated by the detector) deviates from the spherical shape of the

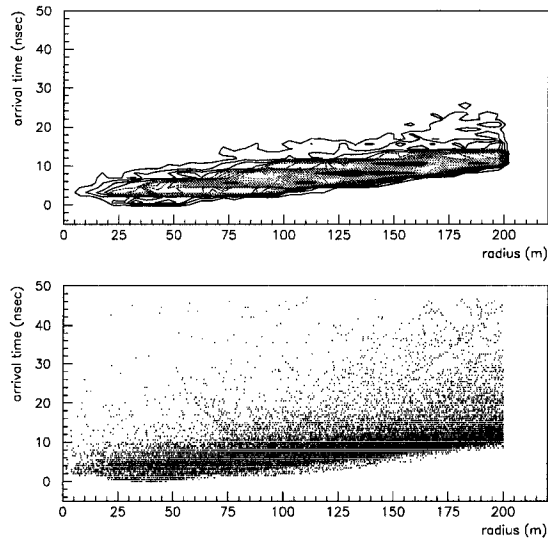


Figure 3.8: Plot and contour plot of arrival time vs radius for a typical 100 GeV shower. The spherical shell is well defined; but, many photons lag up to 40 nsec behind the initial front. If some of these photons are accepted into the simulation they can seriously affect the χ^2 values of fits to a spherical wavefront. The horizontal bands seen in the plots are an artifact of the simulation code. They are due to the 0.5 nsec time steps used in the simulation.

ideal γ -ray shower. On the other hand, if the trigger formation time is reduced below 5 nsec there would be loss of signal.

To test these two ideas, we varied the individual tube trigger formation time and observed the changes in the number of events that were accepted by the trigger model and the changes to the χ^2 distributions resulting from fitting the set of arrival times of each event to a spherical wavefront for 100, 200 and 500 GeV showers. The details of the fitting routine are discussed in section 4.2.7. The results of this study are summarised in figure 3.9 and table 3.2.

In figure 3.9 it is clear that at 3 nsec, fewer events are accepted by the trigger. This is consistent with our idea that below 5 nsec we are cutting out photons that make up the wanted signal. Because the trigger ratio flattens above 5 nsec, having a longer time window would not result in a significant increase in trigger ratio.

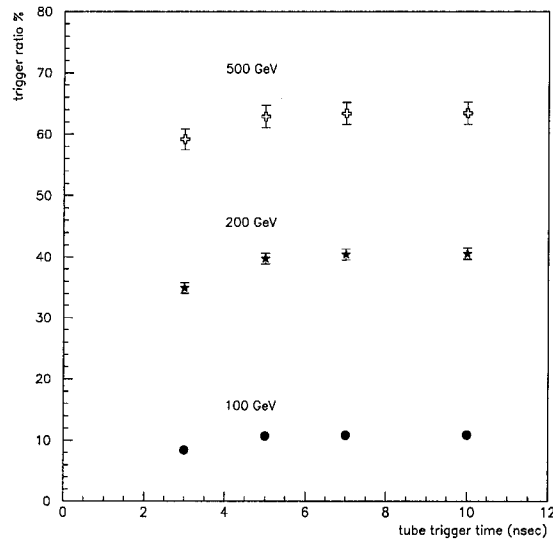


Figure 3.9: Plot of the trigger ratio versus tube trigger formation time. For all three energies one notices that at a tube trigger formation time below 5 nsec we start losing triggers.

To characterise the χ^2 distributions the ratio of events below certain cuts in χ^2 was calculated:

$$R_{\chi^2 < cut} = \frac{N_{\chi^2 < cut}}{N_{total}} \quad (3.2)$$

As the detected wavefronts approach the shape of a spherical shell, the value of $R_{\chi^2 < cut}$ will increase. As these detected showers deviate from the ideal wavefront, a greater proportion of the events will have higher χ^2 values, thus decreasing the value of $R_{\chi^2 < cut}$ as the tail of the χ^2 distribution becomes more important.

As the the tube trigger formation time is increased we notice, for all energies, a change in the χ^2 distributions. As the tube trigger formation time is increased the χ^2 distributions are shifted to higher χ^2 values. Telling us that as we increase the width of the sliding time window (individual tube trigger formation time) the shape of the wavefront accepted by the detector becomes less spherical. Basically, by accepting the lagging photons, we bias the wavefront shape away from the ideal thin spherical shell.

Energy (GeV)	Time Cut (nsec)	$R_{\chi^2 < 1.0}$	$R_{\chi^2 < 1.25}$	$R_{\chi^2 < 1.5}$
100	3	0.61	0.81	0.91
100	5	0.38	0.56	0.70
100	7	0.36	0.51	0.65
100	10	0.35	0.50	0.64
200	3	0.60	0.77	0.88
200	5	0.42	0.58	0.71
200	7	0.39	0.54	0.67
200	10	0.39	0.54	0.66
500	3	0.52	0.70	0.81
500	5	0.45	0.62	0.74
500	7	0.44	0.61	0.73
500	10	0.44	0.61	0.72

Table 3.2: Variation of the individual trigger time cut and its effect on the shape of the accepted wavefront. The timecut's effect on the shape is measured by noting the χ^2 of a fit to a spherical wavefront. This study is performed on 100, 200 and 500 GeV showers.

3.3 Simulation Results

MOCCA, sandfield and the trigger model combined constitute a complete simulation chain for the STACEE-32 telescope. The simulation chain described in this chapter was developed to determine the response of the telescope to cosmic rays and, more importantly, γ rays. In this chapter I will explain the major results of the simulation chain: the acceptance as a function of energy, (effective area curve), the cosmic ray rate and the efficiency of a χ^2 cut.

3.3.1 Cosmic Ray Rate

Most of the Čerenkov light hitting the STACEE detector is produced by cosmic rays. Every observing night, runs where the detector is simply pointed at zenith are taken to record the cosmic ray rate. By comparing the Monte Carlo data to “zenith” runs we have a powerful check of the simulation chain.

The first step in this calculation was to generate proton showers with the MOCCA package. The protons were generated with a differential energy spectral index of -2.75 , (i.e. with a flux Φ varying as $d\Phi/dE \propto E^{-2.75}$) in an energy range between 100 GeV and 10 TeV. The initial directions of the protons were scattered uniformly in solid angle about a 2° radius circle about zenith.

The response of the detector to these showers was then modelled with the sandfield field simulator. The sandfield package can “re-use” a specific MOCCA shower several times within a circular area of specified radius on the heliostat field. This option is useful because it saves substantial amounts of computer time and disk space. All wavelength dependent losses are included in the sandfield modelling. Once the Čerenkov photons were scattered and traced through the sandfield package, the trigger response was modelled with the trigger model. The

simulation was run at a threshold of 5 photoelectrons/tube, with 6/8 triggers for the L1 trigger and 3/4 L1 clusters for one global trigger, an individual tube trigger formation time of 5 nsec and an L1 trigger formation time of 13 nsec.

The measured differential flux for protons hitting the upper atmosphere is [73]

$$\left(\frac{dN}{dE}\right)_{\text{protons}} = (9.17 \pm 2.39) \times 10^{-2} E^{-2.76 \pm 0.09} (m^2 sr s TeV)^{-1} \quad (3.3)$$

The integrated flux of protons above 100 GeV is $(2.99 \pm 0.78) m^{-2} s^{-1} sr^{-1}$. To obtain the rate of protons predicted for the STACEE telescope one needs to multiply the integrated flux, the scattering area, the solid angle and the trigger fraction. The results of the cosmic ray rate simulations are presented in Table 3.3.1.

Simulated MOCCA proton showers	30255
Scatters per shower	10
Total number of scatters	302550
Number of triggered events	417
Proton Triggering fraction	$(1.38 \pm 0.11) \times 10^{-3}$

Table 3.3: Statistics of proton simulation. The uncertainty on the fraction of triggered events is statistical.

$$\begin{aligned} \textit{Proton Rate} &= \textit{IntegralFlux} \cdot \textit{Area} \cdot \textit{SolidAngle} \cdot \textit{TriggerFraction} & (3.4) \\ &= (2.99 \pm 0.78) m^{-2} s^{-1} sr^{-1} \cdot 250^2 \pi m^2 \cdot 2\pi(1 - \cos(2^\circ)) sr \cdot (1.38 \pm 0.11) \times 10^{-3} \end{aligned}$$

$$\textit{Proton Rate} = 3.1 \pm 0.79 Hz$$

(3.5)

Heavier nuclei are also present in the cosmic ray flux; but, they are less numerous and produce significantly less light (see figure 1.9). The lightest of these nuclei is helium. The helium trigger rate was determined in the same manner in a similar

study and was calculated to be 0.14 ± 0.04 Hz. The total trigger rate due to cosmic rays is thus predicted to be $\sim 3.24 \pm 0.8$ Hz. The actual observed rate from zenith run 484 was 2.92 ± 0.06 Hz. It was performed on a clear night with no known technical problems. The calculated cosmic ray trigger rate is therefore in reasonable agreement with the measured rate. This gives us a good indication that our simulation chain is in fact reproducing the detector response appropriately.

3.3.2 Effective Area Curve

The detector's sensitivity to γ -rays as a function of the energy of the γ -rays is characterised by an "effective area curve". The effective area is defined as:

$$A_{eff}(E) = \int P(E)dA \quad (3.6)$$

where $P(E)$ is the fraction of γ -ray showers that triggered the experiment and the integral is over an area sufficiently large so that at its outer limit $P(E) \rightarrow 0$. An effective area curve is generated by scattering showers over an area on the ground at different energies and measuring the fraction of γ -ray showers that triggered the experiment, $P(E)$. The telescope's response is measured as a function of surface area. Since $P(E)$, the probability a shower of energy E to trigger the experiment, changes with energy, so too does the effective area.

Since the detector response varies as a function of elevation and azimuth and every source tracks a different path through the sky the effective area must be calculated on a source by source basis. The majority of the ON+231 data set was collected at an angle of 7° from zenith with the azimuth angle varying from 150° to 250° . Figure 3.10 displays the distribution in azimuth and elevation angle (ϕ and θ) of the ON+231 data set. In order to simplify the calculation of the effective area, we calculate the effective area for a few points where most of the data can be represented. For our data set we chose two such points. The first point at

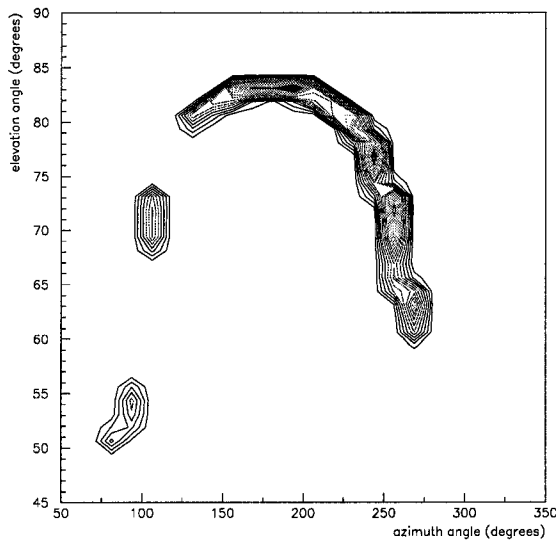


Figure 3.10: Contour plot of the azimuthal and elevation angle distributions of the ON+231 data set. The vast majority of the data lies in two distinct regions.

($\phi = 150^\circ$ and $\theta = 83^\circ$) is near the transit point of ON+231 path. We have checked that the effective area calculation is symmetric in azimuth angle around 180° (South) as expected from the geometry of the field. The second point is taken at ($\phi = 252^\circ$ and $\theta = 73^\circ$) and is used to represent the second large concentration of data at a lower elevation.

For each point the entire simulation chain must be used to determine the telescope’s response. First MOCCA showers are generated at point sources corresponding to the azimuth and elevation angles chosen. These showers are generated at energies of 50, 70, 100, 150, 200, 300, 500 and 1000 GeV. Since at low energies the triggering fraction approaches zero quickly, more points were taken at the lower energies in order to properly define the “turn-on” energy and steep rise in effective area that is typical of these experiments. Once these MOCCA showers have been generated, they are then scattered using sandfield over a radius of

200 m. When one examines figure 1.8 one is reassured that at a 200 m radius is sufficient for $P(E) \rightarrow 0$, since the density of Čerenkov photons on the ground diminishes quickly after ~ 120 m radius. Each shower is scattered 20 times over the array. The sandfield output files are then run through the trigger model with the standard settings for the ON 231 data set: a 6/8 and 3/4 trigger, a 5 nsec tube trigger formation time, a 5 photoelectron tube threshold and a 13 nsec L1 formation time. Once one has the triggering fraction for one energy one only has to multiply it by the scattering area ($200^2\pi m^2$). The effective area curves for both points are shown in figure 3.11.

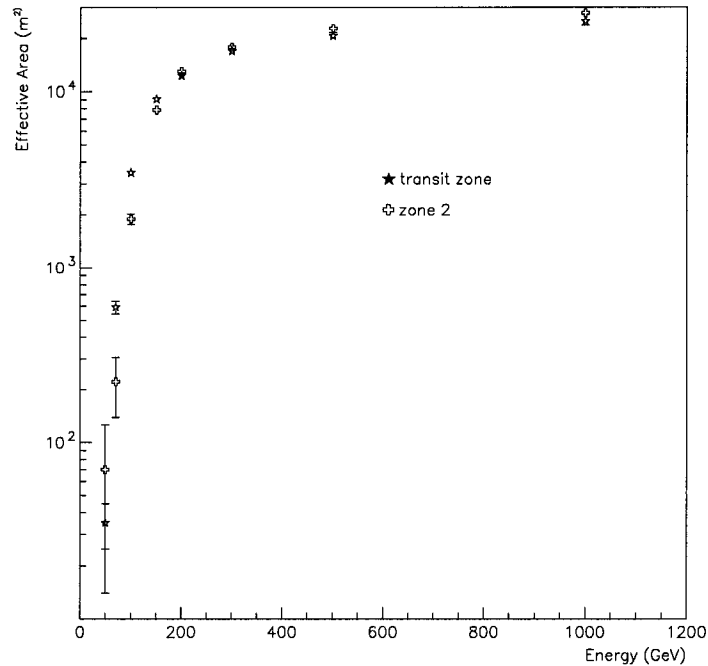


Figure 3.11: The effective area curves for the transit point ($\phi = 150^\circ$, $\theta = 83^\circ$) and the second point ($\phi = 252^\circ$, $\theta = 73^\circ$).

The lower elevation point has a larger maximum effective area, but has a larger

turn-on value. This is typical of the effective area curves for solar power based Čerenkov telescopes (see figure 3.12 and [74]). In order to use a single effective area curve, we perform a weighted average of both curves. Zone 1 is taken to

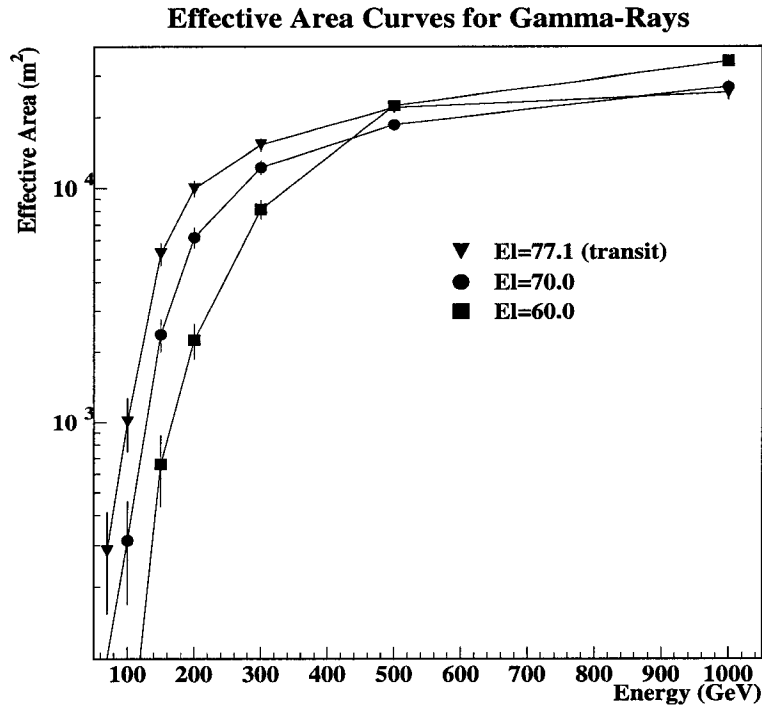


Figure 3.12: The effective area curves used in the STACEE-32 Crab analysis. The turn-on energy of the effective area decreases with elevation angle.

represent all events with an elevation greater than 80° , zone 1 contains 35% of the data. Zone 2 includes all events with an azimuth angle greater than 225° (roughly the azimuth angle where the previous zone ends), and represents 53% of the data. The weighted average of these two curves gives the final effective area curve depicted in figure 3.13.

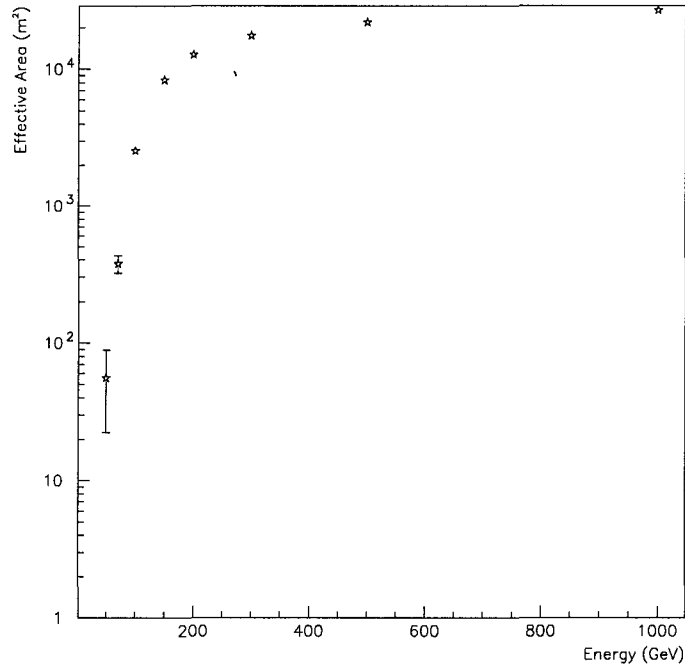


Figure 3.13: Plot of the average effective area curve for ON+231.

3.3.3 Calculating the Energy Threshold

In order to quote a physical flux from STACEE one needs two crucial data: our effective area curve (the acceptance of the detector) and an energy threshold. In an ideal detector the effective area curve would be a simple step function with the step at the threshold energy, E_{thresh} :

$$A_{eff}(E) = \begin{cases} 0 & : E < E_{thresh} \\ A_o & : E \geq E_{thresh} \end{cases} \quad (3.7)$$

The actual response for Čerenkov detectors is step, but not a step function. Thus, common practice is to define the threshold energy as the energy where the γ -ray detection per unit energy is at its peak. Another way of expressing this would

be to say that the threshold energy is the energy for which the product of the differential flux spectrum of the source and the effective area of the detector reach a maximum:

$$A_{eff}(E_{thresh}) \times \phi_{diff}(E_{thresh}) = \max_E(A_{eff}(E) \times \phi_{diff}(E)) \quad (3.8)$$

where $A_{eff}(E)$ is the effective area for the detector as a function of energy and $\phi_{diff}(E)$ is the differential emission spectrum for the source in question. This energy is sometimes called the “spectral threshold energy” [75].

In this convention, because the energy threshold depends on the effective area and the effective area in turn depends on the path in the sky of the source observed, the threshold energy is also a source dependent value. The threshold energy is also dependent on the source spectrum when one considers that one has to use the convolution of the effective area with the source’s differential spectrum. For the Crab, this does not pose a serious problem: the Crab’s flux has been measured both below and above the STACEE energy range, so assuming a continuous (experimental) spectrum is well founded. For sources such as ON+231 where the spectral index is poorly understood and the cutoff occurs below Whipple energies, this approximation is more suspect. If one assumes a spectral index of 2.4 [75] for the Crab and performs the convolution with the average Crab effective area for the STACEE telescope [61] one obtains an energy threshold of $\sim 190 \pm 60$ GeV. When the Crab threshold energy calculation is repeated with the trigger model used for this analysis (the trigger models are the only differences in the MC chains for the Crab and ON+231 analysis) we obtain an energy threshold of ~ 160 GeV, which is consistent (within systematic error) with the Crab analysis energy threshold.

For ON+231, using the same method (see figure 3.14), with the previously presented effective area curve and the mean EGRET spectral index of $E^{-1.73}$ [5], we obtain an energy threshold of ~ 130 GeV. To get an idea of how this threshold

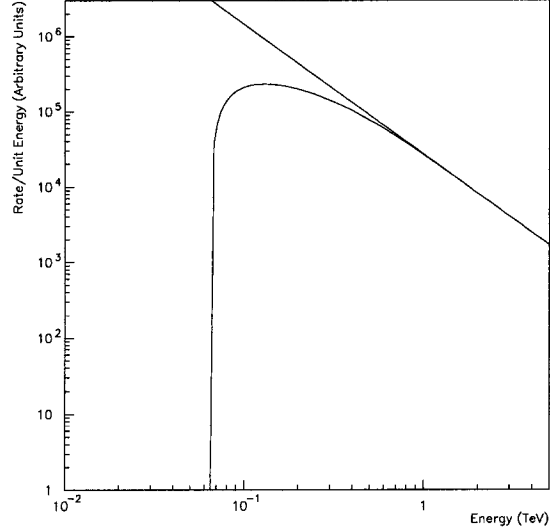


Figure 3.14: The solid curve is a product of the average effective area curve with an $E^{-1.73}$ spectrum. The solid line is the $E^{-1.73}$ spectrum, shown for comparison.

changes with the spectral index we repeated the calculation for values differing by 1σ from the EGRET central value (i.e. for $\Gamma = 1.73 \pm 0.18$ as reported in [5]). We obtain a threshold of ~ 140 GeV for the harder spectrum ($\Gamma = 1.55$) and 120 GeV for the softer spectrum ($\Gamma = 1.91$). When one compares this energy threshold result to that of the Crab one must also take into account the change in elevation angle. The maximum elevation angle of the crab data was taken at 77.1° , the ON+231 data was taken at a higher elevation angle (the majority of the data near 83°). The effect of elevation angle on the effective area curve (discussed in section 3.3.2) is that as the elevation angle increases the turn-on energy of the effective area curve decreases, when even this small decrease in turn on energy is combined with the power law spectrum of the source the spectral energy threshold will decrease. Because of this fact we expect the ON+231 spectral energy threshold to be lower than the Crab spectral energy threshold for an identical instrument.

Chapter 4

Data Analysis

The STACEE-32 prototype was built in the spring and fall of 1998 so that we could observe the Crab for the 1998-99 season. In the fall of 1998 we started an intense observation campaign. Although the Crab Nebula was our primary objective during the campaign, ON+231 presented itself as an ideal secondary candidate since it rises immediately after the Crab sets. Starting on February 14th, 1999 several nights worth of data were taken on ON+231. This resulted in a data set consisting of 17 on-off pairs. The following is a description of the data collection procedure, data analysis techniques and a presentation and discussion of our results.

4.1 Data Collection

Since the cosmic ray flux is much larger than the γ -ray flux, the STACEE-32 data set is largely composed of proton showers. The extraction of a γ -ray signal from this background dominated data can only be accomplished by comparing two data sets, one set of runs acquired while tracking the source (the ON runs)

that presumably include signal, and another set containing only background (OFF runs). The statistical significance of a signal is expressed as:

$$S = \frac{ON - OFF}{\sqrt{ON + OFF}} \quad (4.1)$$

where the ON and OFF variables represent the total number of events taken on and off source respectively. Equation 4.1 is true only if the background rate has remained the same for the ON and OFF runs. The major source of background events in the experiment are the cosmic rays which do not vary significantly in time and are distributed isotropically: therefore one does not expect to see significant variations in cosmic ray rates between any OFF and ON runs. However, there exist some sources of background that can vary from run to run:

weather conditions Compared to the relative darkness of the night sky at Sandia, clouds or even haziness can add a significant amount of brightness, due to reflected light from the city of Albuquerque and lights from the surrounding Kirtland Air Force Base. Clouds have been observed to cause the PMTs to have dangerously high currents. Besides the risk of obtaining more triggers from background light, high L1 rates cause increases in deadtime and have been observed to cause technical problems. For all of these reasons, ON-OFF data with differing weather conditions are excluded from this analysis.

lights around the site There exist many sources of light pollution around the STACEE-32 telescope. Although the chances of observing a variation between runs in the amount of this light are very small, they would have the same effects as clouds, causing the tube currents to rise and the L1 rates to climb. Since man-made light sources are usually much more intense than natural phenomena, these sources usually activate the HV current trip.

technical problems Since this entire data set was recorded using a prototype of the telescope, many technical problems were encountered during the data taking. These problems usually manifest themselves quite clearly in the data and can be easily spotted offline. The data with technical problems were removed from the data set.

4.1.1 A Typical Night at the STACEE Telescope

Observations of sources with the STACEE telescope are limited to clear, moonless nights when the source is within 45 degrees of zenith. A typical evening of observations would start at astronomical twilight, or when the moon sets depending on which was later (these two factors are the main determinants for the STACEE duty cycle). The phototubes are then turned on early to allow them to warm up (tube response stabilises about 1/2 an hour after the HV has been applied) while the heliostats are being initially slewed from their stowed positions. Once the heliostats are at zenith, two rate versus threshold curves are recorded: one using randomised delays and the other using proper delays. A clear breakpoint can be observed in the rate versus threshold curves (recall figure 2.15). The scrambled delay curve will go to a trigger rate of zero while the in-time delay curve tends to flatten. Using these two curves one can easily locate the value of the discriminator threshold at which the experiment triggers on Čerenkov light and is largely free of accidentals due to random coincidences. The discriminator thresholds are then set for the evening. For this data set the discriminator thresholds were typically set at ~ 125 mV with the trigger conditions set at 6/8 (L1) and 3/4 (L2).

Each data run is also taken with a corresponding background run. For the OFF run the same path in azimuth and elevation is observed as for the ON run. To do this one must slew the heliostats to a point 30 minutes in right ascension

(RA) from the source, all the while keeping the declination constant. The runs are 28 minutes in length. The choice of a 30' offset, allows the operator 2 minutes to slew the heliostats to or off the source. Although there can be only one type of ON run, one can choose between two types of OFF runs: OFF-East and OFF-West. When the ON run is observed first in the sequence one would take the OFF run to the east of the source. When the OFF run is observed first, it is to the west of the source. To maximise the amount of data taken close to zenith one would use OFF-West runs as the source is rising and OFF-East runs after the source has transitted. Barring technical problems, this sequence of ON-OFF pairs continues until the moon rises or until the start of astronomical twilight. Figure 4.1 illustrates the sequence of ON-OFF runs that would be taken in an ideal night of observations. Zenith runs are also taken at the beginning, middle and ends of observing nights.

4.2 Analysis Technique

Because the STACEE-32 ON+231 data set was so small, (17 pairs for ON+231 compared with 141 for the Crab Nebula), the analysis for this source was performed with the idea of keeping as much “good” data as possible. Individual run cuts were kept as loose as possible. Instead of cuts on the entire run quantities, runs were divided into one minute bins and all possibly usable data was kept. Adopting this approach led us to keep all weather conditions. For comparison, in the Crab analysis, 6% of the original run pairs were discarded due to bad weather conditions[61]. An additional 22% of the Crab runs were discarded due to variations in L1 rates, usually as a direct consequence of cloud cover or haze moving into the telescope’s field of view.

Because we perform an ON-OFF comparison, it is very important that the

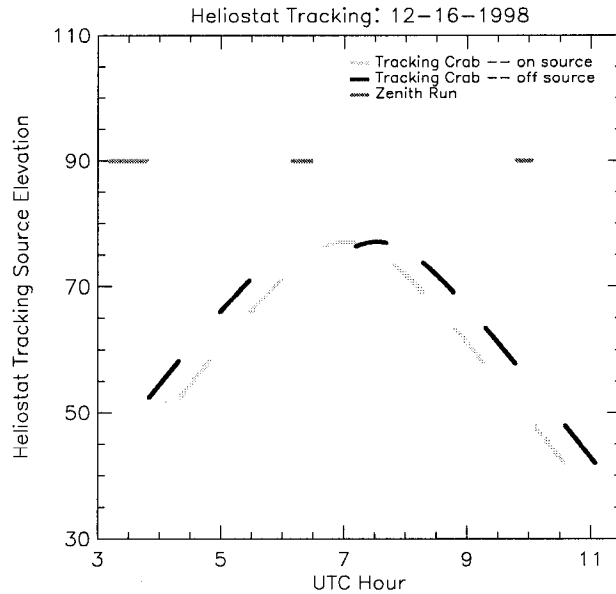


Figure 4.1: A good night of ON OFF pairs with the STACEE telescope. Here the elevation of the STACEE target is plotted as a function of UT time. The straight lines at at 90° elevation are zenith runs used for stability and diagnostic tests. Note that the ON and OFF runs have the same elevation path, offset in time.

ON-OFF data be matched to the same lengths of time. To do this the run lengths were trimmed so that the starts and ends of the runs were exactly 30 minutes apart. This procedure was complicated by certain technical difficulties. STACEE-32 was a development version of the telescope and was beset by occasional problems with the DAQ. A certain pathology of the DAQ, essentially due to a CAMAC controller problem that occurred in high L1 rate situations, came to be known as a “DAQ hang”. In this case the electronics would keep functioning but data would no longer be recorded. Run pairs where DAQ hangs occurred were kept, but only the parts of the runs that had data corresponding to the same trajectory of the source in local coordinates of the OFF and ON runs were used

in the analysis. These cuts are referred to as the fiducial time cuts.

4.2.1 Run Cuts

Cuts based on general run characteristics that exclude entire runs from the analysis, such as cuts based on weather conditions or technical problems, were avoided because they tend to discard entire runs even though only parts of the run experience problems. This tactic is much more painstaking and time consuming than simply discarding entire runs, but is also essential considering the limited size of the data set. Runs displaying technical problems (such as the DAQ hang problem) were only truncated, keeping as much of the unaffected data as possible. The only cut that could be considered a run cut, was a cut on the run length: runs had to contain at least 5 minutes worth of steady conditions after the various time dependent cuts, in each of the ON and OFF runs.

4.2.2 L1 Rate Cuts

High PMT rates, and therefore high Level 1 rates also, can seriously degrade the quality of data taken. They degrade the quality of the data in two ways: they increase the deadtime of the trigger system and they increase the number of accidental triggers in the data. The STACEE-32 L2 trigger system is not a deadtime-free system. The delayed channel is effectively dead for a time approximately equal to the delay setting. As long as the delay setting is small compared to the time between L1 triggers this effect is negligible. As the time between L1 triggers decreases (the L1 rate increases), this deadtime worsens.

As PMT rates increase, the rate of corruption of the data due to accidental triggers increases strongly. Ideally we would use data for which accidental rates

are negligibly small.

To ensure stability between the runs, various quantities from the runs were plotted as a function of time (currents, L1 rates, L2 rate) in one minute bins. Cuts were then imposed on a time-dependent basis. The most telling of these parameters were the L1 rates.

The L1 rates are almost entirely due to PMT coincidences and as such are a good measure of the local sky conditions at any time. One can model the L1 rates using individual PMT rates to show this. This model is initially easier to understand if we assume that all tubes fire at the same rate R_t . The L1 coincidence rates would then be described by:

$$R_{L1} = n \binom{n}{m} R_t (R_t \tau)^{-1} \quad (4.2)$$

where τ is the trigger formation time and m and n are the trigger conditions for the formation of the L1 trigger, and $\binom{n}{m}$ is the number of different combinations where we can choose m channels to form a trigger from a total number of n channels.

$$\binom{n}{m} = \frac{n!}{m!(n-m)!} \quad (4.3)$$

In our case $m = 6$ and $n = 8$. This approximation only holds true if $R\tau \ll 1$. Equation 4.2 can predict the shape of the L1 rate distribution with time, but fails to predict the right absolute values. By making $R\tau$ small one can make the random coincidence background rate small. However, values of τ smaller than the width of the Čerenkov pulse, as discussed in section 1.2.3, will result in a loss of signal. In STACEE-32 the value of τ was governed by the discriminator pulse width of ~ 13 nsec.

To achieve a more robust understanding of the L1 rates one must take into account actual PMT rates. Starting from first principles we can refine our rate model to take into account different individual tube rates. We do this numerically,

by assuming that one tube has fired and then calculate the probability that at least $m - 1$ tubes trigger within a length of time τ , (in our case τ is equivalent to the effective pulse width), where m is the minimum number of tubes needed for the trigger condition. For identical tube rates, R , and a 6/8 trigger condition, the L1 rate is:

$$\begin{aligned}
 R_{L1} &= 8 \times R \times \binom{7}{5} \times P(R, \tau)^5 \times \bar{P}(R, \tau)^2 \\
 &+ 8 \times R \times \binom{7}{6} \times P(R, \tau)^6 \times \bar{P}(R, \tau) \\
 &+ 8 \times R \times P(R, \tau)^7
 \end{aligned} \tag{4.4}$$

where the overall factor of 8 arises because there are eight identical tubes. We have included the probability of not getting hits within a time τ , $\bar{P}(R, \tau)$.

For a randomly firing PMT the probability of getting another hit within a time τ is [76]:

$$P(t < \tau) = \int_{t=0}^{t=\tau} R e^{-Rt} dt = 1 - e^{-R\tau} \tag{4.5}$$

Thus it follows that $\bar{P}(R, \tau)$ is simply $e^{-R\tau}$. To make the model sensitive to individual PMT rate variations we must substitute the $\binom{n}{m}$ with the actual permutations needed. Thus equation 4.4 becomes:

$$\begin{aligned}
 R_{L1} &= R_1[P_2P_3P_4P_5P_6\bar{P}_7\bar{P}_8 + 20 \text{ more terms where we change the } \bar{P}'\text{s excluding } P_1] \\
 &+ R_2[P_1P_3P_4P_5P_6\bar{P}_7\bar{P}_8 + 20 \text{ more terms where we change the } \bar{P}'\text{s excluding } P_2] \\
 &+ R_3[5 \text{ of } 7] + \dots + R_8[5 \text{ of } 7] \\
 &+ R_1[P_2P_3P_4P_5P_6P_7\bar{P}_8 + 6 \text{ more terms where we change the } \bar{P}'\text{s excluding } P_1] \\
 &+ R_2[6 \text{ of } 7] + \dots R_8[6 \text{ of } 7] \\
 &+ R_1[P_2P_3P_4P_5P_6P_7P_8] + R_2[7 \text{ of } 7] + \dots + R_8[7 \text{ of } 7]
 \end{aligned} \tag{4.6}$$

where the notation [5 of 7] represents the 21 $\binom{7}{5} = 21$, $\binom{7}{6} = 7$ different terms

one needs to add. Using this model one can verify that the L1 rates are completely dependent on the PMT rates, which are in turn almost entirely consisting of night sky background random coincidences. Thus L1 rates are a good measure of the night sky background variations. Figure 4.2 shows that the model matches data very well. Assuming a trigger formation time that is the width of our discriminator pulse width (13.5 nsec) and taking the first 8 tube rates averaged over one minute one can predict the L1 rates accurately. The effective L1 coincidence formation time obtained from this model is also useful for the trigger model described in the simulation chapter.

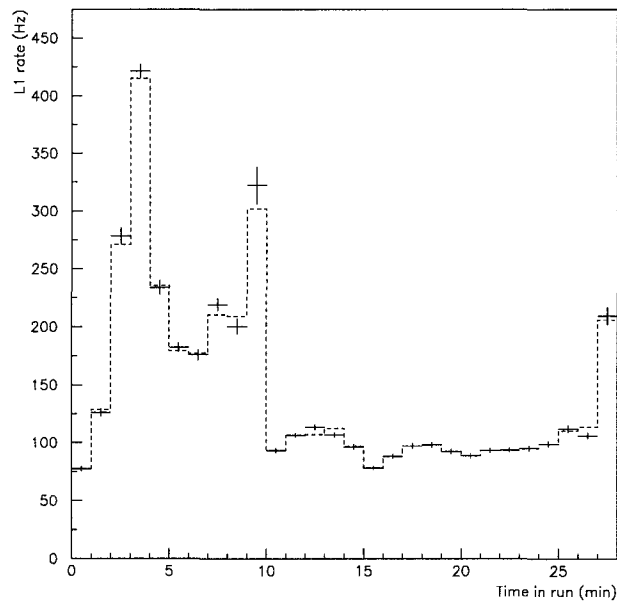


Figure 4.2: The L1 rate model is compared to the L1 rate for the first cluster (channels 0 through 7) of run 1244. The points are actual data (error is statistical) and the histogram is the rate model prediction from PMT rates averaged over one minute bins.

Since we can now see that L1 rates vary strongly as a function of night sky background we can use these rates to impose cuts within runs. If L1 rates change significantly between an OFF and an ON run one can surmise that the night sky background has changed between the two sections of runs and that these sections of runs should be cut from the analysis. The cut designed to do this looks at the ratio (taken in 1 minute bins) between the first and second run in a pair, irrespective of whether the run be an OFF or an ON run.

$$0.5 < \frac{L1P_{n_{first}}}{L1P_{n_{second}}} < 2 \quad (4.7)$$

$L1P_n$ refers to one of the four clusters. If at least two clusters show inter-run L1 rates that vary by a factor of two then those sections of runs are removed from the data set, see figure 4.3.

4.2.3 Cuts Due to Technical Problems

A number of runs (8 in total) from the ON+231 data set were affected by unexplained fluctuations in L1 rates. These fluctuations were not large enough to make those sections of runs fail the L1 rate ratio cut. The fluctuations were of the order of 10-20%. The fluctuations only occur on the last L1 patch, (channels 24-31). The fluctuations observed do not seem to cause a corresponding change in the L2 trigger rate. Figure 4.4 shows the L1 rates of run 1322 with the problem occurring in the last cluster. When these 8 runs were investigated further it was found that the fluctuations all occurred when the LRS 4518 delay module had a transition in its delay setting. More specifically, the L1 rate fluctuations were linked to the last channel, channel 31. The corresponding discriminator channel had also been suspected of double pulsing [77]. For these reasons the sections of runs that display this problem have been removed from the data set. One pair (runs 1273-74) was completely removed because of this cut.

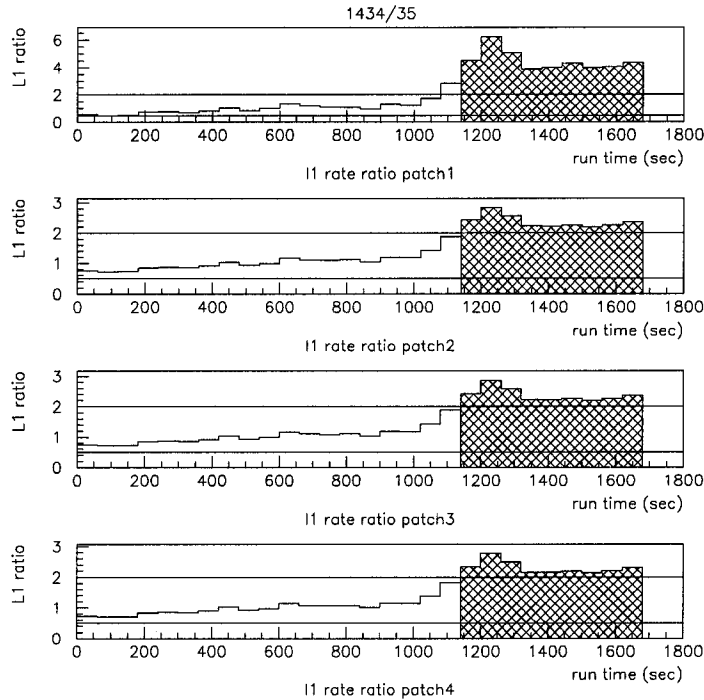


Figure 4.3: Ratio of the four L1 rates as a function of time for runs 1434 and 1435. The two horizontal lines show the upper and lower bounds (2 and 0.5) of the L1 rate ratio cut. In this pair, all events after 1150 seconds have been cut.

4.2.4 Event Cuts: Offline Reconstruction of Events

In their raw form, STACEE-32 data are nothing more than time-stamped TDC and ADC measurements stored on a channel by channel basis. When the TDC hits are plotted versus time in the run, concentrated bands are apparent where the in-time hits due to the Čerenkov events occur. The TDCs are operated in common stop mode, so higher TDC values correspond to earlier times (time is measured in TDC counts from the common stop signal). The position and slope of these bands is a consequence of the delays used in the trigger system. As the source tracks its path through the sky, the delays used to form the trigger are

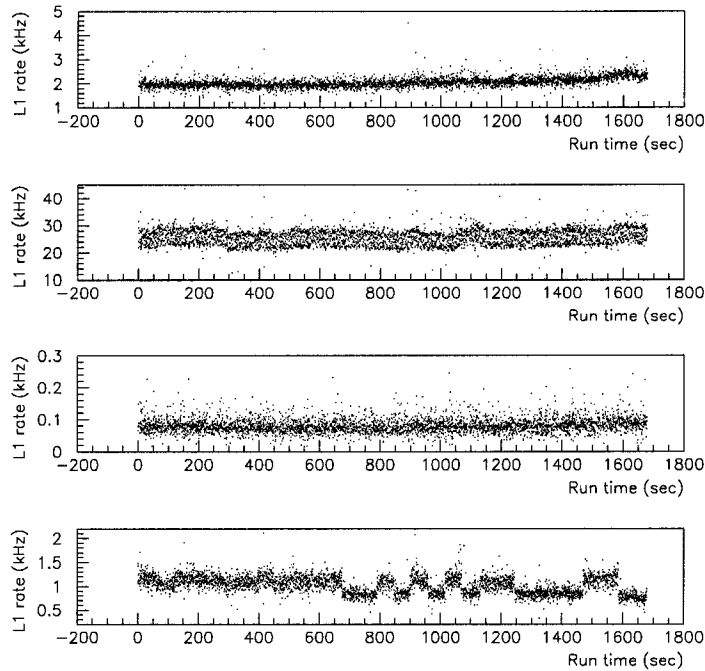


Figure 4.4: Run 1322 exhibiting the “choppiness” malfunction on the last cluster for about 2/3 of the run. The effect is visible as the L1 rate changes dramatically in a non-statistical fashion. In this pair all data after 670 seconds were removed from both the ON and OFF runs.

dynamically adjusted and result in a slanted TDC versus time distribution.

Straight lines are fit to these bands and only TDC hits within ± 12 TDC hits (± 6 nsec)) from the fitted line are accepted. If a channel has a TDC hit within the time band, the channel is said to have an “in-time” hit, and is considered to have participated in the event. Figure 4.5 shows the narrow band that is present in the TDC versus time plots and the residuals to a straight line fit to the TDC distribution. To reconstruct the entire event one must proceed cluster by cluster and test for in time hits in every channel in the experiment. If enough channels

in a cluster are in-time and at least 3 clusters have triggered, the event is said to be an offline trigger (OT) event.

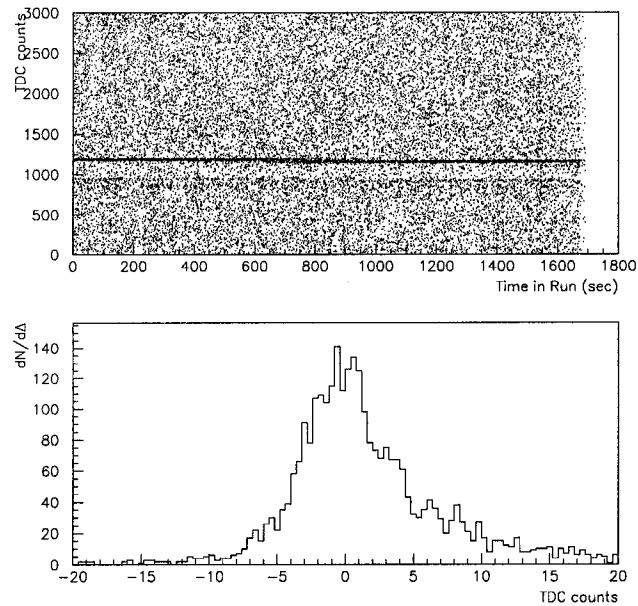


Figure 4.5: Top: raw TDC hits for a channel plotted as a function of time. The slope in the band is due to the movement of the object through the sky. The second line below the first line is a reflection of the signal pulse (up and down a 20 m long cable) due to improper impedance matching at the filter box. Bottom: residuals from the fit of a straight line to the upper dark band. One can observe immediately that a TDC cut at ± 12 TDC hits accepts the vast majority of the data.

4.2.4.1 Transit Runs

After a source transits, it starts to decrease in elevation angle. One therefore expects a slope change in the graph of TDC hits as a function of time (see figure

4.6). Since a straight line can not be fitted to such data, the data are split into two runs and are simply fitted on each side of the transit point independently. This only occurs once in the ON+231 data set, for the run pair 1318-19. The resulting 2 runs are labelled 1318a and 1319a for the first sections of the ON and OFF runs and 1318b and 1319b for the latter two.

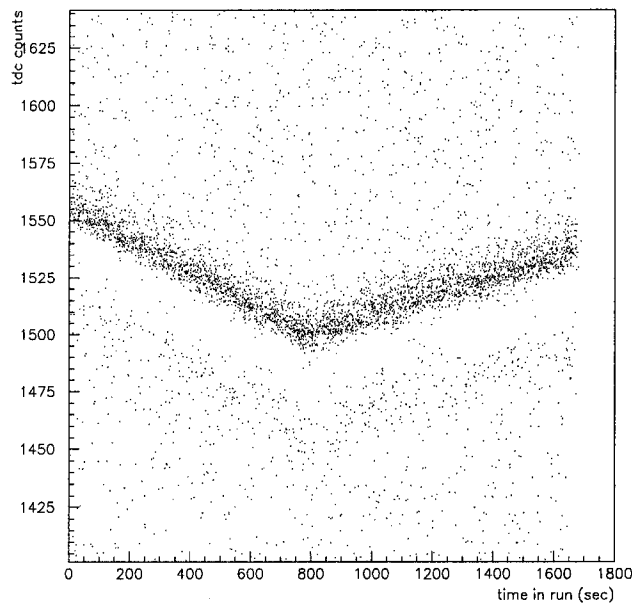


Figure 4.6: Example of a TDC distribution where the source transits during the run. The blank area below the dark band is present in all STACEE-32 TDC distributions and is due to the discriminator deadtime.

4.2.5 Deadtime

As mentioned in section 2.2.5.3 the 10 kHz clock has two outputs to an LRS 2551 scaler. One stays on for the entire duration of the run while the other is gated by the event veto while the DAQ is processing a triggered event. By taking the ratios

of these two clocks, the experiment's livetime can be calculated. The livetime is measured over the fiducial time of the run and a deadtime correction is calculated on a run by run basis. Once this correction has been applied to the total number of events reconstructed for that run, the new event total is referred to as deadtime corrected (DC). For the runs used in the ON+231 analysis the livetime was $\sim 90\%$ (see figure 4.7).

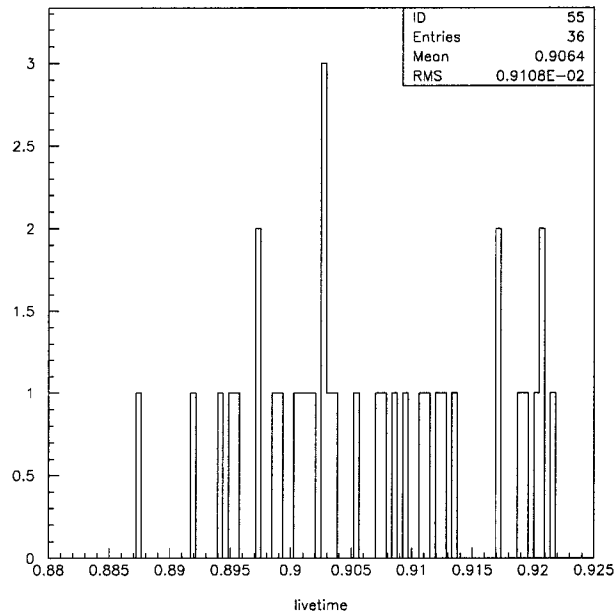


Figure 4.7: The livetime for the runs used in the ON+231 analysis. The deadtime correction is of the order of 10%.

4.2.6 Timing Corrections and Heliostat Arrival Times

Since we know the channel by channel delays in the electronics and the positions of secondaries and heliostats we can calculate the direction of the incoming wavefront from the timing information. The times of flight are determined from the

geometrical distances between the centres of each heliostat and the position of the secondaries. The x, y and z positions of each heliostat and secondary were measured to an accuracy of 1 cm.

The trims, slight channel to channel variations in the signal transit time through the electronics, were measured using two different methods. The first method employed the calibration laser. The camera was illuminated with laser flashes and the PMT pulses' travel times through the cables and front end electronics were then measured channel by channel at the 200' level to better than 0.5 nsec using a digital oscilloscope. The second method was to use a lens cap mounted with an LED to pulse tubes individually.

Using all these time corrections one can reconstruct the shower arrival times at the heliostats, and knowing the speed of light, essentially obtain a snapshot of the shower as it triggered the experiment, see figure 4.8. These arrival times are then used with quality cuts to reject cosmic ray showers that have triggered the experiment.

4.2.6.1 Slewing correction

Timing variations due to differences in pulse amplitude can vary by as much as 3 nsec. Since we are trying to measure a wavefront that is only 5 nsec thick, a variation of this magnitude must be corrected. A slewing correction is therefore also applied to the 24 channels that are equipped with ADCs. To correct for this effect one needs to have pulse amplitude information. To determine the slewing correction every channel was illuminated using the laser. The laser flash amplitude was then varied and time and amplitude of each pulse were then recorded. Figure 4.9 is a typical slewing plot (plot of the arrival times as a function of pulse amplitude). A good parameterisation of the slewing correction is [61]:

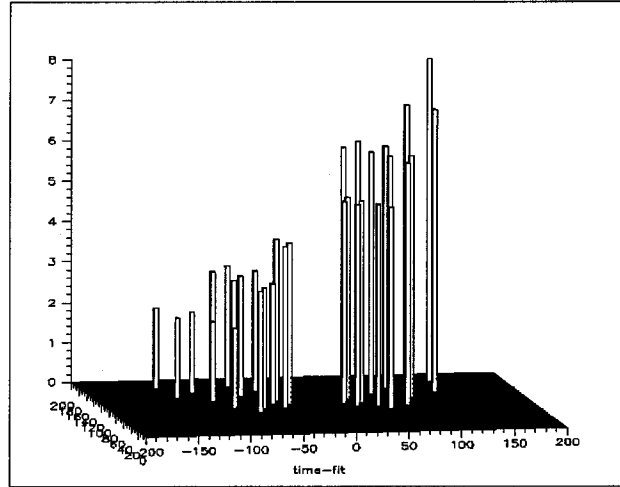


Figure 4.8: Arrival times (in nsec) reconstructed from the time of flight values for an 11 km radius sphere hitting the centre of the array. The position of these columns correspond to the position (in metres) of the associated heliostats in the field.

$$\delta t_i = \frac{A_i}{B_i + (Q_{counts} - \langle Pedestal_i \rangle)} \quad (4.8)$$

Here A and B are constants determined empirically for each channel. Q_{counts} is the number of raw ADC counts, and $\langle Pedestal_i \rangle$ is the pedestal. This slewing correction is applied to the 24 channels equipped with ADCs.

4.2.7 Wavefront Reconstruction

Once the trigger has been re-imposed and the wavefront arrival times for each channel that has an in-time hit is determined, one can use the heliostat positions

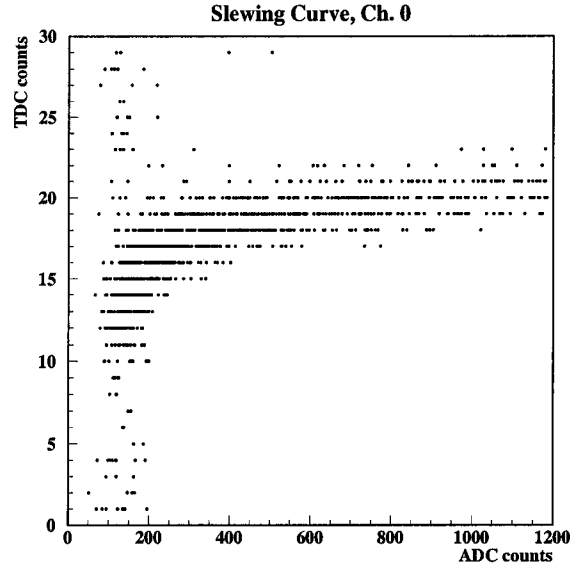


Figure 4.9: Pulse slewing for channel 0. The Y axis is the arrival time in TDC counts (0.5 nsec) in common stop mode (the smaller values represent later arrival times). The X axis is in raw ADC counts.

to recreate a 3 dimensional snapshot of the shower front as it triggered the experiment. MC studies tell us that γ -initiated showers have a more spherical wavefront than their proton-initiated counterparts. As a means to determine the “sphericity” of an event we calculate the goodness of fit parameter, χ^2 , that results by fitting the shower front to a sphere. To obtain this value one must minimise the equation:

$$\chi^2 = \sum_i \frac{(t_i - t_{eqn})^2}{\sigma_i^2} \quad (4.9)$$

Here t_i are the reconstructed heliostat arrival times for the channels in the fit, t_{eqn} are the times one would obtain with a given equation (usually a sphere or a plane). The parameters to be minimised are embedded in the equation we want to test. $1/\sigma_i$ is the weight associated with the measurement of t_i , usually this is simply the timing resolution we have for that channel. We can see quite easily

that the value of χ^2 depends inversely on this weight so accurate determinations of the timing resolution are very important in determining what range of values we expect to see in a χ^2 distribution.

4.2.7.1 Timing Resolutions

In order to perform a χ^2 minimisation one must have weights, or timing resolutions. It has been observed that high levels of night sky background degrade the timing resolution. This occurs as night sky background pulses are combined with actual Čerenkov pulses and change the pulses' shapes and widths, therefore changing the measured arrival time of these pulses. If we assume that the arrival times of the night sky background photons are random, then the timing resolution would vary with the square root of the individual tube rate (since we believe these rates to be completely dominated by night sky background). We parameterise the tube to tube time resolutions as:

$$\sigma_{ci} = \sigma_{0i} \sqrt{1 + \frac{R_i}{R_{0i}}} \quad (4.10)$$

where σ_{ci} is the value of the timing resolution, R_i is the measured PMT rate for channel i , σ_{0i} and R_{0i} are constants determined empirically from calibration runs. The timing resolutions were obtained by taking several zenith runs at different discriminator threshold values (i.e. at different PMT rates) and then fitting these events to spheres. The residuals of these fits are in turn fitted to Gaussians and the width of the Gaussians are taken as the σ 's for that threshold setting [61]. In this manner the timing resolution is determined as a function of PMT rate for each tube. Equation 4.10 can then be used to interpolate in order to determine σ_{ci} for a particular channel and an instantaneous rate R_i . Figure 4.10 demonstrates how well the parameterisation fits the timing resolutions measured at different PMT rates.

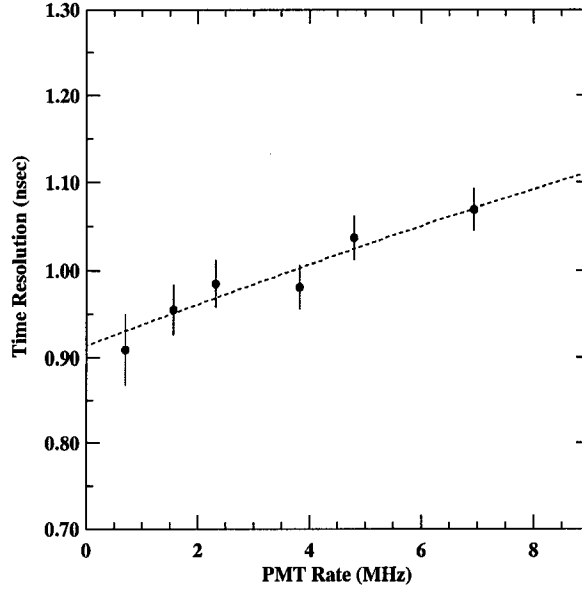


Figure 4.10: Timing resolution in nsec plotted as a function of PMT rate for one channel. Points are the time resolutions; the dotted line is the parameterisation from equation 4.10.

4.2.7.2 Fitting Showerfronts to a plane

To illustrate the general idea of how we fit the timing data, I will describe how we initially fit the reconstructed timing data to a plane, and extract the right ascension and declination. If one treats the arriving shower as a plane one can perform an exact χ^2 minimisation to determine the parameters a, b, c_p in the equation of a plane, namely:

$$z = ax + by + c_p \quad (4.11)$$

Once one has fitted for a, b and c_p , one can obtain the direction of the shower by looking at the vector normal to that plane, namely $\hat{n} = (-a\hat{i}, -b\hat{j}, \hat{k})/\sqrt{a^2 + b^2 + 1}$. This vector points in the direction of the incoming shower front. We will call this vector the direction vector. From this vector one can calculate the local azimuth

and zenith angles ϕ_{az} and θ_{zen} :

$$\phi_{az} = \tan^{-1}(b/a) \quad (4.12)$$

$$\theta_{zen} = \tan^{-1}(\sqrt{a^2 + b^2}) \quad (4.13)$$

These equations describe how to obtain the ϕ_{az} and θ_{zen} angles using the z positions. We must keep in mind that we are actually using propagation times to the shower front at the time of the trigger and not z positions, since the STACEE-32 detector only allows us to get the arrival times. To use the arrival times we need to perform the transformation $z' = ct/\cos\theta$, where c is the speed of light, and t is the arrival time. When we perform the $z \rightarrow z'$ transformation the azimuth and zenith angle formula become:

$$\phi_{az} = \tan^{-1}(b/a) \quad (4.14)$$

$$\theta_{zen} = \sin^{-1}(\sqrt{a^2 + b^2}) \quad (4.15)$$

Then, using the GPS timestamp, one can reconstruct the right ascension and declination of that specific event. The crucial step in this process was obtaining the direction vector of the wavefront from fitting to the plane. Once this has been obtained the transformations for obtaining ϕ_{az} , θ_{el} , the right ascension and the declination are straightforward.

4.2.8 Fitting Showerfronts to a Sphere

At lower energies γ -initiated showers can be approximated as spheres with large (≈ 11 km) radii. Since the shower maximum position of the shower is the region where most secondaries (and therefore Čerenkov photons) are generated, it is logical to take this point as the point of origin of the spherical wavefront. The height of the shower maximum is fixed in the sense that it occurs on average at an atmospheric depth of ~ 270 g/cm² (100 GeV γ -ray), as measured along the path of

the incoming particle. Of course the distance from shower maximum to the centre of the array, the radius of the sphere we want to fit, will be a function of $\cos \theta_{el}$ since as the shower enters the atmosphere at an angle that is not perpendicular to the Earth's surface, it will traverse more atmosphere at a lower altitudes. The z coordinate of the shower maximum position is then given by:

$$H_z = 7000 \ln\left(\frac{1300}{|270n_z| - 0.6}\right) \text{metres} \quad (4.16)$$

where H_z is the height of shower maximum, in metres above sea level, and n_z is the z -component of the showerfront's wave vector [61]. The constants in this equation are artifacts of the conversion from atmospheric depth in (g/cm^2) to altitude above sea level. Figure 4.11 is a simplified 2 dimensional diagram that illustrates the geometry of the spherical shower front arriving at the heliostat field.

With the height of the point of origin fixed, one only has to vary the x and y values of this point in the χ^2 minimisation to determine one end of the direction vector. The position of the vector on the ground is assumed to be the geometric centre of the array. This is done because of a lack of sufficient channels with ADC data and because of the limits to the physical size of the experiment. Since γ -ray showers have a nearly uniform photon density and are so wide (they often cover the entire size of the array) one would need to detect the edges of the Čerenkov pool to be able to accurately locate its centre. The configuration of heliostats in STACEE-32 did not allow for enough heliostats at the edges to do this.

The lack of good ADC data prevents us from locating the shower core centre on the ground as a function of collected charge for each PMT or conversely, photons on each heliostat. MC simulations show that taking the shower core location as the geometrical centre of the array is not a bad approximation, since the experiment is most sensitive for showers landing within 50 m of the centre of the array [61]. With an error of 50 m on the ground, one can estimate the angular error by dividing this value by the approximate radius of the showerfront, which is usually

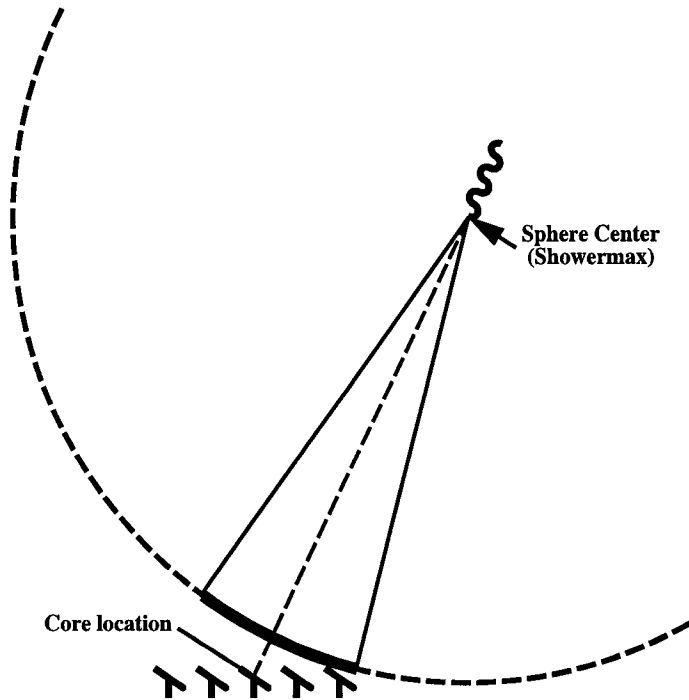


Figure 4.11: A schematic representation of the spherical wavefront fitting. The shower core location is fixed at the centre of the array, while the centre of the sphere is defined as the shower maximum of the shower. The wavefront should not be confused with being isotropic: it is conical with a spherical base, as demonstrated in this diagram.

≈ 11 km, to obtain an angular resolution of $\approx 0.25^\circ$.

Thus, with both ends of the line determined, the direction vector of the shower can be calculated. This information can be converted to local elevation and azimuth angles and then to right ascension and declination. Figure 4.12 is a plot of the reconstructed right ascension and declination for every event in run 1271.

The actual fitting was done numerically using the Numerical Recipes fitting routine called amoeba [78]. The fit was performed iteratively. It is performed first on all channels that have reconstructed in-time hits for those channels that have

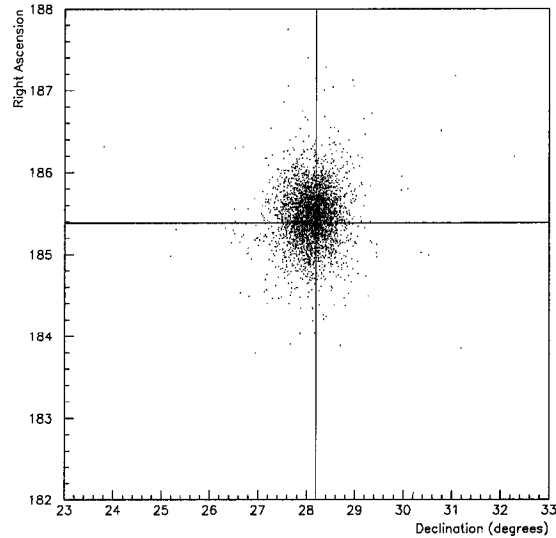


Figure 4.12: The reconstructed right ascension and declination for every event in run 1271. The cross hairs indicate the actual coordinates for ON+231(RA=12h21m31.7s DEC=28d13m59s) or (RA=185.38° DEC=28.23°).

slewing corrections (24 out of 32). After the first iteration, any channels that are more than 4σ away from the fit are removed. The remaining channels are then re-fit; any channel with a 4.5σ deviation from the fit is then removed and one final fit is performed. It was the χ^2 per degree of freedom from this final fit that is saved.

4.2.9 χ^2_{sphere} Cut

For every γ -ray, traversing a given solid angle, there are of the order of 10^4 protons. Because of this large background rate, and despite our trigger's insensitivity to hadron-initiated showers (as evidenced by our low proton trigger rate calculated in section 3.3.1) we must impose quality cuts offline to improve the purity

of our sample. If one can find a cut that improves the purity of our sample the sensitivity of the experiment will effectively be increased. If a very effective offline proton removal method could be found, our experiment could operate at lower thresholds. Sadly this is not the case with STACEE-32 or any other non-imaging Čerenkov experiment at present. The protons that do trigger our experiment leave a signature that is very much like the relatively rare γ rays we are looking for. The fact that our data is mostly protons is reflected in the χ^2 distributions for the on and off data (Figure 4.13). These two distributions are virtually identical. The similarity of these two distributions assures us that the χ^2 cut will not preferentially effect the on or off data.

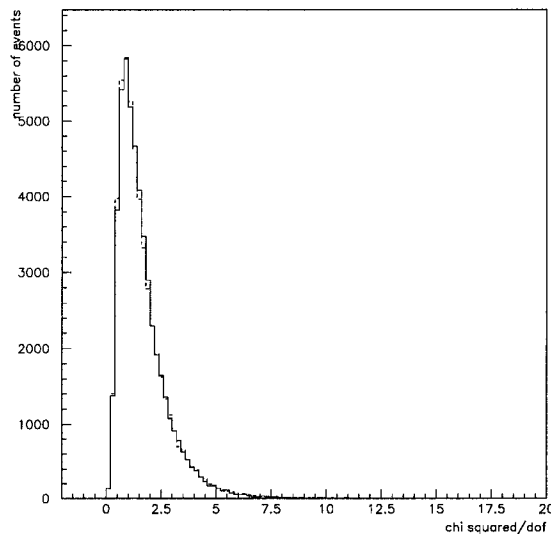


Figure 4.13: Superimposition of χ^2 distributions for the STACEE-32 ON+231 ON and OFF data. The dashed line is the OFF data.

One of the few handles we have on rejecting protons offline is the χ^2 value resulting from a fit to a spherical wavefront. In the MC section we have seen that proton-initiated showers tend to be less dense (in Čerenkov photons/area) than

γ -initiated showers, but we also know that their timing profiles are less smooth than for γ -initiated showers. If proton-initiated showers indeed have a different timing profile one should be able to observe a difference in the χ^2 distributions of the spherical wavefront for γ rays and protons. S. Oser proposed a χ^2 cut in his thesis for the analysis of the STACEE-32 Crab data [61]. When one looks at these distributions using MC data, (see figure 4.14) one notices that at $\chi^2 < 1$ the γ -ray peak is mostly conserved while the proton data lies primarily in the $\chi^2 > 1$ region.

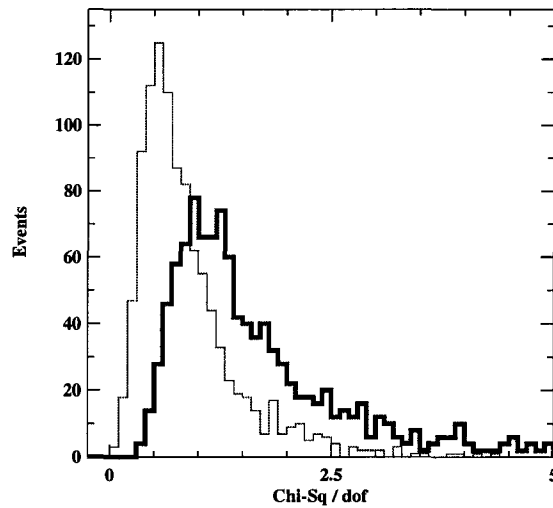


Figure 4.14: The χ^2 (dof) distributions for simulated 100 GeV γ -ray (light line) and proton (heavy line to the right) initiated showers. At $\chi^2 < 1$ the proton contamination in the γ -ray sample is reduced.

4.2.9.1 Efficiency of the χ^2 cut

When the arrival times are fitted to spherical wavefronts one can obtain a χ^2 value from the fit. Thus one can evaluate a shower's resemblance to a γ -initiated shower, by imposing a χ^2 quality cut on a shower by shower basis. One of the issues with this kind of cut with our dataset is how the efficiency of the χ^2 distribution varies with energy. The results from the trigger model summarised in table 3.2 show some variation with energy. If one takes the values of $R_{\chi^2 < 1.0}$ for the 5 nsec individual tube trigger formation time, an increase of the $R_{\chi^2 < 1.0}$ value with energy from $R_{\chi^2 < 1.0} = 0.38$ to $R_{\chi^2 < 1.0} = 0.44$ is observed. To determine whether or not we can use a constant χ^2 cut efficiency over several energies we have to test both cases: namely a constant efficiency for the cut in χ^2 versus a χ^2 cut efficiency value that slides linearly with energy.

For the constant efficiency we take the value of $R_{\chi^2 < 1.0}$ at 200 GeV from table 3.2, namely $R_{\chi^2 < 1.0} = 0.42$. Taking the three values of the $R_{\chi^2 < 1.0}$ from table 3.2, we can form a linear function of energy, $\chi_{eff}^2(E)$, to represent the case where the efficiency of the cut is not constant.

In order to evaluate the effect of a varying χ^2 cut efficiency on the acceptance we compare a quantity, ξ , proportional to the integrated flux one would see between 100 GeV and 1 TeV, for the constant and linearly varying cases. In the case of varying efficiency ξ is proportional to the integral of the EGRET ON+231 differential emission spectrum of the source multiplied by the effective area of the telescope and the χ^2 efficiency function

$$\xi_{linear} = \int_{0.1TeV}^{1.0TeV} \phi(E) A_{eff}(E) \chi_{eff}^2(E) dE \quad (4.17)$$

while for the constant χ^2 efficiency ξ is simply:

$$\xi_{constant} = R_{\chi^2 < 1.0, 200GeV} \times \int_{0.1TeV}^{1.0TeV} \phi(E) A_{eff}(E) dE \quad (4.18)$$

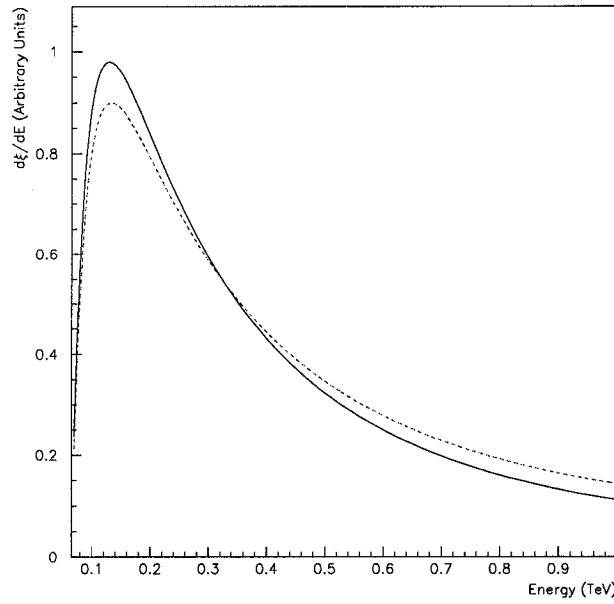


Figure 4.15: The dotted red line is the product of the effective area curve, the differential emission spectrum for ON+231 and the χ^2 efficiency as a function of energy. The solid line is the same product using the constant χ^2 efficiency. The constant χ^2 efficiency used was the value of the 200 GeV $\chi^2 < 1.0$, namely 0.42. When both these curves are integrated the fractional difference between ξ_{linear} and $\xi_{constant}$ is 1.9%.

When one evaluates the integrals, one finds that there is only a 1.9% fractional difference between ξ_{linear} and $\xi_{constant}$, see figure 4.15. Therefore assuming a constant efficiency for the χ^2 cut of $R_{\chi^2 < 1.0, 200 GeV}$ is a reasonable approximation.

Chapter 5

Results and Conclusion

5.1 Results

For this analysis we will compare 4 different stages of cuts. First we will present the data without the L1 rate cuts, the “choppiness” cut or the χ^2_{sphere} cut. The initial modifications at this stage are:

Fiducial Time Cuts: FTC OFF and ON runs are trimmed so that they have equal times and, more importantly, to cover the same tracks of sky. This includes cutting runs into parts for transit runs and cutting the paired run of a DAQ-hanged-run to the same length.

Offline Trigger Re-imposition: OT In time hits are located in the TDC distributions and the trigger is re-imposed offline as described in section 4.2.4.

Deadtime Corrections: DC The livetime is determined on a run by run basis from noting the vetoed and unvetoed 10kHz clocks. The number of events reconstructed for the run is divided by the livetime to give the deadtime-corrected total.

The total time on the source after imposing run length matching (fiducial time cuts) was 25770 seconds. Out of 17 pairs initially considered, 14 showed an excess in the ON run after imposing fiducial time cuts FTC, taking out the fake triggers, re-imposing the trigger offline and correcting for deadtime. Summing all the events and calculating the significance from these different stages gives the results summarised in table 5.1).

Cuts			Events	Events	S
FTC	OT	DC	ON	OFF	σ
✓			55064	54962	0.31
✓	✓		53550	53259	0.89
✓	✓	✓	59174	58754	1.22

Table 5.1: S is the ON-OFF significance $S = \frac{ON-OFF}{\sqrt{ON+OFF}}$. FTC = within fiducial time cuts, OT = offline trigger re-imposed, DC = deadtime corrected.

Once the L1 rate cuts were applied 2 pairs (1244-45 and 1258-59) were completely removed from the data set. At this point 12 out of 15 pairs showed an excess in the ON runs. When the technical problems discussed in section 4.2.3 were removed, one more run pair was cut completely from the data set (1273-74). At this point in the analysis, 11 out of 14 pairs showed an excess on the ON runs. These results are tabulated in table 5.2.

With these additional cuts applied, one can observe that the slight excess of events in the ON runs seems to increase, even though at this point one could not make any statements about observing a signal. When the $\chi^2 < 1$ quality cut is imposed the slight excess in the ON runs disappears.

Cuts				Events	Events	S
FTC	OT	DC	$\chi^2 < 1$	ON	OFF	σ
✓				41584	41265	1.11
✓	✓			40464	40175	1.02
✓	✓	✓		44710	44302	1.37
✓	✓	✓	✓	18741	18749	-0.03

Table 5.2: ON+231 data set significance with the quality cuts imposed. We observe a slight increase in the significance in all stages of the event reconstruction with the L1 rate ratio cut and the cut on the “choppiness”. When the $\chi^2 < 1$ cut is applied, the slight excess on the on runs is wiped out.

5.1.1 Calculating an Upper Limit

With a significance consistent with zero, one would be tempted to conclude that STACEE-32 has not observed a γ -ray signal from ON+231. However to quantify such a claim we must determine how sure we are that we did not see a signal, even a small one, taking into account our background levels and sensitivity. That is, we must construct an upper limit (UL) for the observed γ trigger rate. To construct such an upper limit we employ the Particle Data Group’s (PDG) bounded upper limit method [79]. This method was preferred over the more recent “unified frequentist approach” [80] mostly because of its familiarity to the McGill STACEE group and because at high background levels these two methods become identical. The PDG method involves re-normalising the likelihood curve so that the integral over the physical region is 1.0, for an upper limit this corresponds to the requirement that:

$$\int_0^{\infty} G(x; \mu; \sigma^2) dx = 1 \quad (5.1)$$

where $G(x; \mu; \sigma)$ is the Gaussian distribution of mean μ and σ^2 is variance. Negative fluxes are non physical, so we must bound the likelihood curve at zero. The

upper limit is then defined as the upper bound δ_{UL} of the normalised integral of the likelihood distribution (integrating from zero to δ_{UL}) that is equal to α , the confidence level (CL) wanted. In our case $\alpha = 0.95$ (a 95% CL upper limit).

$$\alpha = \frac{\int_0^{\delta_{UL}} G(x; \mu; \sigma^2) dx}{\int_0^{\infty} G(x; \mu; \sigma^2) dx} \quad (5.2)$$

In equation 5.2, we set α to 95%, μ is our deficit, -8 and σ is the variance namely $\sqrt{ON + OFF} = 193.6$. To evaluate the 95% CL UL, we must evaluate the integrals and solve for δ_{UL} . Knowing the value of the definite integral of the likelihood distribution from $-\infty$ to any value:

$$\int_{-\infty}^a \frac{1}{\sqrt{2\pi}} e^{-\frac{(x-\mu)^2}{2\sigma^2}} dx = \frac{1}{2} [1 + \text{erf}(\frac{a-\mu}{\sqrt{2}\sigma})] \quad (5.3)$$

We can evaluate the integrals from equation 5.2 in terms of 5.3. We then evaluate the error functions (and one inverse error function) to arrive at a value of 376 events as the 95% confidence level upper limit for a γ -ray signal from ON+231 in the STACEE-32 data.

5.1.2 Calculating the Integral Flux Limit

In order to situate this upper limit with the other γ -ray results on ON+231 we must calculate the corresponding 95% confidence level upper limit on the flux. Because of the limited ADC resolution of STACEE-32, a spectral flux result is impossible; only the integrated flux can be calculated. In the simplest scenario the integral flux is simply the integration, with respect to energy, of the differential flux from the energy threshold, E_{th} to ∞ :

$$\Phi(E > E_{th}) = \int_{E_{th}}^{\infty} \frac{d\Phi}{dE} dE \quad (5.4)$$

We know that the differential flux has an energy dependence, we will assume that the energy flux is simply the extension of the mean EGRET flux times a constant:

$$\frac{d\Phi}{dE} = C \left(\frac{E}{1\text{GeV}} \right)^{-1.73} \text{cm}^{-2}\text{sec}^{-1}\text{GeV}^{-1} \quad (5.5)$$

The physical γ -ray trigger rate of our experiment is the integral of the product of the effective area, the efficiency of the χ^2 cut $\epsilon = 0.42$, (essentially our acceptance as a function of energy) with the differential energy spectrum:

$$R_{obs} = \epsilon \int_0^{\infty} \frac{d\Phi}{dE} A_{eff}(E) dE \quad (5.6)$$

where the integration is from zero to ∞ . Since the effective area, A_{eff} dies out at a finite energy larger than zero, we could also integrate from the turn on energy of the effective area function without changing the result of the integration.

If we substitute the assumed differential flux (equation 5.5) into equation 5.6 and use the effective area from figure 3.13, we can evaluate the integral numerically:

$$R_{obs} = C \times \epsilon \int_0^{\infty} E^{-1.73} A_{eff}(E) dE = C \times 3.2 \times 10^6 \text{sec}^{-1} \quad (5.7)$$

Taking R_{obs} to be the result of solving the upper limit calculation (equation 5.3) namely 376 events over the total fiducial time of the data set (18,750 seconds), we can solve for the constant C:

$$C = \frac{R_{obs}}{3.2 \times 10^6} = 6.3 \times 10^{-9} \text{cm}^{-2}\text{sec}^{-1}\text{GeV}^{-1} \quad (5.8)$$

When we integrate equation 5.5 with the value of C , from our threshold energy, 130 GeV, we obtain an upper limit on the integrated flux at a 95% confidence level :

$$\Phi(E > 130\text{GeV}) \leq 2.4 \times 10^{-10} \text{cm}^{-2}\text{sec}^{-1} \quad (5.9)$$

The uncertainty on the EGRET spectral index was ± 0.18 . Since this calculation is dependent on the spectral index, we have explored the integral flux limit variation as a function of the spectral index. We must take care to recalculate the threshold energy each time we vary the spectral index since this parameter is also dependent on the spectral index. For this reason the effective area and integral flux calculations were repeated for values of the spectral index ranging from $\Gamma=1.5$ to 2.0. The results are presented in figure 5.1.

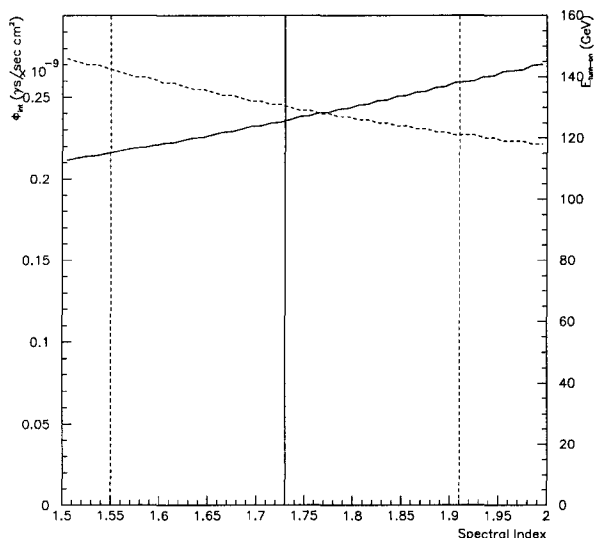


Figure 5.1: Integral flux upper limit and energy threshold variation as a function of spectral index. The solid line is the integrated flux upper limit (left scale) and the dashed line is the threshold energy (right scale). The vertical lines indicate the upper and lower limits on the uncertainty of the spectral index and the nominal value of the spectral index, $\Gamma=1.73$. When one lets the spectral index vary, in the energy threshold calculations and then in the integral flux calculation one notes only a small dependence on spectral index.

5.1.3 Systematic Uncertainty

Each part of the STACEE-32 instrument had to be characterised and quantified in order to understand the throughput. In chapters 2 and 3, several of these calibrations and characterisations are presented. However, these measurements, (reflectivity and transmission curves, phototube gains etc.), all carry varying degrees of uncertainty that affect the detector throughput. The uncertainty on the throughput results in a systematic error in the threshold energy of the flux measurement.

In chapter 3 we saw that γ -ray showers have general characteristics that differentiate them from proton-initiated showers. These characteristics don't fundamentally change with the energy of the initial γ -rays. The only element that changes with energy is the Čerenkov yield generated by the shower. That is, a 100 GeV shower, where half the Čerenkov photons are randomly and uniformly ignored, closely resembles a 50 GeV γ -initiated shower.

This calorimetric nature of the Čerenkov light yield greatly simplifies the systematic error analysis. Errors in the optical throughput of the telescope will change the effective energy scale of the experiment. If a factor of 2 error in the throughput estimation was made (specifically an error resulting in a 100% overestimation of the throughput), a 200 GeV shower would be accepted by the STACEE-32 telescope as a 100 GeV, since the main elements that affect the trigger of the instrument (the timing profile, the shower radius on the ground etc.) would remain the same. We can generalise this example by considering the nominal effective area curve, $A_{nom}(E)$, and the ratio of the true photon throughput of the detector to the estimated (nominal) throughput, β (in the previous example $\beta=0.5$). Thus because of the calorimetric nature of the photon yield, the actual

effective area $A_{true}(E)$ for a given energy would be

$$A_{true}(E) = A_{nom}(\beta E) \quad (5.10)$$

The underlying assumption of equation 5.10 is that γ -ray showers from different energies differ only in the number of Čerenkov photons produced on the ground. This assumption has been tested with simulations, and holds true with good accuracy for values of $\beta \sim 1$ [61]. Systematic uncertainties result in an error on β , in such a way that, if the various sources of error could be combined, they could be expressed as

$$\beta = 1 \pm \Delta\beta \quad (5.11)$$

where $\Delta\beta$ represents the uncertainty in the throughput (and since the shower photon yield scales linearly with energy, in the energy scale also).

To understand how $\Delta\beta$ would affect the experiment one must re-examine the spectral energy threshold, E_{thresh} . In section 3.3.3 we defined E_{thresh} as the maximum of the product of the differential flux for the observed source with the effective area. If we include the throughput uncertainty ($A(E) \rightarrow A(\beta E)$), for sources such as ON+231 with a power law spectrum, the product has the general form

$$A(E)E^{-\alpha} \rightarrow A(\beta E)E^{-\alpha} \quad (5.12)$$

If we define $E' = \beta E$, then to find the spectral energy threshold, E_{thresh} one must maximise:

$$A(E')E'^{-\alpha}\beta^\alpha \quad (5.13)$$

Since β^α is simply a constant, when we maximise equation 5.13, we are in reality maximising the functions on the left hand side of the transformation of equation 5.12. The maximum of this product occurs at the original threshold

energy $E' = E_{thresh-orig}$; thus using equation 5.11 the new threshold energy can be understood as:

$$E_{thresh-new} = \frac{E'}{\beta} = \frac{E_{thresh-orig}}{\beta} \approx E_{thresh-orig}(1 \pm \Delta\beta) \quad (5.14)$$

Hence the fractional uncertainty of the spectral threshold energy is equal to $\Delta\beta$.

By replacing $A(E)$ with $A(\beta E)$ and E_{thresh} with E_{thresh}/β in the calculations for the integrated flux described in section 5.1.2, we see that β cancels out of the integrated flux calculation and that

$$\Phi_{int}(E > E_{thresh-orig}) = \Phi_{int}(E > E_{thresh-new} = \frac{E_{thresh-orig}}{\beta}) \quad (5.15)$$

Thus changing the throughput parameter β does not change the integrated flux but does change the value at which that flux is quoted.

Given the previous arguments, the determination of systematic error on the threshold energy reduces to estimating the fractional uncertainty $\Delta\beta$. The estimation of $\Delta\beta$ is achieved by estimating the various uncertainties that could lead to a loss of throughput and then adding these uncertainties in quadrature. There are 10 primary sources of uncertainty; what follows are brief descriptions of these sources of systematic throughput loss and estimates of the uncertainty associated with each.

Čerenkov photon production The uncertainty in the Čerenkov light yield we think we should see according to our simulations has a direct effect on the nominal effective area curve. We estimate this uncertainty by comparing the Čerenkov yield of two different shower simulation programs. At energies relevant to our analysis, comparisons between MOCCA and CORSIKA result in yields that differ by about 5% [81]. Thus we estimate the uncertainty of the simulated Čerenkov yield at 5%.

Atmospheric attenuation Losses of Čerenkov photons due to atmospheric attenuation will also have a direct effect on the effective area curve. The atmospheric attenuation model used by STACEE-32 has been compared to other atmospheric models [82]. A 10% difference in photon production was observed between different models, thus an uncertainty of 10% is associated with atmospheric attenuation.

Heliostat reflectivity The heliostat mirror reflectivity was measured (see figure 2.11); the systematic uncertainty on the overall reflectivity is estimated to be 10% [83].

Secondary mirror reflectivity The reflectivity of the secondary mirrors were measured by the manufacturer. Although specific data could not be obtained, a conservative estimate of the uncertainty on the secondary reflectivity measurement would be to assume that it was on par with the reflectivity measurements of the heliostats. Thus an uncertainty of 10% is attributed to the secondary mirrors.

Can misalignment The PMT canisters were positioned on the camera to collect the maximum amount of light. CCD images of the Moon were taken for each can. The can positions were then adjusted so that the light collected by the DTIRCs was within a few percent of its optimum value. Because of the uncertainties in the CCD analysis and because of the difficulty in repositioning the cans accurately when the camera is not disassembled, an uncertainty of 5% is attributed to the throughput due to can positioning.

Photocathode efficiency The PMT quantum efficiency curve was taken from the manufacturer's catalog. The cathode sensitivity to blue light is given as $11.0 \mu A/lmF$ with a minimum value of $9.0 \mu A/lmF$ [59]. Thus, we assume a possible difference of $\pm 2.0 \mu A/lmF$, and take the RMS error on the quantum efficiency to be 13%.

PMT to DTIRC optical coupling As shown in figure 2.9, the coupling between the PMT and the DTIRC is achieved by using a thin silicone disk, called a cookie. After assembly of the cameras for STACEE-32 it was determined that these cookies had a non-negligible expansion coefficient. At low temperatures they contract and shrink in thickness, often causing a loss of the coupling between the DTIRC and PMT. The cans were checked on a nightly basis and were re-coupled if signs of decoupling were noticed. At the end of observing nights most tubes had conserved their optical coupling while some tubes would have roughly $\sim 10\%$ of their photocathode surface area decoupled from the DTIRCs. We simply assign an optical coupling uncertainty of 5%.

Phototube gains and trigger model The average discriminator threshold setting for the ON+231 data set was 128 mV. Based on measurements of the average single photoelectron pulse, measured at 25 mV (after amplification in the front end electronics) we set the tube trigger level in the trigger model to > 5 photoelectrons. If the gain of a tube is overestimated then more photoelectrons will be needed to make that tube trigger. When one considers the gain measurements discussed in section 2.2.4.2 it is clear that an error in the gain measurement will result in a loss of signal. Therefore, the uncertainty associated with the gain measurement, 10%, must also be included in our throughput uncertainty.

Heliostat optics In section 3.2.1 we described how heliostat simulations were tuned to reproduce sunspot curves. The uncertainty associated with the light flux hitting the secondary in the sunspot measurements was 10%. The heliostat simulation code within sandfield, reproduced the measured relative flux to within 6%. Sunspot shapes were also seen to have a strong dependence on the Sun's elevation. Uncertainty of the sunspots sizes and shapes

based on the Sun's elevation were estimated to be 15%. Thus when we add these three uncertainties in quadrature we obtain a total uncertainty of 19% for the heliostat optics throughput.

Heliostat bias drift In November of 1998 the STACEE-32 heliostat biases were optimised by taking moon images. It was thought that these biases would remain constant, with the obvious exception of the biases of heliostats that had any of their drive motors replaced or adjusted. This was not the case. In the late spring of 1999 the biases were rechecked and some of the biases had drifted by as much as 4 bits. The amount of throughput loss over time was almost impossible to determine, since the details of the bias drift are unknown. Later studies determined that a bias error of one bit was accompanied by a 5% error in throughput [57]. Since our entire data set was taken in the early spring of 1999, we conservatively associate a 20% uncertainty to heliostat bias drift.

Using equation 5.14 and the final $\Delta\beta$ from table 5.3. The STACEE-32 ON+231 spectral threshold energy with errors can be stated as:

$$E_{th} = 130(1 \pm \Delta\beta) \approx 130 \pm 50 \text{ GeV} \quad (5.16)$$

5.2 Discussion and Conclusion

The purpose of the STACEE-32 prototype was to demonstrate that one could use a thermal solar power generating station as an astronomical instrument. This was achieved in 1999 when the STACEE collaboration reported a 7σ detection of the Crab [84]. During the STACEE collaboration's first Crab observation season, a small data set was also collected for AGN ON+231. While, we can not report a detection of this AGN, we have set a 95% confidence level upper limit on its

Čerenkov photon production	6%
Atmospheric attenuation	10%
Heliostat reflectivity	10%
Secondary mirror reflectivity	10%
Can misalignment	5%
Photocathode efficiency	13%
PMT to cookie optical decoupling	5%
Phototube gains and trigger model	10%
Heliostat optics	19%
Heliostat bias drift	20%
Total uncertainty $\Delta\beta$	37%

Table 5.3: The 10 major sources of systematic uncertainty summarised and added in quadrature.

integral flux at the spectral energy threshold determined for this source:

$$\Phi_{int}(E > 130 \pm 50\text{GeV}) \leq 2.4 \times 10^{-10} \text{cm}^{-2} \text{sec}^{-1} \quad (5.17)$$

When these calculations are repeated for a 99% confidence level we obtain an upper limit on the integrated flux of:

$$\Phi_{int}(E > 130 \pm 50\text{GeV}) \leq 3.1 \times 10^{-10} \text{cm}^{-2} \text{sec}^{-1} \quad (5.18)$$

Since ON+231 has not been detected above EGRET energies this upper limit constitutes a further constraint on the γ -ray emission spectrum of this AGN. When the STACEE-32 result is plotted with the extrapolated EGRET ON+231 integrated flux and the latest (1999) Whipple upper limit of this AGN [47], we note that the STACEE-32 upper limit is roughly an order of magnitude lower than the projected EGRET flux at that energy (see figure 5.2).

To fully comprehend this plot some explanation is necessary. In figure 5.2 the

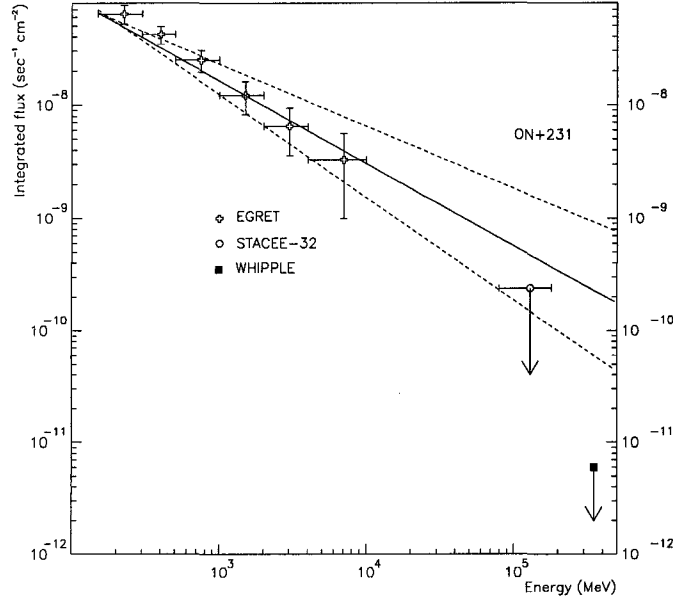


Figure 5.2: The STACEE-32 ON+231 integral flux upper limit is plotted with the Whipple 1999 UL at 350 GeV and the extrapolated EGRET integrated flux spectrum. STACEE-32 95% CL upper limit further constrains the γ -ray flux from this AGN. The solid line is the integrated EGRET flux using the nominal value for the spectral index. The dashed lines are the integrated fluxes with the upper and lower bounds (1σ) of the EGRET spectral index, ($\Gamma = -1.73 \pm .18$).

central solid line is the result of integrating the nominal differential EGRET flux for this source from a minimum, E_i , energy to ∞ :

$$\int_{E_i}^{\infty} 2.1 \times 10^{-11} (E/721 \text{ MeV})^{-1.73} dE \text{ sec}^{-1} \text{ cm}^{-2} \text{ MeV}^{-1} \quad (5.19)$$

The two dotted lines represent the integrated fluxes of the upper and lower bounds of the EGRET spectral index ($\Gamma = -1.51$ and $\Gamma = -1.91$ respectively), calculated in the same manner.

The integrated EGRET flux points were calculated from raw data from the 3rd EGRET catalog [85, 5]. The differential flux for each energy bin i was multiplied by the width of the bin to obtain the integrated flux for that bin, ϕ_i . To calculate an integrated flux for any bin i , Φ_i , the sum of all the fluxes from each bin with a higher energy was added to the flux of the bin.

$$\Phi_i = \sum_i^{i_{max}} \phi_i \quad (5.20)$$

The highest energy bin in the EGRET data is from 4 to 10 GeV; this essentially imposes an upper limit on the EGRET energy range that is less than ∞ and thus results in a lower last bin and an error in the normalisation of the overall integrated flux as calculated from the EGRET data points. This lack of the “tail” of the integral flux to infinity that is needed to calculate an integrated flux, is the reason the EGRET points lie below the nominal integrated flux line. One should note that the slope of these points is parallel to that of the integrated nominal flux line.

When the lower and upper bounds of the differential EGRET fluxes are plotted they intersect at the 721 MeV pivot value quoted in the EGRET flux, (see figure 5.3 and equation 1.23). The point at which integrated fluxes cross bears no special significance.

Since several studies ([45, 43] for example) have already concluded that ON+231’s spectral cut-off could not be due to intergalactic IR field absorption, the implications of this constraint on the ON+231 flux limit the γ -ray emission production mechanism of the AGN itself.

This non-detection should be taken as a reason this AGN should remain a strong candidate for observing time with the future manifestations of the STACEE telescope. Other reasons are:

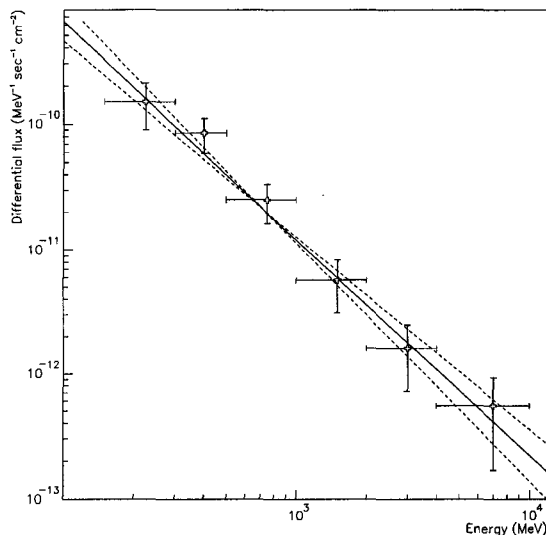


Figure 5.3: The EGRET differential spectrum presented in figure 1.23 is reproduced with the raw EGRET data points. For comparison the upper and lower bounds of the spectral index are also plotted in dashed lines.

Improved sensitivity in STACEE-48 Many of the shortcomings of the STACEE-32 prototype mentioned in this thesis such as the lack of ADCs for every channel, biasing errors and poor heliostat focusing have been corrected in the 48 channel version of STACEE. In addition to these improvements which should affect our energy threshold and our flux sensitivity, STACEE-48 will have a 50% increase in collection area over STACEE-32. These improvements have already borne fruit in the STACEE-48 detection of Mrk 421 in 2001 [86]. With a more sensitive instrument operating at a lower threshold another observation campaign on ON+231 could result in a first detection above EGRET energies from this AGN or could further constrain its emission spectrum.

Flaring activity ON+231, much like Mrk 421 [17], has been observed in a

flaring state by EGRET [5]. When an AGN is in a flaring state its flux increases dramatically, and its emission spectrum may also undergo spectral hardening. Thus, there are two mechanisms where one could possibly obtain a large enough flux to be detected at STACEE energies.

ON+231: an interesting source Section 1.4 was entirely dedicated to the history and scientifically interesting aspects of this source. ON+231 has been the object of recent multiwavelength studies and will continue to be an intensely studied AGN by members of every branch of the extragalactic astrophysical community. The biggest source dependent reason to further study this AGN with future manifestations of STACEE is that it would be one of the first detection of an AGN above EGRET energies that was not detected by the imaging detectors. Because it has the hardest spectral index of all EGRET detected AGN and because of its relative proximity ($z=0.102$), ON+231 is a good candidate for detection at lower energies.

A convenient source for STACEE-48 The current ON+231 data set was collected with STACEE-32 because ON+231 would rise as the Crab was setting. This situation will not change with STACEE-48. If the collaboration decides to undertake an improved Crab observation campaign with the 48 channel version of the telescope, ON+231 will be an ideal source to finish evenings where there is still dark time after the Crab has set. This observation strategy would not interfere with another Crab observation and would increase the duty cycle of the instrument.

We thus strongly suggest that more data on ON+231 be taken with the STACEE-48 experiment. A detection of ON+231 above EGRET energies, or further constraints on its emission spectrum, would prove a significant benefit to AGN research.

Bibliography

- [1] S.M. Derdeyn et al. SAS-B Digitized Spark Chamber Gamma Ray Telescope. *Nuclear Methods and Instruments*, 98:557, 1972.
- [2] D.J. Thompson et al. SAS-2 high-energy gamma-ray observations of the VELA pulsar. *Astrophysical Journal Letters*, 200:79, 1975.
- [3] P.V. Ramana Murthy and A.W. Wolfendale. *Gamma-Ray Astronomy*. Cambridge University Press, 1993.
- [4] Kanbach et al. EGRET (Energetic Gamma-Ray Experiment Telescope) on NASA's Gamma-Ray Observatory (GRO). *Space Science Reviews*, 49:69, 1988.
- [5] R.C. Hartman et al. The Third EGRET Catalog of High-Energy Gamma-Ray Sources. *Astrophysical Journal Supplement Series*, 123:79, 1999.
- [6] see GLAST web page at <http://www-glast.stanford.edu/>.
- [7] M. Samorski and W. Stamm. Detection of 2×10^{15} to 2×10^{16} eV gamma-rays from Cygnus X-3. *Astrophysical Journal Letters*, 268:17, 1983.
- [8] B. Dingus et al. Ultrahigh-energy pulsed emission from Hercules X-1 with anomalous air-shower muon production. *Physics Review Letters*, 61:1906, 1988.

- [9] A. Borione et al. *Nuclear Instruments and Methods A*, 346:329, 1994.
- [10] J. Fowler. *Composition and Spectrum of Cosmic Rays at the Knee Measured by the CASA-BLANCA Experiment*. PhD thesis, University of Chicago, 1999.
- [11] C.W. Allen. *Astrophysical Quantities*. The Athlone Press, London, 3rd edition edition, 1976. p.124.
- [12] C.M. Hoffman et al. Gamma-ray Astronomy at High Energies. *Review of Modern Physics*, 71, 1999.
- [13] M.F. Cawley et al. Search for gamma-rays above 400 GeV from Geminga. volume 1, page 173, La Jolla, Springfield Virginia, 1985. in 19th International Cosmic Ray Conference proceedings.
- [14] R.A. Ong. Very High-Energy Gamma-Ray Astronomy. *Physics Reports*, 305(93), 1998.
- [15] T. Weekes. VHE Astronomy before the New Milleneum. In *GeV-TeV Astrophysics: Towards a Major Atmospheric Cherenkov Telescope VI*, Snowbird, Utah, 1999.
- [16] A. D. Kerrick et al. Upper Limits on TeV Gamma-ray Emission from Active Galactic Nuclei. *Astrophysical Journal*, 452:588, 1995.
- [17] J. E. McEnergy et al. TeV Observations of the Variability and Spectrum of Markarian 421. In *Proceedings of the 25th International Cosmic Ray Conference*, Durban, 1997.
- [18] E. Fermi. *Physical Review*, 75:1169, 1949.
- [19] M.S. Longair. *High Energy Astrophysics: Stars, the Galaxy and the interstellar medium*. Cambridge University Press, 2nd edition edition, 1994.

- [20] M. G. Baring. Diffusive Shock Acceleration: The Fermi Mechanism. In Y. Giraud-Heraud and J. Tran Thanh Van, editors, *Very High Energy Phenomena in the Universe*, page 97. XXXII Morion Workshop, Editions Frontieres, 1997.
- [21] G. Chanmugan and K. Brecher. Ultra-high energy gamma rays and cosmic rays from accreting degenerate stars. *Nature*, 313:767, 1985.
- [22] L. G. Maraschi et al. A jet model for the gamma-ray emitting blazar 3C 279. *Astrophysical Journal*, 397:L5, 1992.
- [23] de Jager et al. Gamma-Ray Observations of the Crab Nebula: A Study of the Synchro-Compton Spectrum. *Astrophysical Journal*, 457:253, 1996.
- [24] F.W. Stecker and M. H. Salamon. Absorption of high-energy gamma rays by interactions with extragalactic starlight photons at high redshifts and the high-energy gamma-ray background. *Astrophysical Journal*, 493:547, 1998.
- [25] Ford et al. HST FOS spectroscopy of M87: Evidence for a disk of ionized gas around a massive black hole. *Astrophysical Journal, Letters*, 435:L27, 1994.
- [26] J. Frank et al. *Accretion Power in Astrophysics*. Cambridge University Press, 1992.
- [27] A. J. Kembhavi and J. V. Narlikar. *Quasars and Active Galactic Nuclei an Introduction*. Cambridge University Press, 1999.
- [28] Sikora et al. Comptonization of diffuse ambient radiation by a relativistic jet: The source of gamma rays from blazars? *Astrophysical Journal*, 421:153, 1994.
- [29] G. Henri et al. Active galactic nuclei as high energy engines. *Astroparticle Physics*, 11:347, 1999.

- [30] M. Wolf. *Astron. Nach2.*, (202):415, 1916.
- [31] Tosti et al. BVR monitoring of ON 231 during the great outburst in 1994-1997. *Astronomy and Astrophysics*, 130:109, 1998.
- [32] F. Biraud. Rapid Optical Variability of the Source PKS 1514-24. *Nature*, 232:178, 1971.
- [33] I.W.A. Browne. Two Bright Quasi Stellar Radio Sources. *Nature*, 231:515, 1971.
- [34] E. Massaro et al. The extraordinary optical outburst of ON 231 (W Com) in spring 1998. *Astronomy and Astrophysics*, 342:L49, 1999.
- [35] E. Massaro et al. Two-sided radio emission in ON 231 (W Comae). *submitted to Astronomy and Astrophysics*, 1999. accepted 17 May 2001.
- [36] M.K. Babadzhanyants et al. ON 231: the testing of 3.8-year period for optical outbursts with multi-peak structure. *Astronomy Astrophysics*, 356:L21, 2000.
- [37] A. Sillanpaa et al. *Astrophysical Journal*, 325:628, 1988.
- [38] F. Homma et al. *PASJ*, 1992.
- [39] F.K. Liu G.Z. Xie J.M. Bai. An historical light curve of ON 231 and its periodic analysis. *Astronomy and Astrophysics*, 295:1, 1995.
- [40] D. Stannard and B.K. McIllwrath. Extended radio structure of BL Lac type objects. *Nature*, 298:140, 1982.
- [41] D. Weistrop et al. Optical and Radio Observations for the BL Lacertae objects 1219+28, 0851+202 and 1400+162. *Astrophysical Journal*, 292:614, 1985.
- [42] J. H. Krolic. *Active Galactic Nuclei*. Princeton University Press, 1999.

- [43] G. Tagliaferri et al. The concave X-ray spectrum of the blazar ON 231: The signature of intermediate BL Lacs objects. *Astronomy Astrophysics*, 354:431, 2000.
- [44] C. vonMontigny et al. High-Energy Gamma-ray Emission from Active Galaxies: EGRET Observations and their Implications. *Astrophysical Journal*, 440:525, 1995.
- [45] M. Maisack et al. A Multi-Frequency Campaign on the γ -ray loud blazar W Comae. In *Conference on Blazars, Black Holes, and Jets*, Girona, Spain, 1996.
- [46] R. Mirzoyan et al. (The HEGRA Collaboration). The first telescope of the HEGRA air Cherenkov imaging telescope array. *Nuclear Instruments and Methods A*, 351:513, 1994.
- [47] J.H. Buckley. Observations of blazars with the Whipple Observatory gamma-ray telescope. *Astroparticle Physics*, 11:119, 1999.
- [48] B. Geibels et al. Prototype tests for the CELESTE solar array gamma-ray telescope. *Nuclear Instruments in Physics Research A*, 412:329, 1998.
- [49] T.C. Weekes et al. Very Energetic Radiation Imaging Telescope Array System (VERITAS) proposal. *Smithsonian Astrophysical Observatory*, Nov. 1996.
- [50] F.A. Aharonian et al. The potential of ground based arrays of imaging atmospheric Cherenkov telescopes: I. Determination of shower parameters. *Astroparticle Physics*, 6:343, 1997.
- [51] E. Lorenz. In *Proc. of the 25th International Cosmic Ray Conference*, page 177, Durban, 1997.
- [52] P. Baillon et al. Gamma ray spectrum of the Crab nebula in the multi TeV region. *Astroparticle Physics*, 341:79, 1993.

- [53] P. Goret et al. Observations of TeV gamma rays from the Crab nebula. *Astronomy and Astrophysics*, 270:401, 1993.
- [54] J.A. Zweerink et al. In *Proceedings of the GeV-TeV Gamma Ray Astronomy Workshop*, Snowbird, 1999. AIP. AIP Conference Proceedings.
- [55] F. Aqueros et al. The GRAAL project. In *Proceedings of the 26th International Cosmic Ray Conference*, volume 5, page 215, 1999.
- [56] M. Chantell et al. Prototype Test Results of the Solar Tower Atmospheric Cherenkov Effect Experiment (STACEE). *Nuclear Instruments and Methods A*, 408:468, 1998.
- [57] R. Scalzo and J. Hinton. Measurement of Heliostat Bias Drift and Light Collection. Internal STACEE Collaboration note 00-14, 2000.
- [58] R. Winston et al. Dielectric Totally Internally Reflecting Concentrators. *Applied Optics*, 26(2), 1987.
- [59] Philips Corporation. Photomultiplier Tubes. Technical report, 1997. Page 24.
- [60] Francois Vincent. Photomultiplier tube gain measurement using an uncalibrated light source. Master's thesis, McGill University, 2000.
- [61] S.M. Oser. *High Energy Gamma-ray Observations of the Crab Nebula and Pulsar with the Solar Tower Atmospheric Cherenkov Effect Experiment*. PhD thesis, University of Chicago, 2000.
- [62] D. Hanna and R. Mukherjee. STACEE Note 99-03: First Results from the STACEE Laser System. Internal STACEE Collaboration note, 1999.
- [63] A.M. Hillas. In *Proc. 19th Int. Cosmic Ray Conf.*, volume 1, page 155, La Jolla, 1985.

- [64] D. Heck et al. CORSIKA: A Monte Carlo Code to Simulate Extensive Air Showers. technical report FZKA 6019, Institute Fur Kernphysik, Forschungszentrum Karlsruhe, 1998.
- [65] K. Binder, editor. *Topics in Current Physics: Monte Carlo Methods in Statistical Physics*. Springer-Verlag, 2nd edition, 1986.
- [66] Adolph S. Jura, editor. *Handbook of Geophysics and the Space Environment*. USAF Geophysics Laboratory, 1985.
- [67] R. Santer. ATERMIS Collaboration internal note, 1990. Private communications as cited by P. Fleury et al. *UV Light in the Atmosphere*.
- [68] J. Linsey and A.M. Hillas. In *Proc. of the Paris Workshop on Cascade Simulations*, page 39, 1981.
- [69] A.M. Hillas. Shower Simulation: Lessons from MOCCA. *Nuclear Physics B (Proc. Supp.)*, 52B:29, 1997.
- [70] S. Oser. Analysis of Heliostat Sunspot Images and Comparison to Simulations. Internal STACEE Collaboration note 99-08, 1999.
- [71] R. Scalzo. Camera Box Occultation 101: What Happens When You Take The Sides Off? Internal STACEE Collaboration note 01-01, 2001.
- [72] M. de Naurois. Étude de la photocathode CELESTE. Internal CELESTE collaboration note, 1998.
- [73] Burnett et al. Energy Spectra of Cosmic Rays Above 1 TeV per Nucleon. *Astrophysical Journal Letters*, 349:25, 1990.
- [74] D. Dumora et al. CELESTE experimental proposal. Technical report, CELESTE collaboration, 1996.

- [75] A.M. Hillas et al. The Spectrum of TeV Gamma Rays from the Crab Nebula. *Astrophysical Journal*, 503:744, 1998.
- [76] C.H. Vincent. Estimation of Multiple Coincidences. *Nuclear Instruments in Physics Research A*, 127:421, 1975.
- [77] K.J. Ragan. Level 1 trigger rate variations. Internal STACEE Collaboration note, 1999.
- [78] W.H. Press S.A. Teukolsky W.T. Vetterling B.P. Flannery. *Numerical Recipes in C, The Art of Scientific Computing*. Cambridge University Press, 1996.
- [79] R.M. Barnett et al. Review of Particle Physics. *Physical Review D*, 54, 1996.
- [80] R.D. Cousins. *AM.J.Phys*, 63:398, 1995.
- [81] J. Hinton. A comparison of the MOCCA and CORSIKA air-shower simulation codes. Internal STACEE Collaboration note 00-10, 2000.
- [82] C. Tyler. Notes on Sources at Low Elevation Angles. Internal STACEE Collaboration note, 1999.
- [83] Mark Chantell, 1999. Private communications as cited by S. Oser in Ph.D. thesis.
- [84] S. Oser et al. High Energy Gamma-ray Observations of the Crab Nebula and Pulsar with the Solar Tower Atmospheric Cerenkov Effect Experiment. *Astrophysical Journal*, 547:949, 2001.
- [85] R. Mukherjee, 2001. Private communications.
- [86] Ong et al. STACEE Observations of Active Galactic Nuclei and Other Sources. In *27th International Cosmic Ray Conference proceedings*, Hamburg, Germany, 2001. OG 2.2.3.